Operation of Microgrids with Conventional and Virtual Energy Storage Systems

by

Samuel Córdova

A thesis
presented to the University of Waterloo
in fulfillment of the
thesis requirement for the degree of
Doctor of Philosophy
in
Electrical and Computing Engineering

Waterloo, Ontario, Canada, 2022

Examining Committee Membership

The following served on the Examining Committee for this thesis. The decision of the Examining Committee is by majority vote.

Supervisor:	Claudio Cañizares University Professor, Dept. of Electrical and Computing Engineering, University of Waterloo
Supervisor:	Álvaro Lorca Associate Professor, Dept. of Electrical Engineering, Dept. of Industrial and Systems Engineering, Pontifical Catholic University of Chile
Internal Member:	Matias Negrete Associate Professor, Dept. of Electrical Engineering, Pontifical Catholic University of Chile
Internal Member:	Juan de Dios Ortúzar Emeritus Professor, Dept. of Transport Engineering and Logistics, Pontifical Catholic University of Chile
Internal Member:	Kankar Bhattacharya Professor, Dept. of Electrical and Computing Engineering, University of Waterloo

Internal Member:	Mehrdad Kazerani Professor, Dept. of Electrical and Computing Engineering, University of Waterloo
Internal-External Member:	Mehrdad Pirnia Lecturer, Dept. of Management Sciences, University of Waterloo
External Examiner:	Gabriela Hug Full Professor, Dept. of Information Technology and Electrical Engineering, Swiss Federal Institute of Technology (ETH) Zurich

Author's Declaration

I hereby declare that I am the sole author of this thesis. This is a true copy of the thesis, including any required final revisions, as accepted by my examiners.

I understand that my thesis may be made electronically available to the public.

Abstract

Distribution systems are now increasingly becoming more active due to the sustainable integration of Distributed Energy Resources (DER). While this has enabled a cleaner and more efficient generation, it has also resulted in new challenges for the operation of modern power systems. In this context, the operation of isolated microgrids is particularly challenging, as these systems are characterized by a low inertia and significant renewable integration, and must be capable of an autonomous operation without the support of other electrical grids. Thus, the present thesis focuses on the design of an Energy Management System (EMS) for the reliable and economic operation of modern isolated microgrids.

Isolated microgrid operation requires considering additional aspects typically omitted in the operation of robust bulk power systems. In particular, as demonstrated in this thesis, second-to-second renewable power fluctuations need to be considered in the microgrid EMS, since these fluctuations can have a large impact on the system's frequency regulation due to its low inertia. Furthermore, to ensure an economic yet reliable operation, modern flexible technologies capable of counterbalancing these short-term fluctuations, such as Battery Energy Storage Systems (BESS) and Demand Response (DR), need to be integrated in the microgrid EMS. Hence, the present thesis focuses on designing a microgrid EMS model that integrates short-term renewable power fluctuations, their impact on frequency regulation, and the role that BESS and DR can play for their management.

In the first part of the thesis, models are presented to characterize short-term renewable power fluctuations and their impact on microgrid operations, including the role that BESS can play to manage power fluctuations and the battery degradation resulting from providing this service. These models are then used to develop a practical EMS considering short-term renewable fluctuations and BESS flexibility, which is validated through exhaustive simulations on two realistic test microgrids, showing the operational benefits of the proposed EMS and highlighting the need to properly model short-term fluctuations and battery degradation in EMS for isolated microgrids.

In the second part of the thesis, the above EMS model is extended to also incorporate the impact of short-term power fluctuations on the microgrid's frequency regulation performance. For this purpose, accurate linear equations describing the frequency deviation and Rate-of-Change-of-Frequency (RoCoF) resulting from these fluctuations are developed, which are then used to build a frequency-constrained EMS model capable of guaranteeing an adequate frequency regulation performance in line with current DER operating standards. Exhaustive transient simulations on a realistic test microgrid considering detailed frequency dynamic and control models are presented, demonstrating the accuracy

of the proposed frequency-constrained EMS and the operational benefits resulting from its implementation.

Finally, the integration of DR techniques for an enhanced microgrid operation is discussed. In particular, the smart control of Thermostatically Controlled Loads (TCL) is studied, as these type of loads comprise a significant share of the total residential demand, and have the capability of managing second-to-second power imbalances without significantly affecting customer comfort. Since computational limitations prevent the direct integration of TCLs within operational models, alternative computationally efficient aggregate models representing TCL flexibility and frequency dynamics are proposed, which are referred to as Virtual Energy Storage Systems (VESS) due to their close resemblance to Conventional Energy Storage Systems (CESS) such as batteries. The proposed aggregate VESS models are then used to design a practical EMS integrating TCL flexibility, and study the impact of TCL integration on microgrid operation and frequency control. Computational experiments using detailed frequency transient and thermal dynamic models are presented, demonstrating the accuracy of the proposed aggregate VESS models, as well as the economic and reliability benefits resulting from using these aggregate models to integrate TCLs in microgrid operation.

Acknowledgements

I would like to express my profound gratitude to my supervisors, Professor Álvaro Lorca and Professor Claudio Cañizares, for their guidance and support during my studies at the Pontifical Catholic University of Chile and the University of Waterloo. It has been a privilege to learn from such extraordinary people, which are not only true experts in their areas, but also have a deep passion for their research. It was thanks to their continuous encouragement, feedback, and support that I was able to complete this thesis.

My sincere thanks to Professor Daniel Olivares, who actively participated during the development of my research. Without any doubts, his observations and feedback played a key role in the completion of this thesis.

I want to thank my Ph.D. Committee for their valuable comments and observations: Professors Kankar Bhattacharya, Mehrdad Kazerani, and Mehrdad Pirnia from the University of Waterloo; Professors Matías Negrete and Juan de Dios de Ortúzar from the Pontifical Catholic University of Chile; and Professor Gabriela Hugh from ETH Zurich.

Thanks to my friends and colleagues at ECS-lab and EMSOL-lab: Nicolás, Cristían, Tomás, Iván, Fabián, William, Mauricio, Dario, Carlos, Matheus, Sofia, and Pablo. Thank you all for creating a friendly working environment in the lab.

I would also like to thank ANID, the Pontifical Catholic University of Chile and the University of Waterloo for awarding the scholarships and providing the financial support for this thesis.

Finally, my deepest gratitude to my parents Miluska and Samuel. All my achievements have been the result of your unconditional love and support during my whole life.

Dedication

To my parents, Miluska and Samuel

Table of Contents

List of Figures

List of Tables

List of Abbreviations

AGC Automatic Generation Control

BESS Battery Energy Storage Systems

CESS Conventional Energy Storage Systems

DER Distributed Energy Resources
DoD Depth-of-Discharge
DR Demand Response

EMS Energy Management System
ERU Expected Reserve Utilization
ESS Energy Storage Systems

FOH First-Order Hold
FoR Frequency-or-RoCoF

KLFN Kasabonika Lake First Nation

LHP Limit-Hit Probability
Li-Ion Lithium-Ion
LS Load Shedding

MAE Mean Absolute Error

MC Monte Carlo

MILP Mixed Integer Linear Programming

MPC Model Predictive Control

NaS Sodium-Sulphur

NiMH Nickel-Metal-Hydride

QSS Quasi-Steady-State

RC Renewable Curtailment

RoCoF Rate-of-Change-of-Frequency

SM Synchronous Machine

SoC State-of-Charge

TCL Thermostatically Controlled Loads

UC Unit Commitment

UFLS Under-Frequency Load Shedding

VBC Virtual Battery Controller

VESS Virtual Energy Storage Systems

VFC Voltage Frequency Control

VRB Vanadium Redox Flow Battery

ZOH Zero-Order Hold

Nomenclature

Functions

$(\cdot) \setminus (\cdot)$	Set difference
$(\cdot)^{+}$	Positive part
$(\cdot)^{-}$	Negative part
$\boldsymbol{\mathcal{F}}^{ID}(\cdot)$	Cycle identification algorithm
$\Gamma^{\lambda}(\cdot)$	Cycle depth stress factor
$\|\cdot\|$	Infinity norm
$\lvert\cdot\rvert$	Absolute value
$\mathbb{E}(\cdot)$	Expected value of a random variable
$\mathcal{F}^{CYC}(\cdot)$	Battery cycle aging
$\mathcal{F}^{OBJ}(\cdot)$	Objective function
$\mathcal{G}^{\mathcal{K}}(\cdot)$	Geary's kurtosis
dim $(\cdot)$	Dimension of a variable
exp $(\cdot)$	Exponential function
mad $(\cdot)$	Mean absolute deviation of a random variable
Prob $(\cdot)$	Probability of an event
std $(\cdot)$	Standard deviation of a random variable

tae $(\cdot)$	Truncated absolute expectation of a random variable

Indices and Sets

$\mathcal{H}^r \subset \mathcal{H}$	Subset of first dispatch time intervals with a finer time resolution
$b \in \mathcal{B}$	Index and set of batteries
$g \in \mathcal{G}$	Index and set of thermal generators
$h \in \mathcal{H}$	Index and set of dispatch (or long) time intervals, $\mathcal{H} = \{1, \ldots, H\}$
$i \in \mathcal{I}$	Index and set of Monte Carlo scenarios
$j \in \mathcal{J}$	Index and set of intra-dispatch (or short) time intervals, $\mathcal{J} = \{1, \ldots, J\}$
$l \in \mathcal{L}$	Index and set of partitions for piecewise battery degradation model
$m \in \mathcal{M}$	Index and set of charging-discharging cycles resulting from a cycle identification algorithm, $\mathcal{M} = \{1, \ldots, M\}$
$n \in \mathcal{N}$	Index and set of TCLs, $\mathcal{N} = \{1, \ldots, N\}$
$t \in \mathcal{T}$	Index and set of generic time intervals

Parameters

α^B	AGC participation factor for batteries
α^G	AGC participation factor for thermal generators
α^W	Time constant for wall thermal dynamics [1/s]
$\mathbf{1}$	Vector of ones with the appropriate dimension
$\Delta\tau$	Time-step size for intra-dispatch (or short) time interval [s]
$\Delta\theta^{TCL}$	Temperature deadband width of TCLs [°C]
ΔT	Time-step size for dispatch (or long) time interval [s]
Δt	Time-step size for generic time interval [s]
ϵ^{χ}	Parameter for adjusting the confidence level of forecast error reserves

$\epsilon^{\partial r}$	Parameter for adjusting the confidence level of regulation-ramp reserves
ϵ^{r}	Parameter for adjusting the confidence level of regulation reserves
$\eta^{B,C}, \eta^{B,D}$	Charging and discharging efficiency for battery
η^{TCL}	Coefficient of performance of TCLs
γ^{V}	Self-discharging rate for virtual battery [1/h]
γ^{TCL}	Self-discharging rate of the virtual stored energy in a TCL [1/s]
$\hat{\phi}$	Piecewise linear battery degradation coefficient
$\hat{P}^{L}$	Forecast average load for a given dispatch time interval [kW]
κ^{B}	Droop gain for batteries
κ^{G}	Droop gain for thermal generators
κ^{V}	Droop gain for virtual battery
μ	Safety derating factor applied to virtual battery's capacity limits in EMS model
$\overline{\Delta f}$	Frequency deviation limit imposed by DER operating standards [Hz]
$\overline{E}^{V}, \underline{E}^{V}$	Upper and lower bounds for virtual battery's energy capacity limit [kWh]
$\overline{P}^{W}, \overline{P}^{S}$	Maximum available wind and solar average powers for a given dispatch time interval [kW]
$\overline{P}^{B}$	Maximum rated charging/discharging power for battery [kW]
$\overline{P}^{TCL}$	Rated electric power of TCLs [kW]
$\overline{P}^{V,C}, \underline{P}^{V,C}$	Upper and lower bounds for virtual battery's charging power limit [kW]
$\overline{P}^{V,D}, \underline{P}^{V,D}$	Upper and lower bounds for virtual battery's discharging power limit [kW]
$\overline{RoCoF}$	RoCoF value limit imposed by DER operating standards [Hz/s]
$\overline{S}$	SoC depth range of battery partition

θ^{A}	Ambient temperature [°C]
θ^{G}	Ground temperature [°C]
$\theta^{F,SS}$	Steady-state floor temperature [°C]
$\theta^{I,SP}$	Temperature set-point of TCLs [°C]
$\theta^{W,0}, \theta^{W,SS}$	Initial and steady-state wall temperature [°C]
$\tilde{\sigma}^{\chi,L}$	Sample standard deviation of normalized load forecast errors
$\tilde{\sigma}^{\chi,S}$	Sample standard deviation of normalized solar generation forecast errors
$\tilde{\sigma}^{\chi,W}$	Sample standard deviation of normalized wind generation forecast errors
$\tilde{\sigma}^{\partial r,L}$	Sample standard deviation of normalized load short-term fluctuation ramps
$\tilde{\sigma}^{\partial r,S}$	Sample standard deviation of normalized solar generation short-term fluctuation ramps
$\tilde{\sigma}^{\partial r,W}$	Sample standard deviation of normalized wind generation short-term fluctuation ramps
$\tilde{\sigma}^{r,L}$	Sample standard deviation of normalized load short-term fluctuations
$\tilde{\sigma}^{r,S}$	Sample standard deviation of normalized solar generation short-term fluctuations
$\tilde{\sigma}^{r,W}$	Sample standard deviation of normalized wind generation short-term fluctuations
$\underline{E}^{B}, \overline{E}^{B}$	Minimum and maximum energy capacity limit for battery [kWh]
$\underline{E}^{V,MC}$	Conservative energy capacity limit for virtual battery resulting from Monte Carlo simulation [kWh]
$\underline{PT}^{G}, \overline{PT}^{G}$	Minimum and maximum transient power capacity limit for thermal generators [kW]
$\underline{P}^{G}, \overline{P}^{G}$	Minimum and maximum steady-state power capacity limit for thermal generators [kW]

$\underline{P}^{V,C,MC}$	Conservative charging power limit for virtual battery resulting from Monte Carlo simulation [kW]
$\underline{P}^{V,D,MC}$	Conservative discharging power limit for virtual battery resulting from Monte Carlo simulation [kW]
$\varphi^{\chi}, \varphi^{r}$	ERU for forecast error and regulation reserves
C^{F}	Thermal capacitance of floor [J/°C]
C^{G}	Variable generation cost for thermal generators [USD/kWh]
C^{I}	Inner thermal capacitance of TCLs [J/°C]
C^{W}	Thermal capacitance of walls [J/°C]
C^{BR}	Battery replacement cost [USD/kWh]
C^{LS}	Load shedding costs [USD/kWh]
C^{NL}	No-load costs for thermal generators [USD/h]
C^{SD}	Shut-down costs for thermal generators [USD]
C^{SU}	Start-up costs for thermal generators [USD]
DT	Timescale for representing wall/floor thermal dynamics in decoupled thermal model (in the order of minutes to hours) [s]
E^{B}	Battery's rated energy capacity [kWh]
E^{V}	Energy capacity limit for virtual battery [kWh]
$E^{V,0}$	Initial stored energy in virtual battery [kWh]
f_0	System's nominal frequency [Hz]
IN^{B}	Virtual inertia constant for battery
IN^{G}	Rotational inertia provided by thermal generator [kJ]
IN^{SYS}	System's total rotational inertia [kJ]
K^{LD}	System's load damping stemming from frequency-sensitive loads

K^{PV}, K^{PF}	Voltage and frequency sensitivity of loads
K^{VFC}	Proportional gain of VFC
MN^{DN}	Minimum down time of thermal generators [min]
MN^{UP}	Minimum up time of thermal generators [min]
$p^{TCL,SS}$	Steady-state baseline TCL power consumption [kW]
$P^{V,C}, P^{V,D}$	Charging and discharging power limit for virtual battery [kW]
q^{C}	Heating power from solar radiation onto windows [W]
q^{W}	Heating power from solar radiation onto walls [W]
q^{EQ}	Equivalent heat power for decoupled thermal model [W]
R^{A}	Ambient thermal resistance of TCLs [°C/W]
R^{C}	Thermal resistance of windows [°C/W]
R^{F}	Thermal resistance of floor [°C/W]
R^{W}	Thermal resistance of walls [°C/W]
R^{EQ}	Equivalent thermal resistance for decoupled thermal model [°C/W]
RP_g^G	Ramp limit of thermal generators [kW/min]
S^0	Initial battery SoC
T^{FC}	Frequency controller time delay [s]
T_D^V	Communication delay for aggregate TCL control [s]
T_F^V	Time constant for Low-Pass Filter in Virtual Battery Controller

Variables

χ	Average power forecast error [kW]
χ^{MG}	Microgrid's net load forecast error [kW]
$\Delta\phi$	Expected increase in battery degradation due to reserve provision

Δe^{G}	Change in the expected average thermal generation due to reserve provision [kW]
Δf	Frequency deviation [Hz or p.u.]
ΔP^{G}	Change in power provided by thermal generators [kW or p.u.]
ΔP^{L}	Change in system's load [kW or p.u.]
$\Delta p^{B,C,\chi,\downarrow}$	Downward forecast error reserve provided by increasing battery charging power [kW]
$\Delta p^{B,C,\chi,\uparrow}$	Upward forecast error reserve provided by decreasing battery charging power [kW]
$\Delta p^{B,C,r,\downarrow}$	Downward regulation reserve provided by increasing battery charging power [kW]
$\Delta p^{B,C,r,\uparrow}$	Upward regulation reserve provided by decreasing battery charging power [kW]
$\Delta p^{B,D,\chi,\downarrow}$	Downward forecast error reserve provided by decreasing battery discharging power [kW]
$\Delta p^{B,D,\chi,\uparrow}$	Upward forecast error reserve provided by increasing battery discharging power [kW]
$\Delta p^{B,D,r,\downarrow}$	Downward regulation reserve provided by decreasing battery discharging power [kW]
$\Delta p^{B,D,r,\uparrow}$	Upward regulation reserve provided by increasing battery discharging power [kW]
$\Delta p^{G,\chi,\downarrow}$	Downward forecast error reserve provided by thermal generators [kW]
$\Delta p^{G,\chi,\uparrow}$	Upward forecast error reserve provided by thermal generators [kW]
$\Delta p^{G,r,\downarrow}$	Downward regulation reserve provided by thermal generators [kW]
$\Delta p^{G,r,\uparrow}$	Upward regulation reserve provided by thermal generators [kW]
$\Delta p^{PF,r,\downarrow}$	Downward regulation reserve provided by frequency sensitive loads [kW]

$\Delta p^{PF,r,\uparrow}$	Upward regulation reserve provided by frequency sensitive loads [kW]
Δp^{TCL}	Deviation from steady-state baseline TCL power consumption [W]
$\Delta p^{V,\chi,\downarrow}$	Downward forecast error reserve provided by virtual battery [kW]
$\Delta p^{V,\chi,\uparrow}$	Upward forecast error reserve provided by virtual battery [kW]
$\Delta p^{V,r,\downarrow}$	Downward regulation reserve provided by virtual battery [kW]
$\Delta p^{V,r,\uparrow}$	Upward regulation reserve provided by virtual battery [kW]
$\Delta p^{VFC,r,\downarrow}$	Downward regulation reserve provided by VFC [kW]
$\Delta p^{VFC,r,\uparrow}$	Upward regulation reserve provided by VFC [kW]
Δs^{B}	Change in the expected battery SoC due to reserve provision
$\hat{d}^{V}$	Virtual battery discharging power set-point for aggregate TCL controller (EMS decision variable) [kW]
$\hat{e}^{V}$	Virtual battery stored energy (EMS decision variable) [kWh]
$\hat{p}^{G}$	Average thermal generation set-point for a given dispatch time interval [kW]
$\hat{p}^{S}$	Forecast average solar generation for a given dispatch time interval [kW]
$\hat{p}^{W}$	Forecast average wind generation for a given dispatch time interval [kW]
∂r	Short-term power fluctuation ramp [kW/s]
∂r^{MG}	Microgrid's net short-term power fluctuation ramp [kW/s]
Φ	Expected total battery degradation
ρ, λ	Cycle count and depth resulting from cycle identification algorithm
Θ	Auxiliary variable representing the virtual stored energy in a TCL [J]
θ^{F}	Floor temperature [°C]
θ^{I}	Inner temperature of TCLs [°C]
θ^{W}	Wall temperature [°C]

$\varsigma^{B,\uparrow}, \varsigma^{B,\downarrow}$	Auxiliary variable for representing bilinear terms related to upward and downward regulation reserves from batteries [kW]
$\varsigma^{G,\uparrow}, \varsigma^{G,\downarrow}$	Auxiliary variable for representing bilinear terms related to upward and downward regulation reserves from thermal generators [kW]
ξ	Uncertainty
ζ^{χ}	Forecast error reserve requirement [kW]
$\zeta^{\partial r}$	Regulation-ramp reserve requirement [kW/s]
ζ^{r}	Regulation reserve requirement [kW]
c^B, d^B	Battery charging and discharging power [kW]
d^V	Virtual battery discharging power (negative for charging) [kW]
e^B	Battery stored energy [kWh]
e^V	Virtual battery stored energy [kWh]
ls	Average load shedding for a given dispatch time interval [kW]
p'^G, p'^B	Power effectively delivered by thermal generators and batteries (capacity limits enforced) [kW]
p^G, p^B	Instantaneous power reference provided to thermal generators and batteries (might violate capacity limits) [kW]
p^V	Instantaneous discharging power provided by virtual battery [kW]
p^{TCL}	TCL electric power consumption (continuous model) [W]
q^{TCL}	Heating (or cooling) power provided by TCL [W]
r	Short-term power fluctuations [kW]
r^{MG}	Microgrid's regulation signal stemming from short-term power fluctuations [kW]
s^B	Instantaneous battery SoC
u^G	ON/OFF status of thermal generators (binary)

u^{TCL}	ON/OFF status of TCLs (binary)
v^G	Start-up of thermal generators (binary)
w^G	Shut-down of thermal generators (binary)

Chapter 1

Introduction

1.1 Motivation

Modern power systems are currently undergoing a paradigm shift motivated by the search for cleaner and more efficient generation sources. In this context, DER are now being actively integrated in distribution networks, as these can enhance system efficiency, reduce carbon emissions, and improve system reliability. While the potential benefits of an increased DER integration are clear, directly controlling a large number of DER while maintaining an adequate security and reliability level in the system is particularly challenging. Thus, to tackle this, microgrids, which are defined as a collection of loads and DER that operate together locally as a single controllable entity, have been proposed as a tool to facilitate the integration and coordination of multiple DER [9].

In practical settings, microgrids typically use a hierarchical control to preserve the generation-load balance and guarantee a secure system operation. Under this approach, two control levels are considered: (i) an upper-level, in which the steady-state operational set-points for the system are determined based on global measurements of the network; and (ii) a lower-level, in which the set-points from the upper-level are used as inputs and necessary real-time adjustments are made based on local measurements. In the power systems literature, the upper-level controller is usually referred to as the EMS or Microgrid Central Controller, which can follow either a centralized or decentralized approach, with the former being preferred for isolated microgrids, and the latter for grid-connected microgrids [10]. This thesis focuses on isolated microgrids, as these face more challenging operation and control issues due to their lack of access to auxiliary services from the main bulk grid. Accordingly, centralized EMS are studied in the research presented here.

Unlike conventional bulk power systems, modern isolated microgrids have a low system inertia and significant renewable integration [11], making their operation and control particularly challenging. As discussed in [12], large second-to-second renewable power fluctuations can be observed for geographically-close plants, which when combined with a low system inertia, can result in poor frequency regulation [13]. Thus, modern EMS need to incorporate short-term power imbalances on their decision-making process, such that a continuous generation-load balance can be guaranteed on a second-to-second basis. Furthermore, modern EMS need to consider new modern flexible technologies, such as Energy Storage Systems (ESS) and DR, and their capability to manage such short-term imbalances.

ESS are by far one of the most important flexibility assets in a microgrid, as these possess the capability of shifting energy from one period to another, making them ideal for managing power imbalances. Nowadays, a wide spectrum of energy storage technologies are available, including electrochemical (e.g., lithium-ion batteries), mechanical (e.g., flywheels), and thermal (e.g., water tanks), amongst others [14]. In this research, these types of ESS will be referred as CESS, as these can already be found in microgrid applications and have well defined technical parameters (e.g., power and energy capacity limits). Furthermore, given the major role that electrochemical batteries play in modern power systems [7, 15], the term CESS will mainly be used to refer to BESS. However, it should be noted that the models developed in this research can easily be extended to other types of CESS.

Another relevant flexibility asset for microgrids is DR, which refers to utilizing available demand flexibility for an enhanced system operation. In the last years, a series of different programs and control strategies have been proposed to harvest demand flexibility, which have shown promising results for the management of power imbalances and the reduction of operating costs [16]. Within these, the aggregated control of TCL, such as air conditioners and water heaters, has gained popularity, as TCLs comprise a significant share of the total residential demand [17], and have the capability to manage fast second-to-second power imbalances without significantly affecting end-user comfort needs [18]. Although computational limitations prevent TCLs to be directly incorporated in operational models such as EMS, recent works have shown that these can be included in the system operation through the use of computationally efficient *virtual battery* models [6, 19–21], in which the flexibility of a TCL collection is characterized by a simple yet accurate battery-like model, thus establishing a direct analogy with CESS. Consequently, this type of load control will also be referred to as VESS throughout this thesis.

Based on the above discussion, the main objective of this thesis is to design a centralized EMS model for isolated microgrids that incorporates second-to-second fluctuations and

their impact on frequency dynamics, as well as the role that CESS and VESS can play to counter-balance such fluctuations. Although a wide literature can be found for centralized EMS for microgrids, only a limited amount of works can be found related to embedding second-to-second power imbalances and their impact on frequency regulation in the EMS's decision-making process. Furthermore, unlike previous works, this thesis discusses the application of VESS for the provision of energy shifting and frequency regulation services, and the potential benefits and practical challenges resulting from the combined integration of CESS and VESS in isolated microgrids.

1.2 Literature Review

In this section, a detailed literature review on topics related to EMS models, second-to-second power fluctuations, and frequency dynamics is presented. Furthermore, a comprehensive survey is presented on the incorporation of BESS, DR, and TCL within operational models, including VESS modeling.

1.2.1 EMS and Short-Term Fluctuations

Several centralized EMS models have been developed for the economic and secure operation of isolated microgrids, which have integrated advanced features such as phase imbalance [22], demand response [23], CO_2 emissions [24], power sharing [25], thermal energy resources [26], and network representations [27] (see [28] and [29] for a thorough literature review). In general, these models are deterministic and indirectly handle uncertainty in renewable generation and demand by means of a Model Predictive Control (MPC) with pre-definied reserve requirements. While this approach does provide some level of protection against uncertainty, there are no a-priori guarantees regarding the conservatiness or cost-efectiveness of such uncertainty management strategy.

To address the above issue, recent EMS models embedding the uncertainty of renewable generation and loads have been developed, which have used stochatic [30], robust [31] and distributionally robust [32] optimization techniques, as well as affine arithmetic techniques [33]. However, these works rely on the assumption that the time-variability and uncertainty in renewable generation and loads can be captured by assuming a constant, albeit uncertain, power during each of the dispatch time intervals (usually in the range of 5min to 1h), thus neglecting intra-dispatch fluctuations in the order of seconds. As previously mentioned, such second-to-second fluctuations are particularly relevant for modern

isolated microgrids, as these are particularly prone to poor frequency regulation due to their low-inertia and significant renewable penetration.

A few papers have studied the integration of short-term imbalances in microgrids EMS models, with these being mostly focused on grid-connected microgrids. In [34] and [35], two-stage open-loop EMS models are proposed for the management of short-term power imbalances, in which two decision-making stages are considered: (i) an upper stage with a low time resolution, in which optimal dispatch set-points are determined; and (ii) a lower stage with a higher time resolution, in which the dispatch set-points are used as inputs and short-term power fluctuations are managed. Under this approach, both stages are solved independently, i.e., in open-loop, and thus have the downside of not ensuring feasibility in the lower-stage in the presence of large and fast power fluctuations. To address this issue, [36] proposes a two-stage closed-loop EMS model, for which feasible dispatch set-points are determined by iteratively solving upper and lower stage problems through a constraint generation method, which adds constraints to the upper stage problem if infeasibilities are detected in the lower stage problem. Therefore, by following a closed-loop structure, this approach guarantees that the obtained solutions remain feasible even in the presence of large and fast power fluctuations. However, this results in a substantial increase in computational demand, as a large number of decision variables is needed for modeling detailed time resolutions. Accordingly, practical applications for this latter EMS model can only be found for minute-to-minute power fluctuations, as using a more detailed time resolution in the order of seconds would result in a computational intractable model. Furthermore, the EMS models in [34–36] are designed specifically for grid-connected microgrids, in which a large support and inertia from the main bulk grid is available, making their application to modern isolated microgrids impractical.

1.2.2 Embedding Frequency Dynamics in Operations

Another relevant aspect to integrate in modern microgrid EMS are frequency dynamics, as renewable power fluctuations can directly impact the frequency regulation in these systems [13]. The explicit modeling of frequency dynamics in operational models is a relatively new research area, with most of the existing literature being focused on the development of frequency-constrained Unit Commitment (UC) models for low-inertia bulk power systems (e.g., [37–41]). In general, these UC models are based on adding frequency-constraints to the optimization problem, such that large frequency excursions resulting from generator outages are avoided, as these are relatively common in bulk power systems with a large number of generators. However, none of these works consider the impact of

short-term renewable power fluctuations on the system's frequency regulation performance, which as previously discussed is a particularly relevant topic for isolated microgrids.

It is also important to highlight that none of the microgrid EMS models discussed in Section 1.2.1 incorporate frequency dynamics in their decission-making process, nor perform frequency transient simulations to validate that the obtained EMS dispatch instructions yield a satisfactory frequency regulation performance. This is particularly relevant issue for practical microgrid applications, as frequency transients can rapidly and significantly deviate from steady-state values in low-inertia systems with highly variable renewable energy sources (e.g., [13]).

1.2.3 Embedding BESS in Operations

Existing EMS models for isolated microgrids already incorporate some form of flexibility associated with BESS in their decision-making process (e.g., [22–32]). Nonetheless, these EMS models have focused exclusively on the energy shifting capability of BESS, neglecting their capability to also provide frequency regulation services, which are of particular interest for isolated microgrids due to their low-inertia and significant renewable integration (see Section 1.1). Furthermore, the degradation resulting from the repeated charging and discharging of BESS have generally been neglected on existing EMS models, based on the assumption that such degradation process is negligible on an operational scale. However, as recently demonstrated in [42, 43], BESS degradation can actually play a significant role in operations, as the repeated charging-discharging of BESS can significantly affect its lifespan and thus entail a relevant lost opportunity cost.

Based on the above discussion, modern EMS models need to incorporate frequency regulation services from BESS, while taking into account the degradation costs stemming from their repeated charging and discharging. Some previous works have integrated degradation costs within operational models; however, most of them have either oversimplified the degradation model by employing a fixed discharging-charging cost at rated conditions (e.g., [36, 44–46]), or overcomplicated the degradation model by using auxiliary binary variables to characterize discharging-charging cycles (e.g., [35, 47]), resulting in computational intensive models applicable only to small test systems. Exceptions can be found in the context of energy, reserve, and secondary frequency regulation markets [42, 48–50], where a good balance between degradation accuracy and computational tractability is achieved; however, these models have been developed for bulk power system applications, and thus need to be adapted for their implementation in microgrid EMS models.

1.2.4 Embedding DR and TCLs in Operations

The integration of DR within operational models, and in particular EMS, is still an active research field. Early works on DR integration within operations have used generic modeling approaches for characterizing load flexibility, which include price-elasticities [51], deferrable demand [52], load bidding curves [53], saturation curves [54], and neural networks [23], amongst others. In general, these models are characterized by their capability to describe a wide range of possible controllable loads; however, this comes at the cost of neglecting dynamics that are specific to a particular load type. This is a particularly relevant issue for TCLs, as these loads are directly affected by thermal dynamics, which need to be incorporated for an accurate modeling in practical implementations [55].

The incorporation of thermal TCL dynamics within operational models is a relatively new research area, with the direct incorporation of detailed thermal state-space models being one of the first approaches found in the power system literature (e.g., [56, 57]). While this approach has the advantage of a high thermal-modeling accuracy, it suffers from computational tractability issues when a large and diverse collection of TCLs is considered, as a significant number of decision variables and constraints for the corresponding optimization model are required in this case. To address this issue, computationally efficient VESS models representing the set of reference signals that can be followed by a large and diverse collection of TCLs have been proposed, which have been successfully implemented in operational models for bulk power systems [19, 20, 58–60]. However, the VESS models considered in these works are based on simple first-order thermal models, which can significantly differ from the actual thermal dynamics observed in real-life applications [61], leaving a pending research gap in this regard. Furthermore, these models have been developed in the context of bulk power systems, and thus need to be adapted to the isolated microgrids, where low-inertia and significant renewable integration play a major role.

1.2.5 Discussion

Based on the above literature review, modern EMS for isolated microgrids should incorporate second-to-second power fluctuations stemming from renewable generation and their impact on frequency dynamics. In this context, BESS and TCLs present a great flexibility potential to counter-balance such fluctuations, and thus their capabilities should also be integrated in microgrid EMS models. Accordingly, the following challenges must be addressed:

- Second-to-second power fluctuations from renewable energy sources and loads, as

well as their associated uncertainty, should be integrated in modern EMS models, as these can have a large impact on isolated microgrids due their low-inertia and significant renewable penetration. Existing EMS models either neglect short-term fluctuations, or use computationally demanding models that limit their application in a second-to-second time scale, leaving a pending research gap in this regard.

- The impact of second-to-second power imbalances on microgrid frequency dynamics should be incorporated in modern EMS models, as these can play a major role in isolated microgrids due their inherent fragility in terms of frequency regulation performance. While some previous works have studied frequency dynamics in the context of operations, these have focused exclusively on the frequency excursions caused by outages in bulk power systems. Thus, new models should be developed to capture the impact of short-term fluctuations on isolated microgrid frequency dynamics.

- Both energy shifting and frequency regulation capabilities of BESS, as well as the resulting degradation costs arising from the provision of these services, should be modeled in modern microgrid EMS. Furthermore, to enable potential practical implementations, emphasis should be put into balancing computational tractability and degradation modeling accuracy. While some previous works have achieved an adequate balance between these two aspects, they have been developed for bulk power system applications, and thus need to be adapted for their implementation in isolated microgrids.

- Both energy shifting and frequency regulation capabilities of TCLs, as well as their inherent thermal dynamics, should be modeled in modern EMS for isolated microgrids, as these type of loads play a significant role in microgrids. Furthermore, to enable potential practical applications with a large and diverse collection of TCLs, emphasis should be put into balancing computational tractability and thermal modeling accuracy, as existing previous works have either used detailed but computationally inefficient formulations, or too simplistic approaches that significantly differ from the actual dynamics observed in practical settings.

- Finally, the joint operation of both BESS and TCLs for the provision of energy shifting and frequency regulation services should be studied while taking into account their associated practical challenges. Previous works have either studied BESS and TCL independently, or neglected the practical challenges of battery degradation, TCL thermal dynamics, and computational tractability. Thus, the joint operation of BESS and TCLs taking into account their practical challenges are yet to be analyzed.

1.3 Research Objectives

Based on the aforementioned literature review, the following objectives have been defined for the present thesis:

- Develop a mathematical model for characterizing second-to-second power fluctuations stemming from renewable generation and loads, while taking into account their impact on isolated microgrid operation and frequency regulation. The resulting model must preserve computational tractability, such that it can be integrated within practical microgrid EMSs.
- Develop mathematical models to characterize the energy shifting and frequency regulation capabilities of BESS and TCLs, taking into account the practical issues of battery degradation, TCL thermal dynamics, and computational tractability.
- Determine optimal operational policies for a centralized EMS in the context of isolated microgrids, taking into account the flexibility and practical issues of BESS and TCL, while maintaining computational tractability.
- Evaluate the performance of the determined operational policies through simulations in a realistic test system, gaining insights into the benefits that BESS and TCL can provide for isolated microgrid operation.

1.4 Thesis Outline

The rest of the thesis is organized as follows:

- In Chapter 2, a thorough review on the background topics relevant to this thesis are presented, including microgrids and EMS, frequency dynamics and control, BESS and their degradation, and TCL and virtual battery modeling.
- In Chapter 3, computationally efficient models for representing short-term power fluctuations and battery degradation are developed, which are then used to design a practical microgrid EMS model embedding these features. Computational experiments on two realistic isolated microgrids are performed to evaluate the benefits of the proposed EMS model, highlighting the need for integrating short-term fluctuations and battery degradation in isolated microgrid operations.

- In Chapter 4, a frequency-constrained EMS model is proposed, in which the impact of short-term imbalances on the frequency regulation performance of the microgrid is integrated. To maintain computational tractability for potential practical applications, accurate linear equations are used to describe microgrid frequency dynamics, which include frequency deviations, RoCoF, and regulation provision from DER units. Detailed dynamic simulations are performed on a realistic test microgrid to demonstrate the benefits of the proposed frequency-constrained EMS model, highlighting the need for integrating frequency dynamics in isolated microgrid operations.

- In Chapter 5, the integration of TCLs within an isolated microgrid EMS model is studied. For this purpose, practical and precise models representing the flexibility and dynamics of aggregated TCL control implementations are developed; namely, a virtual battery model integrating high-order thermal dynamics for TCLs, and a frequency transient model capturing relevant challenges observed in practical applications. Computational experiments using detailed frequency transient and thermal models are performed to demonstrate the accuracy of the proposed aggregated TCL models, as well as the economic and reliability benefits stemming from their integration within a microgrid EMS model.

- In Chapter 6, the main conclusions and contributions of the thesis are summarized, and future research ideas are discussed.

Chapter 2

Background

In this chapter, an overview of the concepts and models used in this thesis is presented. First, microgrids and the role that EMS play in their operation are discussed. CESS and their different available technologies are then presented, including BESS and their degradation. TCL and existing virtual battery representations are reviewed next, followed by a discussion of the mathematical models used to describe the frequency dynamics and control of microgrids. Finally, a summary of the topics discussed in this chapter is presented.

2.1 Microgrids

Microgrids are defined as a collection of loads and DER, such as ESS and renewable energy sources, that operate locally as a single controllable entity. While small autonomous microgrids have existed for many decades in remote communities, there has been a recent growing interest in microgrids, as these systems can facilitate the integration of DER in modern power systems [9]. Microgrids can have an AC, DC, or hybrid AC-DC topology, with AC being the most frequent topology found in practical settings [62]. Thus, the present thesis focuses on AC microgrids, as these are the most common nowadays.

Unlike conventional power systems, microgrids have a set of particular features that need to be considered for its operation and control; namely, smaller system size, higher share of renewable energy sources, higher uncertainty in generation and demand, lower system inertia, higher R/X ratio of the feeders, unbalanced three-phase loading, and limited short-circuit capacity. All these features directly affect the stability of the microgrid, making its operation and control particularly challenging [11]. Microgrids can operate in

either grid-connected or stand-alone modes. In the grid-connected mode, the microgrid is directly connected to the main bulk grid at a single point of connection commonly referred as the Point of Common Coupling. In this case, voltage and frequency are mainly imposed by the main bulk grid and power deficit/excess can be traded with it, facilitating the operation and control of the microgrid. In contrast, in stand-alone mode, the microgrid must control voltage and frequency on its own, as well as handle power unbalances within; thus, microgrid operation in stand-alone mode is a more challenging task. Microgrids that do not have a Point of Common Coupling, and thus are forced to continuously operate in stand-alone mode, are referred to as *isolated microgrids* [10]. The present thesis focuses on these type of microgrids, as system operation and control is more challenging in this case.

To ensure a secure and efficient operation, microgrids usually employ a hierarchical control for generation-load balance. Under this approach, microgrid control is divided in the following three levels, which differ based on the considered time frame and speed of response [10]:

- *Primary control* is the fastest of the three levels of controls, and its based exclusively on local measurements, requiring no communication infrastructure. This level includes output controls, power sharing, and droop controls.
- *Secondary control* ensures the reliable and economic operation of the microgrid. In this level, system-wide frequency and voltage regulation is performed, which includes the UC and dispatch of the microgrid's DER units. This is the highest level of control for isolated microgrids and is commonly referred to in the literature as EMS or Microgrid Central Controller.
- *Tertiary control* handles the coordination with the main bulk grid and/or other microgrids. This level of control is only present in grid-connected mode.

The present thesis focuses on the secondary control of isolated microgrids, in particular in EMS model design. However, the effect of primary control is also considered in this research, as it plays a major role in the frequency dynamics of the microgrid. Tertiary control is not discussed in this thesis, since it is not present in isolated microgrids.

2.1.1 Energy Management Systems

EMS in microgrids have the task of determining the schedule and dispatch set-points of the system's DER units, while taking into account the microgrid's unique characteristics.

EMS can either follow a decentralized or centralized approach for determining and communicating the dispatch set-points of the different DER units, which can be described as follows [10]:

- Under the decentralized approach, the autonomy of the different DER units and loads is prioritized, and thus the set-points are determined by a distributed decision making process, making this approach ideal for grid-connect microgrids with multiple owners and a fast-changing number of DER units.
- Under the centralized approach, a central controller collects global measurements of the microgrid and determines the corresponding set-points for the different DER devices. This enables the use of optimization algorithms that directly incorporate the coupling dynamics between the operation of the different devices, allowing a reliable system coordination. Thus, this approach is usually preferred in isolated microgrids, where generation-load balance is critical and the infrastructure of the network remains relatively fixed.

Given that the focus of this research is in isolated microgrids, a centralized approach is considered henceforth.

2.1.2 The Unit Commitment Problem

Centralized EMS can be described as a type of UC problem, in which the schedule and dispatch set-points of the microgrid's DER units needs to be determined. This is achieved by solving an optimization problem within the central controller based on previously collected global measurements. In general, the UC problem has the following structure [63–65]:

$$\begin{aligned} \min_{\boldsymbol{x},\boldsymbol{y}} \quad & \mathcal{F}^{OBJ}\left(\boldsymbol{x},\boldsymbol{y}\right) \\ \text{s.t.} \quad & \boldsymbol{x} \in \{0,1\}\,,\ \boldsymbol{y} \geq 0 \\ & \boldsymbol{\mathcal{F}}^{IN}(\boldsymbol{x},\boldsymbol{y}) \leq 0 \\ & \boldsymbol{\mathcal{F}}^{EQ}(\boldsymbol{x},\boldsymbol{y}) = 0 \end{aligned}$$

where $\boldsymbol{x}$ are binary decision variables, which are typically related to the ON/OFF dispatch decisions for thermal generators; $\boldsymbol{y}$ are non-negative continuous decision variables, which include DER dispatch set-points and line flows; $\mathcal{F}^{OBJ}(\cdot)$ is a scalar objective function, which incorporates relevant operation costs such as fuel, maintenance, start-up, and shut-down costs; $\boldsymbol{\mathcal{F}}^{IN}(\cdot)$ are inequality constraints, which are typically related to DER capacity

limits; and $\boldsymbol{\mathcal{F}}^{EQ}(\cdot)$ are equality constraints, which are usually linked to the physics and dynamics of the decision variables and parameters (e.g., power flow equations). Typically, UC models utilize linear expressions for the objective function $\mathcal{F}^{OBJ}$, and constraints $\boldsymbol{\mathcal{F}}^{IN}$ and $\boldsymbol{\mathcal{F}}^{EQ}$, such that a Mixed Integer Linear Programming (MILP) problem is obtained, allowing the use of highly efficient off-the-shelf solvers, such as Gurobi [66] and CPLEX [67].

2.2 Conventional Energy Storage Systems

ESS are a relevant flexibility asset for isolated microgrids, as these cannot only provide energy shifting services, but also a series of other relevant auxiliary services, such as frequency and voltage regulation, power quality improvement, and grid-forming capability. A wide spectrum of different energy storage technologies can be found nowadays, which include [14, 15]:

- *Electrochemical storage*, in which an electrochemical process is used to transform and store electrical energy as chemical energy. Within this category, lithium-ion, lead-acid and flow batteries are the most typical nowadays. This type of storage is characterized by its great flexibility and widespread application in different fields, including electric vehicles and power systems.

- *Mechanical storage*, in which electrical energy is transformed and stored as kinetic or potential energy. Within this category, pumped hydro, compressed air, and flywheel energy storage are the most common.

- *Thermal storage*, in which heat is stored in an insulated repository for space heating/cooling or hot water production. Within this category, water tanks and ceramic brick packed-beds are typical.

- *Electrical storage*, in which electrical energy is stored by means of capacitors and magnetic fields. Within this category, supercapacitors and superconducting magnetic energy storage can be found. This type of storage is characterized by high power capacity, low energy density, and high investment cost, which limits its application to time frames in the order of seconds.

- *Hydrogen storage*, in which electricity and hydrogen interact through the use of an electrolizer and a fuel cell. Unlike other storage technologies, this type of storage allows seasonal storage.

In this thesis, these type of energy storage technologies are referred to as CESS, as these have successfully been implemented in power system applications and have well defined technical parameters (e.g., power and energy capacity limits). Thus, CESS can be described by the following discrete-time linear equations $\forall t \in \mathcal{T}$ [68]:

$$e_t^B = e_{t-1}^B + \Delta t \left(\eta^{B,C} \, c_t^B - \frac{1}{\eta^{B,D}} \, d_t^B \right) \tag{2.1}$$

$$\underline{E}^B \leq e_t^B \leq \overline{E}^B \tag{2.2}$$

$$c_t^B \leq \overline{P}^B, \quad d_t^B \leq \overline{P}^B \tag{2.3}$$

where Δt is the time-step size; $c_t^B \geq 0$ and $d_t^B \geq 0$ are the charging and discharging power at time t; $e_t^B \geq 0$ is the stored energy at the end of period t; $\mathcal{T}$ the set of time intervals; $\eta^{B,C}$ and $\eta^{B,D}$ are the charging and discharging efficiency; $\underline{E}^B$ and $\overline{E}^B$ are the minimum and maximum energy capacity limit; and $\overline{P}^B$ is the maximum rated charging/discharging power, respectively. Equation (2.1) describes the SoC evolution over time, and equations (2.2) and (2.3) represent the capacity limits for stored energy and charging/discharging power, respectively. The present thesis focuses on electrochemical batteries, i.e., BESS, as it is one of the most flexible and widespread CESS technologies found in power systems applications [7, 15]. However, modelling of and insights on BESS can readily be extended for other type of CESS.

2.2.1 Battery Energy Storage Systems

Electrochemical batteries are typically composed by an anode, a cathode, an electrolyte, and a semipermeable membrane, which are used to trigger a chemical redox process to store and deliver electric energy, as illustrated in Figure 2.1. A wide spectrum of commercial-scale electrochemical batteries can be found in practical applications, including Lead-Acid, Nickel-Metal-Hydride (NiMH), Lithium-Ion (Li-Ion), Sodium-Sulphur (NaS), and Vanadium Redox Flow Battery (VRB); each one has its own particular set of features, as shown in Table 2.1. Due to their high energy/power density, efficiency, and useful life, Li-Ion batteries are currently the most popular type of BESS found in power systems, having been applied in the provision of numerous services, such as energy shifting, frequency and voltage regulation, and transmission/distribution updgrade deferral. Furthermore, Li-Ion batteries are the main technology for modern electric vehicles; however, their wide-scale application in power systems is currently still limited due to their high capital costs, which are expected to decrease in the near-future [7].

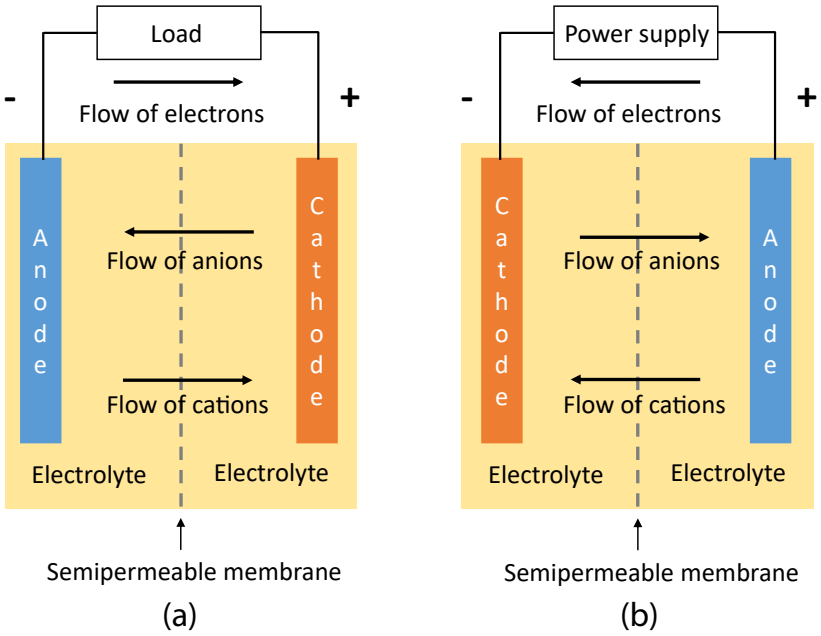

Figure 2.1: Typical discharging (a) and charging (b) process of an electrochemical battery [1].

2.2.2 Battery Degradation and Aging

As batteries require a high initial investment for their installation, proper quantification techniques for the battery's useful life are required to ensure an efficient energy storage planning and operation. Battery lifetime depends on a series of external stress factors that degrade and age its components, which include cycle Depth-of-Discharge (DoD), current rate, average SoC, calendar time, and cell temperature. From an operational point of view, such degradation translates into a fading of the battery's original capacity, with a 20% capacity fading being the usual threshold used to define battery end-of-life [43, 69].

In general, existing battery degradation models can be classified into three main categories, which differ in their degradation modelling accuracy and computational tractability, as follows:

- *Theoretical models* focus on modelling the active material and ion-diffusion loss by means of partial differential equations [70, 71]. These models have the highest accuracy in modelling battery degradation, but at the expense of a high computational

Table 2.1: Main features of common electrochemical batteries [7].

Type	**Lead-Acid**	**NiMH**	**Li-Ion**	**NaS**	**VRB**
Energy density [Wh/kg]	25-50	60-120	75-200	150-240	10-30
Power density [W/kg]	75-300	250-1,000	500-2,000	150-230	80-150
Useful life [n° cycles]	200-1,000	180-2,000	1,000-10,000	2,500-4,000	>12,000
Capital cost [USD/kWh]	100-300	900-3,500	300-2,500	300-500	150-1,000
Round-trip efficiency [%]	75-87	∼65	85-97	75-90	75-90
Self discharge	Low	High	Medium	-	Negligible

burden. Thus, these type of models cannot be directly incorporated within operational models.

- *Empirical models* are based exclusively on experimental data and statistical analysis, greatly simplifying the degradation model [48, 72, 73]. These models are highly computationally efficient, but have the drawback that they are tailored to specific test conditions, and thus their predictions can be very poor for other battery operating conditions.

- *Semi-empirical models* combine theoretical analysis with experimental observations to tackle the issues of computational tractability and performance under general battery operating conditions [43, 69]. Under this approach, degradation is modelled through theoretical stress factor models whose parameters are calibrated with experimental data.

This thesis focuses on the semi-empirical approach, as its computational tractability and general applicability makes it ideal for operational applications, such as EMS model design. Under this approach, the degradation is mainly driven by: (i) cycle aging, which captures the degradation due to the battery's continuous charging and discharging; and (ii) calendar aging, which represent the battery's inherent degradation over time. In general, both cycle and calendar aging can be described as a function of the cycle's DoD λ and count ρ, cell

temperature θ^C, average SoC $\hat{s}^B$, and time t stress factors, as follows [43]:

$$\mathcal{F}^{CYC}(\theta^C, \hat{s}^B, \boldsymbol{\rho}, \boldsymbol{\lambda}) = \Gamma^{\theta}(\theta^C)\,\Gamma^{S}(\hat{s}^B) \sum_{m \in \mathcal{M}} \rho_m\,\Gamma^{\lambda}(\lambda_m) \tag{2.4}$$

$$\mathcal{F}^{CAL}(\theta^C, \hat{s}^B, t) = \Gamma^{\theta}(\theta^C)\,\Gamma^{S}(\hat{s}^B)\,\Gamma^{T}(t) \tag{2.5}$$

where $\mathcal{F}^{CYC}(\cdot)$ and $\mathcal{F}^{CAL}(\cdot)$ represent cycle and calendar aging, respectively; and $\Gamma(\cdot)$ is the stress factor model representing the effect of the stress factors on the battery's life, which are assumed to be multiplicative. Note that the cycles are indexed by $m \in \mathcal{M} = \{1, \ldots, M\}$ and are characterized by their depth $\lambda_m \geq 0$, and count $\rho_m \in \{0.5, 1\}$, for which $\rho_m = 0.5$ corresponds to a half cycle, and $\rho_m = 1$ to a full cycle.

Given that the focus of this research its on microgrid operations, the degradation process described by (2.4) and (2.5) can be simplified to facilitate its integration in microgrid EMS models. In particular, the presence of external controllers regulating the average SoC $\hat{s}^B$ and cell temperature θ^C can be assumed, making cycle aging the main driver of battery degradation [42, 49]. Thus, the degradation caused by battery operation can be described by the following equation:

$$\mathcal{F}^{CYC}(\boldsymbol{\rho}, \boldsymbol{\lambda}) = \sum_{m \in \mathcal{M}} \rho_m\,\Gamma^{\lambda}(\lambda_m) \tag{2.6}$$

where it can be seen that a cycle identification algorithm is needed for determining the set of cycles $\mathcal{M}$, and their corresponding depth λ_m and count ρ_m. In general, such cycle identification algorithm can be described as a function of the SoC profile $\boldsymbol{s}^B \in [0, 1]^n$ resulting from battery operation, as follows:

$$[\boldsymbol{\rho},\, \boldsymbol{\lambda}] = \boldsymbol{\mathcal{F}}^{ID}(\boldsymbol{s}^B) \tag{2.7}$$

where $\boldsymbol{\lambda}$ and $\boldsymbol{\rho}$ are vectors representing the resulting cycle depths and counts, respectively, with their dimension being equal to the number of cycles, i.e., $\dim(\boldsymbol{\lambda}) = \dim(\boldsymbol{\rho}) = M$.

Cycle identification algorithms based on the rainflow cycle counting method, such as the ones presented in [74,75], have commonly been used for battery life estimation applications (e.g., [42, 43, 49]). Under this approach, cycles are identified based on local extremas of the SoC profile, which are referred to as turning/reversal points. Thus, based on a time series of such reversal points, cycles are identified and classified either as full ($\rho_m = 1$) or half ($\rho_m = 0.5$) cycles, and assigned a corresponding cycle depth λ_m. An illustrative example of the application of the rainflow cycle counting algorithm is presented in Figure 2.2, for which the `rainflow` function in MATLAB [74,76] was used to identify the resulting charging/discharging cycles. Observe that a total of $M = 5$ cycles are identified, whose resulting cycle count and depth are indicated in Table 2.2.

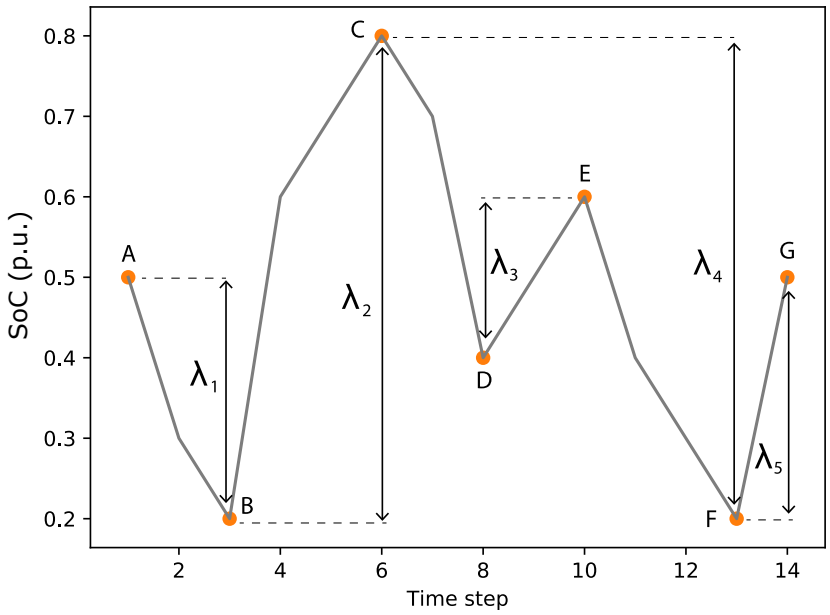

Figure 2.2: Example of rainflow cycle counting algorithm for cycle identification based on a battery's SoC profile ($M = 5$). Orange circles indicate turning/reversal points.

Table 2.2: Results of the rainflow cycle-counting algorithm example in Figure 2.2 ($M = 5$).

Reversal points	**A-B**	**B-C**	**D-E**	**C-F**	**F-G**
Cycle depth (λ_m)	0.3	0.6	0.2	0.6	0.3
Cycle count (ρ_m)	0.5	0.5	1	0.5	0.5

2.3 Thermostatically Controlled Loads

TCLs encompass air conditioners, refrigerators, electric space heaters, and electric water heaters, all of which comprise a significant share of the total electric demand at a residential level [17]. TCLs are characterized by their inherent thermal inertia, which allows temporary adjusting their electricity consumption without violating end-user temperature comfort requirements [18]. For residential TCLs, end-user temperature requirements take the form of a temperature deadband in which the device's temperature must be maintained at all times, for which a simple hysteresis ON/OFF control is typically employed in practice. Accordingly, the following equations have commonly been used in the power systems

literature to describe TCL dynamics [6, 19, 20, 77–79]:

$$C^I \frac{d\theta^I(t)}{dt} = \frac{\theta^A - \theta^I(t)}{R^A} \pm \underbrace{u^{TCL}(t)\, \eta^{TCL}\, \overline{P}^{TCL}}_{q^{TCL}(t)} \tag{2.8}$$

$$\lim_{\epsilon \to 0} u^{TCL}(t+\epsilon) = \begin{cases} u^{TCL}(t), & \left|\theta^I(t) - \theta^{I,SP}\right| < \Delta\theta^{TCL} \\ 1 - u^{TCL}(t), & \left|\theta^I(t) - \theta^{I,SP}\right| \geq \Delta\theta^{TCL} \end{cases} \tag{2.9}$$

where (2.8) describes the dynamics of the TCL's inner temperature θ^I, which is affected by the ambient temperature θ^A and the TCL's ON/OFF status $u^{TCL} \in \{0, 1\}$; and (2.9) describes the TCL's hysteresis ON/OFF control, which ensures the TCL's inner temperature θ^I stays within the deadband defined by the temperature set-point $\theta^{I,SP}$ and deadband width $\Delta\theta^{TCL}$. Parameters C^I, R^A, η^{TCL}, and $\overline{P}^{TCL}$ represent the TCL's inner thermal capacitance, ambient thermal resistance, coefficient of performance, and rated electric power, respectively, which depend on the thermal and electric characteristics of the TCL. Furthermore, observe that (2.8) includes a $\pm$ sign to differentiate of whether the TCL is operating in heating (+) or cooling (−) mode. The relatively low mathematical complexity of this model has allowed its use for simulating a large collection of TCLs (around 1000-2000 TCLs in [6, 19, 77–79]).

2.3.1 Aggregated Load Control and Virtual Battery Models

While TCLs cannot provide much flexibility on their own, a coordinated cluster of multiple TCLs can instead provide a significant amount of flexibility. Consequently, a series of different aggregated TCL controllers have been proposed, which aim to accurately coordinate a TCL collection to follow an aggregate power reference signal, and are based on advanced control techniques such as decentralized stochastic control [80], population-bin linear state-space models [77, 81], and priority-list control [6]. As demonstrated in these works, if an adequate level of sensing and communications is available, modern aggregated TCL controllers can achieve a satisfactory signal tracking performance, allowing its implementation for frequency regulation services. However, these controllers cannot be directly implemented in operational models, such as EMS, as it would result in a computational untractable optimization model with too many decision variables and constraints. Thus, to tackle this issue, computationally efficient VESS models have recently been proposed as a tool for modeling the flexibility of a TCL aggregation. This alternative representation is based on characterizing the set of reference signals that can be tracked by aggregated

TCL controller through an equivalent SoC equation with time-varing and uncertain energy/power capacity limits [6, 19–21], as follows $\forall t \in \mathcal{T}$:

$$e_t^V = \left(1 - \gamma^V \Delta t\right) e_{t-1}^V - \Delta t \cdot d_t^V \tag{2.10}$$

$$-E_t^V(\xi) \leq e_t^V \leq E_t^V(\xi) \tag{2.11}$$

$$-P_t^{V,C}(\xi) \leq d_t^V \leq P_t^{V,D}(\xi) \tag{2.12}$$

where d_t^V and e_t^V are the virtual battery's discharging power and stored energy, respectively, and γ^V is the self-discharging rate. Note that, unlike CESS capacity limits (2.2) and (2.3), the capacity limits (2.11) and (2.12) depend on the time t and uncertainty variable ξ. Given the similarity of the above virtual battery model to the CESS model (2.1)-(2.3), the term VESS will be used hereinafter to refer to this representation of the flexibility resulting from an aggregated TCL control.

2.3.2 High-Order Thermal Models

Existing works on aggregated TCL control and virtual battery representations typically assume that TCL thermal dynamics are accurately described by (2.8), which corresponds to a simple first-order thermal model that captures the interaction between the TCL's inner temperature θ^I and ambient temperature θ^A, as illustrated in Figure 2.3. However, as demonstrated in [61], these simple first-order dynamics are not sufficiently accurate to represent the actual dynamics observed in real-life applications, for which additional relevant aspects need to be incorporated, such as solar irradiance heat gains and wall/floor heat transfers. Thus, recent works on TCL control such as [82, 83] have proposed the use of more detailed high-order thermal models that integrate these additional features, which can be described by the following third-order system of differential equations, as per Figure 2.4:

$$C^I \frac{d\theta^I(t)}{dt} = q^{TCL}(t) + q^C + \frac{\theta^A - \theta^I(t)}{R^C} + \frac{\theta^W(t) - \theta^I(t)}{R^W/2} + \frac{\theta^F(t) - \theta^I(t)}{R^F/2} \tag{2.13a}$$

$$C^W \frac{d\theta^W(t)}{dt} = q^W + \frac{\theta^A + \theta^I(t) - 2\theta^W(t)}{R^W/2} \tag{2.13b}$$

$$C^F \frac{d\theta^F(t)}{dt} = \frac{\theta^G + \theta^I(t) - 2\theta^F(t)}{R^F/2} \tag{2.13c}$$

where θ^W and θ^F are wall and floor temperatures, respectively; q^C and q^W are the heating power from the solar radiation onto windows and walls, respectively; R^C is the thermal

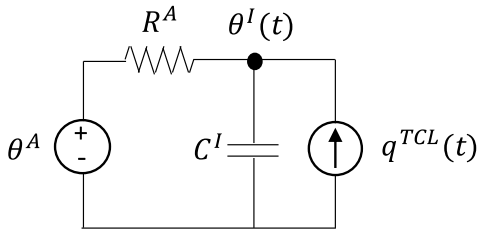

Figure 2.3: Thermal circuit for first-order TCL thermal model.

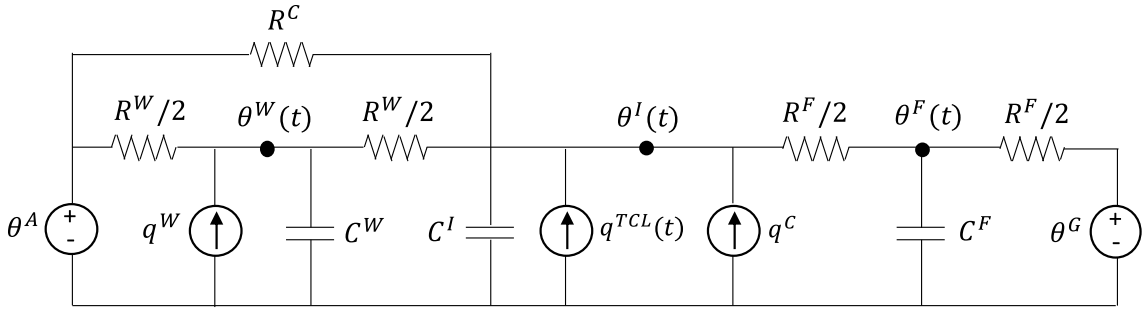

Figure 2.4: Thermal circuit for third-order TCL thermal model.

resistance of windows; R^W and C^W are the thermal resistance and thermal capacitance of walls, respectively; R^F and C^F are the thermal resistance and capacitance of the floor, respectively; and θ^G is the ground temperature. The high modeling accuracy of the above thermal model has allowed the detailed evaluation of possible practical applications of small-scale TCL controls (e.g., [82, 83]). However, due to its relatively high mathematical complexity, it has not been yet applied in studies with a large number of TCLs nor VESS models.

2.4 Frequency Dynamics and Control

Frequency control plays a fundamental role for ensuring a secure system operation, as generation units and electric loads need a relatively stable system frequency for their correct functioning. Frequency deviations are the result of instantaneous generation-load power imbalances, which stem from diverse sources such as generator/line outages and fast short-term fluctuations in renewable generation and demand. In general, the instantaneous frequency deviation Δf resulting from a power imbalance ΔP^{IMB} can be described by the

following swing equation [84, 85]:

$$2\,IN^{SYS}\,\frac{d\Delta f(t)}{dt} + K^{LD}\,\Delta f(t) = \Delta P^{IMB} = \sum_{g\in\mathcal{G}} \Delta P_g^G(t) - \Delta P^L(t) \tag{2.14}$$

where IN^{SYS} is the system's total rotational inertia; K^{LD} is the system's total load-damping stemming from frequency-sensitive loads; ΔP_g^G is the change in generator's g power; and ΔP^L is the change in the system's load. Thus, an excess of generation ($\Delta P^{IMB} > 0$) will result in a temporary increase in frequency, and a generation shortage ($\Delta P^{IMB} < 0$) will translate in a frequency decay.

To prevent large frequency excursions that could affect the system's correct operation, primary frequency controllers are typically included in the generation units of modern power systems, being the droop control the most common approach found in practical applications. Under this approach, the power reference of each generator $g \in \mathcal{G}$ is adjusted based on the system's frequency deviation and an specific droop gain κ_g^G, resulting in the following linear power-frequency relationship [84, 85]:

$$\Delta P_g^{G,REF}(t) = -\frac{1}{\kappa_g^G}\,\Delta f(t) \tag{2.15}$$

where $\Delta P_g^{G,REF}$ is the change of generator's g power reference/set-point. The main advantage of the above droop control lies in its decentralized nature, for which only local frequency measurements are required, resulting in a robust yet simple frequency control method. Furthermore, droop control allows a coordinated steady-state power sharing amongst the different generators connected to the system, which will be dictated by droop gain κ_g^G and rated power of each generator. In practical settings, droop gains are typically determined based on operation guidelines such as [86], for which maximum allowable frequency deviations and range of acceptable droop gains are indicated.

With the exception of microgrids with a limited number of generators, local primary droop controllers are typically supported by an additional supplementary frequency control. For conventional power systems, such supplementary control takes the form of an Automatic Generation Control (AGC) scheme, which allows correcting the steady-state frequency error of a droop-only control. An example of a standard AGC implementation is illustrated in Figure 2.5, for which an integral component has been considered for the supplementary frequency control [84, 85]. Note that in the figure, the supplementary control signal ΔP^{AGC} is distributed amongst the different units based on participation factors α_g^G.

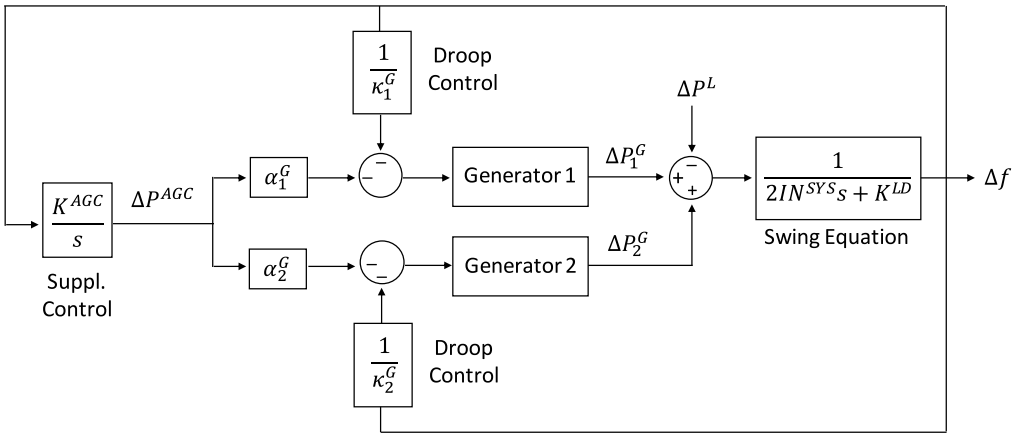

Figure 2.5: Example of AGC frequency control scheme based on local droop control and supplementary integral control.

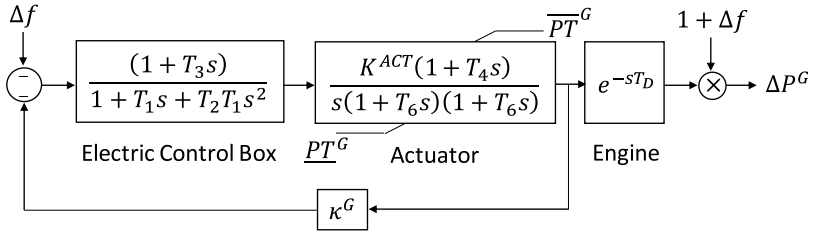

Figure 2.6: Block diagram of diesel generator governor model DEGOV1 [2].

2.4.1 Generator and Battery Dynamic Models

Due their flexibility and low investment cost, diesel generators are by far the most common type of generator found in microgrids. Thus, in this thesis, a frequency dynamic model for a diesel generator is considered, which is based on its governor's response and includes an Electronic Control Box, Actuator, and Engine as described by Figure 2.6 [2]. Note that in the figure, a feedback loop for a steady-state frequency-droop response is included.

BESS are also typically found in modern practical microgrids, as these can provide relevant grid services such as frequency regulation and grid-forming capability [7, 15]. Thus, in this thesis, a frequency dynamic model for BESS is also considered, which is illustrated in Figure 2.7 and it is based on WECC's generic modules REPC_A, REEC_A, and REGC_A [3]. Note that the presented model captures the frequency response and

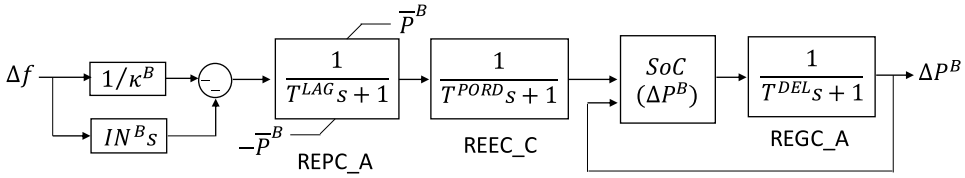

Figure 2.7: Block diagram of battery frequency response model [3].

time lags resulting from the battery's converter and inner control loops, and includes a frequency-droop response κ^B, a virtual inertia component IN^B, and a SoC limit function $SoC\left(\Delta P^B\right)$, which automatically ceases battery (dis)charging if the upper (lower) energy limit is reached.

2.4.2 Load Model and Voltage Frequency Control

Electric loads can be modelled based on their aggregate sensitivity to frequency and voltage changes. Typically, the following static load model has been used for representing active power loads at a distribution level [84, 85]:

$$P^L(t) = P_0^L \left(V(t)\right)^{K^{PV}} \left(1 + K^{PF}\,\Delta f(t)\right) \tag{2.16}$$

where P^L and V are the instantaneous load and voltage, respectively; P_0^L is the nominal load; and K^{PV} and K^{PF} are voltage and frequency sensitivities of the electric loads, respectively. Note that the system's load damping K^{LD} in (2.14) stems from the above frequency sensitivity, with $K^{LD} = P_0^L\ K^{PF}$.

The voltage sensitivity described in (2.16) can also be exploited to provided additional frequency regulation to isolated microgrids. This can be achieved by installing a Voltage Frequency Control (VFC) in the microgrid's diesel generators, which modifies the generator's voltage reference based on measured frequency deviations [4]. This results in the frequency dynamic model illustrated in Figure 2.8, where K^{VFC} and $\overline{\Delta V}$ are the VFC's proportional gain and maximum voltage reference change; and V^G represents the aggregated dynamic response of the generator's Synchronous Machine (SM) and Exciter.

2.4.3 Load Shedding and Renewable Curtailment Models

To prevent system collapse in the presence of unexpectedly large and fast power imbalances, auxiliary Load Shedding (LS) and Renewable Curtailment (RC) controllers are typically

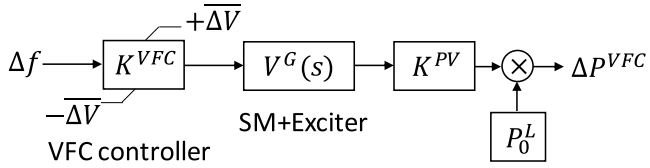

Figure 2.8: Block diagram of a proportional Voltage Frequency Controller [4].

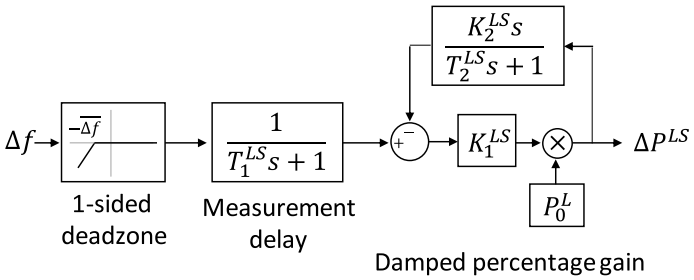

Figure 2.9: Block diagram of load shedding frequency control scheme.

included in isolated microgrid applications [86, 87]. Thus, in this thesis two simple linear percentage-based LS and RC controllers are included for frequency transient simulations, which are depicted in Figures 2.9 and 2.10, respectively. Note that both controllers include damped percentage gains, which depend on nominal load P_0^L, wind generation P_0^W, and solar generation P_0^S. Furthermore, observe that in accordance with modern DER operating standards [86], these controllers are triggered when the upper or lower frequency deviation limits $\pm\overline{\Delta f}$ are reached.

2.4.4 Isolated Microgrid Dynamic Model

Based on the aforementioned dynamic models, a transient model to describe the frequency dynamics of an isolated microgrid can be developed. The resulting dynamic model is presented in Figure 2.11, which includes blocks for representing the transient response of diesel generators and batteries, as well as the control response of VFC, LS and RC controllers. Note that in the figure, continuous-time functions for representing short-term fluctuations in loads $r^L(t)$, wind generation $r^W(t)$, and solar generation $r^S(t)$ are integrated.

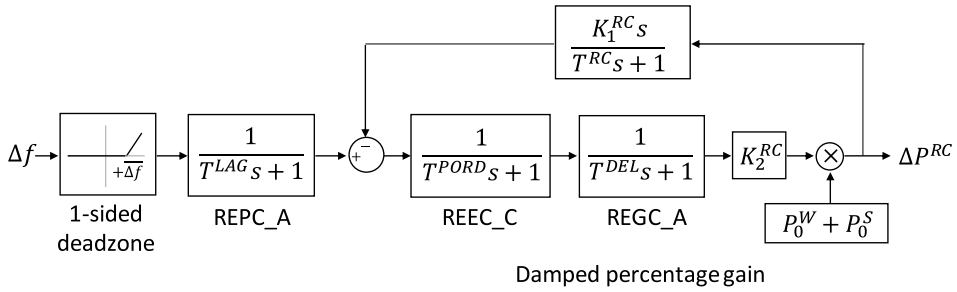

Figure 2.10: Block diagram of renewable curtailment frequency control scheme.

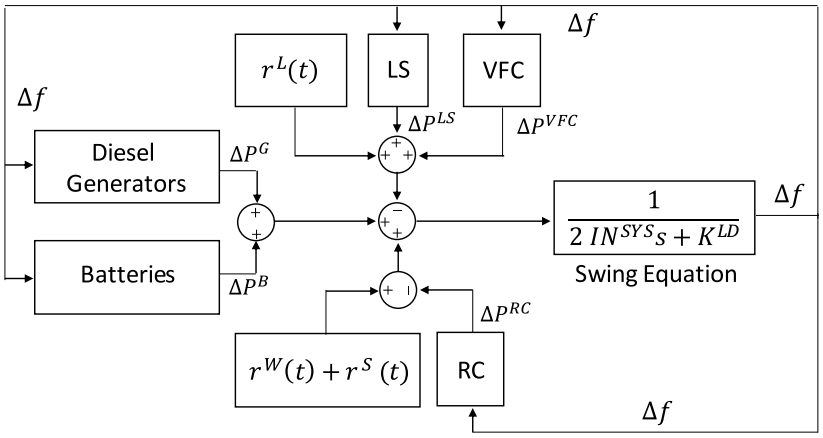

Figure 2.11: Microgrid's frequency regulation model.

2.5 Summary

This chapter presented a background review of the concepts and models used through the present thesis. The review included fundamental aspects related to microgrid operation and control, including its hierarchical control structure and the use of centralized EMS models for an efficient and reliable system operation. Furthermore, existing modeling techniques for representing the flexibility and practical challenges of BESS and aggregated TCL control techniques were discussed. Finally, existing mathematical models for representing the frequency dynamics and control of isolated microgrids were presented, including transient models for diesel generators, batteries, electric loads, and load shedding and renewable curtailment auxiliary controllers.

Chapter 3

Integrating Short-Term Power Fluctuations and Battery Degradation in Microgrid Operation

As discussed in Chapter 1, second-to-second power fluctuations can play a relevant role in the operation and control of isolated microgrids, as these tend to have a low inertia and significant renewable integration. In this context, modern microgrid EMS model need to incorporate short-term power fluctuations within their decision-making process to ensure a reliable and efficient system operation. Furthermore, given the major role that BESS can play to counterbalance power fluctuations, the energy shifting and regulation capability of batteries, as well as the resulting battery degradation costs, need to be integrated within modern EMS models for an enhanced system operation. Hence, a novel EMS embedding short-term fluctuations and battery degradation is developed in this chapter. Bearing in mind that computational tractability is a necessary feature for practical EMS implementations, the models developed here are designed for attaining a suitable computational efficiency, allowing their direct incorporation into the optimization routines of modern EMS models. Exhaustive computational experiments on the real Kasabonika Lake First Nation (KLFN) isolated microgrid and CIGRE benchmark test system show the benefits resulting from the implementation of the proposed EMS model, highlighting the need to integrate short-term fluctuations and battery degradation within modern EMS models for isolated microgrids.

The chapter is organized as follows: In Section 3.1, novel computationally tractable models describing short-term power fluctuations and battery degradation are presented. In

Section 3.2, reserves, their modeling, and how these are affected by short-term fluctuations, are discussed. Based on the models developed in the two previous sections, the proposed practical EMS model is then presented in Section 3.3. Computational experiments and their results are discussed in Section 3.4. Finally, a summary of the topics reviewed in this chapter is presented in Section 3.5.

3.1 Short-Term Fluctuations and Battery Degradation Models

In this section, precise and computationally efficient models to characterize short-term fluctuations and battery degradation are described. These models serve as the basis for deriving the mathematical expressions that make the computationally tractable EMS model proposed in this chapter.

3.1.1 Short-Term Fluctuations Model

One of the main challenges of modeling second-to-second power fluctuations within EMS is computational tractability. As time-variability of renewable generation and demand is usually captured in EMS models by defining different time intervals, directly using a detailed time-resolution in the order of seconds would result on a dramatic increase in the number of decision variables, yielding a computational intractable model. Hence, a computationally efficient representation of short-term fluctuations is developed here, which is based on considering two different time frames: one for dispatch (or long) time intervals $h \in \mathcal{H} = \{1, \ldots, H\}$, and another for intra-dispatch (or short) time intervals $j \in \mathcal{J} = \{1, \ldots, J\}$. This allows splitting the generic instantaneous power vector $\boldsymbol{p}_h$ during dispatch time interval h into long and short term components as follows:

$$\boldsymbol{p}_h = \underbrace{[\hat{p}_h + \chi_h(\xi)]}_{\text{long term}} \mathbf{1} + \underbrace{\boldsymbol{r}_h(\xi)}_{\text{short term}} \tag{3.1}$$

where $\boldsymbol{p}_h = [p_{h,1}, \ldots, p_{h,j}, \ldots, p_{h,J}]$; $\mathbf{1}$ is a vector of ones of dimension J; $\hat{p}_h$ is the average power forecast; and χ_h is the average power forecast error, which is affected by uncertainty ξ. Thus, short-term fluctuations are described by vector $\boldsymbol{r}_h = [r_{h,1}, \ldots, r_{h,j}, \ldots, r_{h,J}]$, which is also affected by uncertainty. Note that $\hat{p}_h$ and χ_h are constant during the dispatch time interval h, and thus have a time resolution of ΔT_h. In contrast, $\boldsymbol{r}_h$ depends also on the short time interval j, and thus has a time step of length $\Delta\tau \ll \Delta T_h$. Figure 3.1 depicts an

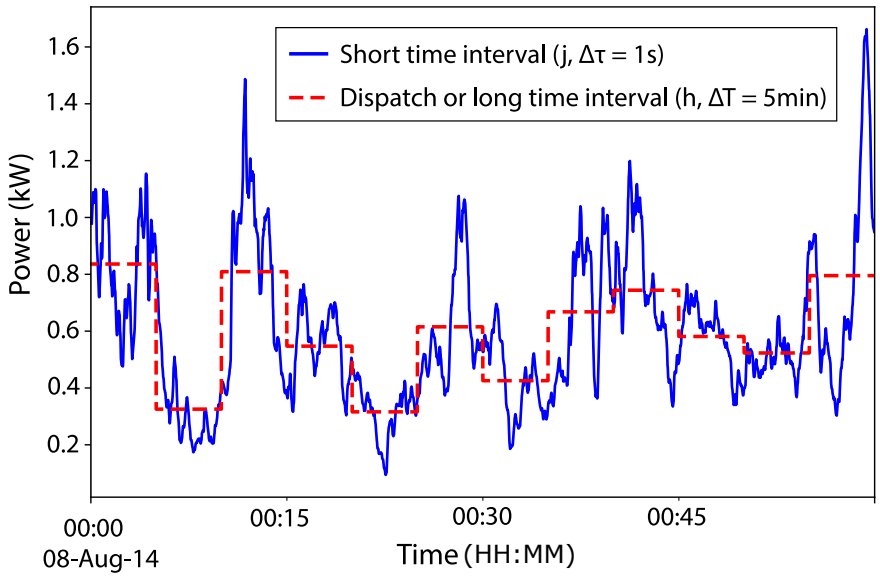

Figure 3.1: Average powers and short-term fluctuations for a 10 kW wind plant at the KLFN microgrid [5].

example in which measurements for the KLFN microgrid [5], with a resolution of $\Delta\tau = 1$s, are used to build: (i) average powers $\hat{p}_h$, which are constant during dispatch time intervals of length $\Delta T_h = 5$min $\forall h \in \mathcal{H}$; and (ii) short-term fluctuations $\boldsymbol{r}_h$, that oscillate around the average powers. In this example, forecast errors are not present, i.e., $\chi_h = 0 \ \forall h \in \mathcal{H}$.

Formulation (3.1) allows the formal definition of a novel computationally efficient representation of the vector of short-term fluctuations $\boldsymbol{r}_h$, referred to as *feature-based representation* here. The key idea is that instead of directly using the high-dimensional vector $\boldsymbol{r}_h$ in the EMS model (as in [34–36]), only the most relevant features of such vector are considered, avoiding the need to define decision variables for each short time interval $j \in \mathcal{J}$, and thus significantly reducing computational burden. Here, the standard deviation (std) and mean absolute deviation (mad) statistical metrics are selected as the features that characterize $\boldsymbol{r}_h$, since these can be linked to reserve sizing and reserve utilization, as described later in Sections 3.2.2 and 3.3.1. Thus, the feature-based representation of $\boldsymbol{r}_h$ is as follows:

$$\boldsymbol{v}_h = \begin{bmatrix} \text{std}(\boldsymbol{r}_h) \\ \text{mad}(\boldsymbol{r}_h) \end{bmatrix} \tag{3.2}$$

where $\boldsymbol{v}_h$ is a vector of dimension equal to 2, which is significantly lower than $J = \dim(\boldsymbol{r}_h)$.

Note that this idea can easily be extended to incorporate other possibly relevant features.

3.1.2 Battery Degradation Model

As discussed in Section 2.2.2, the battery degradation caused by cycle aging can be described by equations (2.6) and (2.7). These equations, while accurate for describing battery aging, have the drawback that they are highly non-linear in practical settings, which prevents their direct integration within operational EMS models. Such non-linearity stems from functions $\boldsymbol{\mathcal{F}}^{ID}(\cdot)$ and $\Gamma^{\lambda}(\cdot)$, being the former non-analytical, and the latter convex but non-linear in practical settings [43]. Thus, to circumvent the above issue, a piecewise linear representation based on [42] is proposed here, for which the battery's cycle depth range is split into even partitions $l \in \mathcal{L}$, resulting in the following expression for describing the degradation of battery $b \in \mathcal{B}$:

$$\mathcal{F}_b^{CYC}(\boldsymbol{c}_b^B, \boldsymbol{d}_b^B) = \frac{\Delta t}{E_b^B} \sum_{t \in \mathcal{T}} \sum_{l \in \mathcal{L}} \frac{\hat{\phi}_{b,l}}{2} \left(\eta_b^{B,C}\, c_{b,l,t}^B + \frac{d_{b,l,t}^B}{\eta_b^{B,D}} \right) \tag{3.3a}$$

$$s_{b,l,t}^B - s_{b,l,t-1}^B = \frac{\Delta t}{E_b^B} \left(\eta_b^{B,C}\, c_{b,l,t}^B - \frac{d_{b,l,t}^B}{\eta_b^{B,D}} \right) \tag{3.3b}$$

$$0 \leq s_{b,l,t}^B \leq \overline{S}_{b,l} \quad \forall b \in \mathcal{B}, l \in \mathcal{L}, t \in \mathcal{T} \tag{3.3c}$$

where $\mathcal{T}$ is a set of generic time intervals t with time-step length Δt; $c_{b,l,t}^B$ is the charging and $d_{b,l,t}^B$ the discharging of battery's b partition l at time t; $E_b^B, \eta_b^{B,C}$, and $\eta_b^{B,D}$ are the battery's rated energy capacity, charging efficiency, and discharging efficiency, respectively; and $\hat{\phi}_{b,l}$ is the piecewise linear degradation coefficient. Note that each battery's b partition l has its own SoC $s_{b,l,t}^B$, which is bounded by the partition's depth range $\overline{S}_{b,l}$. Furthermore, observe in (3.3a) that unlike [42], half-cycles instead of full-cycles are assumed, so that both charging and discharging are equally penalized in terms of the resulting degradation.

3.2 Reserves and Regulation Modeling

Based on (3.1), reserves for managing forecast errors and short-term fluctuations are needed to ensure a secure microgrid operation. Accordingly, in this section, methods for efficiently sizing and allocating these reserves are discussed. Furthermore, tools for assessing the security provided by such reserves are presented.

3.2.1 Forecast Error Reserve

Most EMS models consider reserves to handle forecast errors, which are typically modeled as a percentage of the expected renewable generation and demand (e.g., [22–27]). This same principle is used here to determine the forecast error reserve needs. Thus, from (3.1), one can describe the microgrid's net load forecast error as follows:

$$\chi_h^{MG}(\xi) = \hat{P}_h^L \, \tilde{\chi}_h^L(\xi) - \hat{p}_h^W \, \tilde{\chi}_h^W(\xi) - \hat{p}_h^S \, \tilde{\chi}_h^S(\xi) \tag{3.4}$$

where $\hat{P}_h^L$, $\hat{p}_h^W$, and $\hat{p}_h^S$ are the forecast average powers during dispatch time interval h corresponding to load, wind generation, and solar generation, respectively; and errors associated with each forecast are described by the normalized zero-mean random scalars $\tilde{\chi}_h^L$, $\tilde{\chi}_h^W$, and $\tilde{\chi}_h^S$.

Based on (3.4), and assuming statistical independence, the standard deviation of the microgrid's net load can be computed as follows:

$$\text{std}\left(\chi_h^{MG}\right) = \left[\left(\hat{P}_h^L \tilde{\sigma}_h^{\chi,L}\right)^2 + \left(\hat{p}_h^W \tilde{\sigma}_h^{\chi,W}\right)^2 + \left(\hat{p}_h^S \tilde{\sigma}_h^{\chi,S}\right)^2\right]^{1/2} \tag{3.5}$$

where $\tilde{\sigma}_h^{\chi,L} = \text{std}\left(\tilde{\chi}_h^L\right)$, $\tilde{\sigma}_h^{\chi,W} = \text{std}\left(\tilde{\chi}_h^W\right)$, and $\tilde{\sigma}_h^{\chi,S} = \text{std}\left(\tilde{\chi}_h^S\right)$ can be estimated from normalized historical samples of forecast errors $\chi_h^L/\hat{P}_h^L$, $\chi_h^W/\hat{p}_h^W$, and $\chi_h^S/\hat{p}_h^S$, respectively. Hence, the forecast error reserve requirement is given by:

$$\zeta_h^{\chi} = \epsilon^{\chi} \, \text{std}\left(\chi_h^{MG}\right) \tag{3.6}$$

where the confidence level can be adjusted through the parameter ϵ^{χ}.

3.2.2 Regulation Reserve

Conventional EMS models do not explicitly represent short-term fluctuations, nor explicitly consider these when computing total reserve requirements (e.g., [22–27]). However, as discussed in Chapter 1, properly accounting for short-term fluctuations is important in isolated microgrids with low inertia and significant renewable integration. Thus, unlike previous EMS models, an especially-dedicated regulation reserve is considered here, which aims to handle the regulation signal stemming from fast fluctuations of demand and renewable generation. Hence, from (3.1), such regulation signal can be defined as follows:

$$\boldsymbol{r}_h^{MG}(\xi) = \hat{P}_h^L \, \tilde{\boldsymbol{r}}_h^L(\xi) - \hat{p}_h^W \, \tilde{\boldsymbol{r}}_h^W(\xi) - \hat{p}_h^S \, \tilde{\boldsymbol{r}}_h^S(\xi) \tag{3.7}$$

where $\tilde{\boldsymbol{r}}_h^L$, $\tilde{\boldsymbol{r}}_h^W$, and $\tilde{\boldsymbol{r}}_h^S$ are zero-mean random vectors representing the normalized short-term fluctuations stemming from demand, wind generation, and solar generation, respectively.

Based on (3.7), and following a similar procedure as in Section 3.2.1, the standard deviation of the regulation signal can be computed as:

$$\text{std}\left(\boldsymbol{r}_h^{MG}\right) = \left[\left(\hat{P}_h^L \tilde{\sigma}_h^{r,L}\right)^2 + \left(\hat{p}_h^W \tilde{\sigma}_h^{r,W}\right)^2 + \left(\hat{p}_h^S \tilde{\sigma}_h^{r,S}\right)^2\right]^{1/2} \tag{3.8}$$

where $\tilde{\sigma}_h^{r,L} = \text{std}\left(\tilde{\boldsymbol{r}}_h^L\right)$, $\tilde{\sigma}_h^{r,W} = \text{std}\left(\tilde{\boldsymbol{r}}_h^W\right)$, and $\tilde{\sigma}_h^{r,S} = \text{std}\left(\tilde{\boldsymbol{r}}_h^S\right)$. However, note that in this case, standard deviations are computed by concatenating normalized historical samples of $r_{j,h}^L/\hat{P}_h^L$, $r_{j,h}^W/\hat{p}_h^W$, and $r_{j,h}^S/\hat{p}_h^S$, since $\tilde{\boldsymbol{r}}$ is a random vector of dimension J. Furthermore, notice that standard deviations only depend on dispatch time interval $h \in \mathcal{H}$, as the short time interval index $j \in \mathcal{J}$ is avoided in accordance with the feature-based approach (3.2).

From (3.8), the regulation reserve requirement can directly be defined, as follows:

$$\zeta_h^r = \epsilon^r \,\text{std}\left(\boldsymbol{r}_h^{MG}\right) \tag{3.9}$$

where the confidence level can be adjusted through the parameter ϵ^r.

3.2.3 Reserve Allocation

The reserves previously defined in Sections 3.2.1 and 3.2.2 require the definition of their corresponding upward and downward reserve constraints to ensure enough capacity margins are kept. Assuming that reserves can be provided by thermal generators $g \in \mathcal{G}$ and batteries $b \in \mathcal{B}$, the following forecast error χ reserve constraints can be obtained $\forall h \in \mathcal{H}$:

$$\zeta_h^\chi = \sum_{g\in\mathcal{G}} \Delta p_{g,h}^{G,\chi,\uparrow} + \sum_{b\in\mathcal{B}}\sum_{l\in\mathcal{L}} \Delta p_{b,l,h}^{B,D,\chi,\uparrow} \tag{3.10a}$$

$$\zeta_h^\chi = \sum_{g\in\mathcal{G}} \Delta p_{g,h}^{G,\chi,\downarrow} + \sum_{b\in\mathcal{B}}\sum_{l\in\mathcal{L}} \Delta p_{b,l,h}^{B,C,\chi,\downarrow} \tag{3.10b}$$

where $\Delta p_{g,h}^{G,\chi,\uparrow}$ and $\Delta p_{g,h}^{G,\chi,\downarrow}$ are the upward ($\uparrow$) and downward ($\downarrow$) forecast error reserve provided by generator g, respectively; $\Delta p_{b,l,h}^{B,D,\chi,\uparrow}$ is the upward forecast error reserve provided by increasing the discharging power of battery's b partition l; and $p_{b,l,h}^{B,C,\chi,\downarrow}$ is the downward forecast error reserve provided by increasing the charging power of battery's b partition l. Note that a symmetrical upward/downward reserve requirement ζ_h^χ is considered here.

The regulation r reserve constraints can be defined similarly as follows $\forall h \in \mathcal{H}$:

$$\zeta_h^r = \sum_{g\in\mathcal{G}} \Delta p_{g,h}^{G,r,\uparrow} + \sum_{b\in\mathcal{B}}\sum_{l\in\mathcal{L}} \Delta p_{b,l,h}^{B,D,r,\uparrow} \tag{3.11a}$$

$$\zeta_h^r = \sum_{g\in\mathcal{G}} \Delta p_{g,h}^{G,r,\downarrow} + \sum_{b\in\mathcal{B}}\sum_{l\in\mathcal{L}} \Delta p_{b,l,h}^{B,C,r,\downarrow} \tag{3.11b}$$

where $\Delta p_{g,h}^{G,r,\uparrow}$ and $\Delta p_{g,h}^{G,r,\downarrow}$ are the upward and downward regulation reserve provided by generator g, respectively; and $\Delta p_{b,l,h}^{B,D,r,\uparrow}$ and $\Delta p_{b,l,h}^{B,C,r,\downarrow}$ are the upward and downward regulation reserve provided by battery's b partition l, respectively. Note that a symmetrical upward/downward reserve requirement ζ_h^r is also considered here.

The reserve allocation defined by variables $\Delta\boldsymbol{p}$ indicate how the mismatches caused by forecast errors and short-term fluctuations are shared among generators and batteries. Specifically, power sharing is dictated by the participation factors $\boldsymbol{\alpha}$, defined as follows:

$$\alpha_{g,h}^{G,\chi,\uparrow} = \frac{\Delta p_{g,h}^{G,\chi,\uparrow}}{\zeta_h^\chi}, \quad \alpha_{g,h}^{G,\chi,\downarrow} = \frac{\Delta p_{g,h}^{G,\chi,\downarrow}}{\zeta_h^\chi} \tag{3.12a}$$

$$\alpha_{g,h}^{G,r,\uparrow} = \frac{\Delta p_{g,h}^{G,r,\uparrow}}{\zeta_h^r}, \quad \alpha_{g,h}^{G,r,\downarrow} = \frac{\Delta p_{g,h}^{G,r,\downarrow}}{\zeta_h^r} \tag{3.12b}$$

$$\alpha_{b,h}^{B,\chi,\uparrow} = \frac{\sum_{l\in\mathcal{L}} \Delta p_{b,l,h}^{B,D,\chi,\uparrow}}{\zeta_h^\chi}, \quad \alpha_{b,h}^{B,\chi,\downarrow} = \frac{\sum_{l\in\mathcal{L}} \Delta p_{b,l,h}^{B,C,\chi,\downarrow}}{\zeta_h^\chi} \tag{3.12c}$$

$$\alpha_{b,h}^{B,r,\uparrow} = \frac{\sum_{l\in\mathcal{L}} \Delta p_{b,l,h}^{B,D,r,\uparrow}}{\zeta_h^r}, \quad \alpha_{b,h}^{B,r,\downarrow} = \frac{\sum_{l\in\mathcal{L}} \Delta p_{b,l,h}^{B,C,r,\downarrow}}{\zeta_h^r} \tag{3.12d}$$

Thus, the participation factors are determined by the share of the total reserve that is provided by each generator and battery, analogous to the participation factors in an AGC scheme [85]. From (3.1) and (3.12), the reference instantaneous power provided to generator g can then be defined as:

$$\boldsymbol{p}_{g,h}^G = \left[\hat{p}_{g,h}^G + \alpha_{g,h}^{G,\chi,\uparrow}\,\chi_h^{MG+}(\xi) - \alpha_{g,h}^{G,\chi,\downarrow}\,\chi_h^{MG-}(\xi)\right]\mathbf{1} + \alpha_{g,h}^{G,r,\uparrow}\,\boldsymbol{r}_h^{MG+}(\xi) - \alpha_{g,h}^{G,r,\downarrow}\,\boldsymbol{r}_h^{MG-}(\xi) \tag{3.13}$$

where $\hat{p}_{g,h}^G$ denotes the generation set-point or average power of generator g during dispatch time interval h; and positive and negative parts are described by $\chi_h^{MG+} = \max\{\chi_h^{MG}, 0\}$; $\chi_h^{MG-} = \max\{-\chi_h^{MG}, 0\}$, which also applies for $\boldsymbol{r}^{MG+}$ and $\boldsymbol{r}^{MG-}$. Similarly, the reference instantaneous power provided to battery b can be described by:

$$\boldsymbol{p}_{b,h}^B = \left[\hat{p}_{b,h}^B + \alpha_{b,h}^{B,\chi,\uparrow}\,\chi_h^{MG+}(\xi) - \alpha_{b,h}^{B,\chi,\downarrow}\,\chi_h^{MG-}(\xi)\right]\mathbf{1} + \alpha_{b,h}^{B,r,\uparrow}\,\boldsymbol{r}_h^{MG+}(\xi) - \alpha_{b,h}^{B,r,\downarrow}\,\boldsymbol{r}_h^{MG-}(\xi) \tag{3.14}$$

where the battery set-point $\hat{p}^B_{b,h}$ is given by $\hat{p}^B_{b,h} = \sum_{l\in\mathcal{L}}(d^B_{b,l,h} - c^B_{b,l,h})$. It is important to highlight that (3.13) and (3.14) might violate the capacity limits of generators and batteries in the presence of unexpectedly large power fluctuations, as discussed next.

3.2.4 Reserve Security Assessment

The reference instantaneous powers provided to generators $\boldsymbol{p}^G_{g,h}$ in (3.13) and batteries $\boldsymbol{p}^B_{b,h}$ in (3.14) are computed based on estimated reserve needs, which might not be sufficient in the event of unexpectedly large short-term power variations. As discussed in Chapter 1, this is especially relevant for isolated microgrids, since it would lead to generators and batteries rapidly hitting their capacity limits, affecting the overall system regulation performance. Based on this observation, a differentiation is made between: (i) reference instantaneous powers $\boldsymbol{p}^G_{g,h}$ and $\boldsymbol{p}^B_{b,h}$, which might violate power and energy capacity limits; and (ii) effectively delivered instantaneous powers $\boldsymbol{p'}^G_{g,h}$ and $\boldsymbol{p'}^B_{b,h}$, which enforce such capacity limits.

The aforementioned definitions allow the design of a security assessment metric to quantify the regulation performance of a particular reserve sizing and allocation method, which is referred here as Limit-Hit Probability (LHP), and is defined as follows:

$$\text{LHP} = \text{Prob}\left[\left(\exists\, g : \boldsymbol{p}^G_{g,h} \neq \boldsymbol{p'}^G_{g,h}\right) \cup \left(\exists\, b : \boldsymbol{p}^B_{b,h} \neq \boldsymbol{p'}^B_{b,h}\right)\right] \tag{3.15}$$

This metric measures the frequency (or probability) that the capacity limits of the DER units are reached due to insufficient reserve allocation, leading to differences between reference and delivered instantaneous powers and thus inadequate tracking of the regulation signal.

3.3 Energy Management System Model

In this section, the definitions and expressions previously derived in Sections 3.1 and 3.2 are used to design a computationally tractable EMS model that incorporates short-term fluctuations and battery degradation.

3.3.1 Operational Impact of Reserve Provision

Typical EMS models assume that the impact of reserve provision is limited to narrowing the range of feasible average power set-points (e.g., see [22–27]). For generators, this can

be modeled using the following constraints:

$$\hat{p}^G_{g,h} + \Delta p^{G,\chi,\uparrow}_{g,h} + \Delta p^{G,r,\uparrow}_{g,h} \leq \overline{P}^G_g \, u^G_{g,h} \quad \forall g \in \mathcal{G}, h \in \mathcal{H} \tag{3.16a}$$

$$\hat{p}^G_{g,h} - \Delta p^{G,\chi,\downarrow}_{g,h} - \Delta p^{G,r,\downarrow}_{g,h} \geq \underline{P}^G_g \, u^G_{g,h} \quad \forall g \in \mathcal{G}, h \in \mathcal{H} \tag{3.16b}$$

where $\overline{P}^G_g$ and $\underline{P}^G_g$ are generator g's steady-state maximum and minimum power; and $u^G_{g,h}$ is a binary variable indicating the generator's ON/OFF status. Similarly, for batteries, the following constraints can be defined:

$$\sum_{l \in \mathcal{L}} \left(c^B_{b,l,h} + \Delta p^{B,C,\chi,\downarrow}_{b,l,h} + \Delta p^{B,C,r,\downarrow}_{b,l,h} \right) \leq \overline{P}^B_b \quad \forall b \in \mathcal{B}, h \in \mathcal{H} \tag{3.17a}$$

$$\sum_{l \in \mathcal{L}} \left(d^B_{b,l,h} + \Delta p^{B,D,\chi,\uparrow}_{b,l,h} + \Delta p^{B,D,r,\uparrow}_{b,l,h} \right) \leq \overline{P}^B_b \quad \forall b \in \mathcal{B}, h \in \mathcal{H} \tag{3.17b}$$

where $\overline{P}^B_b$ is the battery b's maximum charging/discharging power. Furthermore, based on (3.3), constraints to ensure enough energy is saved for battery reserve provision, assuming the worst-case scenario of energy requirement for the following dispatch time interval, can be defined as follows $\forall b \in \mathcal{B}, l \in \mathcal{L}, h \in \mathcal{H}$:

$$s^B_{b,l,h-1} + \frac{\Delta T_h \, \eta^{B,C}_b}{E^B_b} \left(c^B_{b,l,h} + \Delta p^{B,C,\chi,\downarrow}_{b,l,h} + \Delta p^{B,C,r,\downarrow}_{b,l,h} \right) - \frac{\Delta T_h}{E^B_b \, \eta^{B,D}_b} \, d^B_{b,l,h} \leq \overline{S}_{b,l} \tag{3.18a}$$

$$s^B_{b,l,h-1} - \frac{\Delta T_h}{E^B_b \, \eta^{B,D}_b} \left(d^B_{b,l,h} + \Delta p^{B,D,\chi,\uparrow}_{b,l,h} + \Delta p^{B,D,r,\uparrow}_{b,l,h} \right) + \frac{\Delta T_h \, \eta^{B,C}_b}{E^B_b} \, c^B_{b,l,h} \geq 0 \tag{3.18b}$$

In addition to the aforementioned constraints, reserves have additional impacts on operation in practice. As discussed in Section 3.2.3, reserves also dictate how real-time mismatches are shared among generators and batteries, and thus have an impact on their instantaneous power outputs. Thus, and unlike previous EMS models, the modeling is here extended to also include this effect, which in turn influences the expected average thermal generation, battery SoC, and battery degradation, as described next.

First, based on the feature-based representation (3.2), the novel concept of Expected Reserve Utilization (ERU) is introduced, which quantifies how much of the allocated reserve is expected to be deployed on average. This metric is especially relevant for forecast error reserves and regulation reserves, which, unlike contingency reserves, are continuously being deployed to handle real-time mismatches. Here, the ERU of forecast error and regulation reserves is estimated by computing the ratio between the mean absolute deviation (mad)

and total reserve requirements ζ, as follows:

$$\varphi_h^{\chi} = \min\left\{1, \frac{\text{mad}(\chi_h^{MG})}{\zeta_h^{\chi}}\right\} = \min\left\{1, \frac{\mathcal{G}^{\mathcal{K}}(\chi_h^{MG})}{\epsilon^{\chi}}\right\} \tag{3.19a}$$

$$\varphi_h^{r} = \min\left\{1, \frac{\text{mad}(\boldsymbol{r}_h^{MG})}{\zeta_h^{r}}\right\} = \min\left\{1, \frac{\mathcal{G}^{\mathcal{K}}(\boldsymbol{r}_h^{MG})}{\epsilon^{r}}\right\} \tag{3.19b}$$

where $\mathcal{G}^{\mathcal{K}}(\cdot) = \text{mad}(\cdot)/\text{std}(\cdot)$ is Geary's kurtosis [88]. Note, however, that other methods for estimating the ERU can also be used.

For thermal generators, the ERU allows modeling the change in the expected average power of generator g during dispatch time interval h due to reserve provision, as follows:

$$\Delta e_{g,h}^{G} = \frac{\varphi_h^{\chi}}{2}\left(\Delta p_{g,h}^{G,\chi,\uparrow} - \Delta p_{g,h}^{G,\chi,\downarrow}\right) + \varphi_h^{r}\left(\Delta p_{g,h}^{G,r,\uparrow} - \Delta p_{g,h}^{G,r,\downarrow}\right) \tag{3.20}$$

Observe that φ_h^{χ} is multiplied by $1/2$, which results from considering two mutually exclusive outcomes (either upward or downward forecast error reserve deployment) with an equal probability of $1/2$. This is not the case for φ_h^{r}, as it is assumed that both upward and downward regulation reserves will always be deployed for at least for a couple of seconds during each dispatch time interval h, resulting in both upward and downward regulation reserve deployment events having a probability of 1.

For batteries, ERU can be used to describe the change in the expected SoC of battery's b partition l due to reserve provision, as follows:

$$\Delta s_{b,l,h}^{B} = \frac{\varphi_h^{\chi}}{2}\frac{\Delta T_h}{E_b^{B}}\left(\eta_b^{B,C}\,\Delta p_{b,l,h}^{B,C,\chi,\downarrow} - \frac{\Delta p_{b,l,h}^{B,D,\chi,\uparrow}}{\eta_b^{B,D}}\right) + \varphi^{r}\frac{\Delta T_h}{E_b^{B}}\left(\eta_b^{B,C}\,\Delta p_{b,l,h}^{B,C,r,\downarrow} - \frac{\Delta p_{b,l,h}^{B,D,r,\uparrow}}{\eta_b^{B,D}}\right) \tag{3.21}$$

Thus, the expected SoC at the end of dispatch time interval h, resulting from both energy shifting and reserve provision can be described as follows:

$$s_{b,l,h}^{B} - s_{b,l,h-1}^{B} = \frac{\Delta T_h}{E_b^{B}}\left(\eta_b^{B,C}\,c_{b,l,h}^{B} - \frac{d_{b,l,h}^{B}}{\eta_b^{B,D}}\right) + \Delta s_{b,l,h}^{B} \tag{3.22a}$$

$$0 \leq s_{b,l,h}^{B} \leq \overline{S}_{b,l} \quad \forall b \in \mathcal{B}, l \in \mathcal{L}, h \in \mathcal{H} \tag{3.22b}$$

The ERU also allows to describe the expected increase in battery degradation due to reserve

provision as follows:

$$\Delta\phi_{b,l,h} = \frac{\hat{\phi}_{b,l}}{2}\frac{\varphi_h^{\chi}}{2}\frac{\Delta T_h}{E_b^B}\left(\eta_b^{B,C}\,\Delta p_{b,l,h}^{B,C,\chi,\downarrow} + \frac{\Delta p_{b,l,h}^{B,D,\chi,\uparrow}}{\eta_b^{B,D}}\right) + \frac{\hat{\phi}_{b,l}}{2}\varphi^r\frac{\Delta T_h}{E_b^B}\left(\eta_b^{B,C}\,\Delta p_{b,l,h}^{B,C,r,\downarrow} + \frac{\Delta p_{b,l,h}^{B,D,r,\uparrow}}{\eta_b^{B,D}}\right) \quad (3.23)$$

where this equation is based on the piecewise degradation model (3.3). Thus, the expected total battery degradation resulting from energy shifting and reserve provision is:

$$\Phi_{b,l,h} = \frac{\hat{\phi}_{b,l}}{2}\frac{\Delta T_h}{E_b^B}\left(\eta_b^{B,C}\,c_{b,l,h}^B + \frac{d_{b,l,h}^B}{\eta_b^{B,D}}\right) + \Delta\phi_{b,l,h} \quad (3.24)$$

3.3.2 Renewable Curtailment

Another relevant feature commonly neglected in EMS models is the use of renewable curtailment for short-term fluctuation management (e.g., [22–27]). Since short-term fluctuations are mainly a byproduct of non-dispatchable renewable generation, renewable curtailment can be used to reduce such fluctuations and thus reserve needs. To model this phenomenon, the high correlation in the resource availability of the microgrid's renewable plants is exploited, which stems from the geographical proximity of the microgrid's units. Thus, wind and solar generation can be lumped into one equivalent renewable plant for each, yielding the following equations for the total wind and solar forecast average powers $\hat{p}_h^W$ and $\hat{p}_h^S$:

$$\hat{p}_h^W \le \overline{P}_h^W, \quad \hat{p}_h^S \le \overline{P}_h^S \quad \forall h \in \mathcal{H} \quad (3.25)$$

where $\overline{P}_h^W$ and $\overline{P}_h^S$ are the maximum available wind and solar average powers during dispatch time interval h, respectively.

Equation (3.25) not only impacts the average power injected by renewable sources, but also the microgrid's net load forecast error χ_h^{MG} in (3.4)-(3.6) and regulation signal $\boldsymbol{r}_h^{MG}$ in (3.7)-(3.9). Accordingly, the forecast error and regulation reserve needs ζ_h^{χ} and ζ_h^r are also a function of wind and solar forecast average powers $(\hat{p}_h^W, \hat{p}_h^S)$, as follows:

$$\zeta_h^{\chi} = \epsilon^{\chi}\left[\left(\hat{P}_h^L\tilde{\sigma}_h^{\chi,L}\right)^2 + \left(\hat{p}_h^W\tilde{\sigma}_h^{\chi,W}\right)^2 + \left(\hat{p}_h^S\tilde{\sigma}_h^{\chi,S}\right)^2\right]^{1/2} \quad (3.26a)$$

$$\zeta_h^{r} = \epsilon^{r}\left[\left(\hat{P}_h^L\tilde{\sigma}_h^{r,L}\right)^2 + \left(\hat{p}_h^W\tilde{\sigma}_h^{r,W}\right)^2 + \left(\hat{p}_h^S\tilde{\sigma}_h^{r,S}\right)^2\right]^{1/2} \quad (3.26b)$$

which captures the capability of using renewable curtailment to reduce the overall system reserve needs. Equations (3.26a) and (3.26b) are non-convex in $(\hat{p}_h^W, \hat{p}_h^S)$, and thus computationally inefficient. To obtain an efficient convex formulation, the fact that $\hat{P}_h^L \tilde{\sigma}_h^{\chi/r,L}$ is large in practical settings is exploited, which allows replacing the non-convex square root function by a linear interpolation between points $(0,0)$ and $(\overline{P}_h^W, \overline{P}_h^S)$. Thus, a set of supporting hyperplanes can be used to represent reserve needs ζ_h^χ and ζ_h^r, which can be iteratively updated through a cutting-planes algorithm [89].

It is also important to highlight that due to the dependence of reserve needs ζ_h^χ and ζ_h^r on $(\hat{p}_h^W, \hat{p}_h^S)$, the ERUs in (3.19) are also affected by $(\hat{p}_h^W, \hat{p}_h^S)$. To avoid overcomplicating the model and keep computational tractability, it is assumed that both χ_h^{MG} and $\boldsymbol{r}_h^{MG}$ resemble a normal distribution, and thus $\mathcal{G}^{\mathcal{K}}(\cdot) = \sqrt{2/\pi} \approx 0.8$ regardless of the values of $(\hat{p}_h^W, \hat{p}_h^S)$, eliminating the dependence of the ERUs on the deployed capacities.

3.3.3 Frequency Control Mechanism

As discussed in Section 3.1.1, short-term fluctuations describe power oscillations in the order of seconds. Under this time frame, the microgrid's frequency control mechanism might impose limitations on the way power mismatches are shared, making its modeling relevant. Typically, microgrids have a droop control which may or may not be accompanied by a supplementary control for frequency recovery [10], similar to AGC. In the case of a droop-only control, the short-term fluctuations will be shared among generators and batteries according to their droop κ, requiring the addition of power sharing constraints $\forall h \in \mathcal{H}$, as follows [25]:

$$\frac{\kappa_b^B}{\overline{P}_b^B} \sum_{l \in \mathcal{L}} \Delta p_{b,l,h}^{B,D,r,\uparrow} = \frac{\kappa_{b'}^B}{\overline{P}_{b'}^B} \sum_{l \in \mathcal{L}} \Delta p_{b',l,h}^{B,D,r,\uparrow} \quad \forall (b,b') \in \mathcal{B} \times \mathcal{B} \tag{3.27a}$$

$$\frac{\kappa_b^B}{\overline{P}_b^B} \sum_{l \in \mathcal{L}} \Delta p_{b,l,h}^{B,C,r,\downarrow} = \frac{\kappa_{b'}^B}{\overline{P}_{b'}^B} \sum_{l \in \mathcal{L}} \Delta p_{b',l,h}^{B,C,r,\downarrow} \quad \forall (b,b') \in \mathcal{B} \times \mathcal{B} \tag{3.27b}$$

$$\frac{\kappa_b^B}{\overline{P}_b^B} \varsigma_{b,g,h}^{B,\uparrow} = \frac{\kappa_g^G}{\overline{P}_g^G} \Delta p_{g,h}^{G,r,\uparrow} \quad \forall (b,g) \in \mathcal{B} \times \mathcal{G} \tag{3.27c}$$

$$\frac{\kappa_b^B}{\overline{P}_b^B} \varsigma_{b,g,h}^{B,\downarrow} = \frac{\kappa_g^G}{\overline{P}_g^G} \Delta p_{g,h}^{G,r,\downarrow} \quad \forall (b,g) \in \mathcal{B} \times \mathcal{G} \tag{3.27d}$$

$$\frac{\kappa_g^G}{\overline{P}_g^G} \varsigma_{g',g,h}^{G,\uparrow} = \frac{\kappa_{g'}^G}{\overline{P}_{g'}^G} \varsigma_{g,g',h}^{G,\uparrow} \quad \forall (g,g') \in \mathcal{G} \times \mathcal{G} \tag{3.27e}$$

$$\frac{\kappa^G_g}{\overline{P}^G_g}\,\varsigma^{G,\downarrow}_{g',g,h} = \frac{\kappa^G_{g'}}{\overline{P}^G_{g'}}\,\varsigma^{G,\downarrow}_{g,g',h} \quad \forall (g,g') \in \mathcal{G}\times\mathcal{G} \tag{3.27f}$$

$$\varsigma^{B,\uparrow}_{b,g,h} = u_{g,h}\sum_{l\in\mathcal{L}} \Delta p^{B,D,r,\uparrow}_{b,l,h}, \quad \varsigma^{B,\downarrow}_{b,g,h} = u_{g,h}\sum_{l\in\mathcal{L}} \Delta p^{B,C,r,\downarrow}_{b,l,h} \tag{3.27g}$$

$$\varsigma^{G,\uparrow}_{g,g',h} = u_{g,h}\,\Delta p^{G,r,\uparrow}_{g',h}, \quad \varsigma^{G,\downarrow}_{g,g',h} = u_{g,h}\,\Delta p^{G,r,\downarrow}_{g',h} \tag{3.27h}$$

which stem from the droop equation (2.15) described in Section 2.4, and result in additional limitations on how regulation reserves Δp^r are distributed among generators and batteries. Note that auxiliary variables representing bilinear terms $\varsigma^{B,\uparrow/\downarrow}_{b,g,h}$ and $\varsigma^{G,\uparrow/\downarrow}_{g',g,h}$ are used here, so that the corresponding constraints can be linearized using standard integer optimization techniques [90].

Unlike the droop-only case, if a microgrid has a supplementary control like AGC, short-term fluctuations in the order of seconds are handled by such supplementary control and power sharing is no longer constrained. Thus, in this case constraints (3.27) are not needed.

3.3.4 Other Constraints

The remaining constraints for the proposed EMS model are presented here. Similar equations can already be found in the existing EMS literature (e.g., [22–27]). Thus, the power balance is described as follows:

$$\sum_{b\in\mathcal{B}}\sum_{l\in\mathcal{L}}\left(d^B_{b,l,h} - c^B_{b,l,h}\right) + \sum_{g\in\mathcal{G}} \hat{p}^G_{g,h} = \hat{P}^L_h - \hat{p}^W_h - \hat{p}^S_h - ls_h \quad \forall h \in \mathcal{H} \tag{3.28}$$

where the wind and solar average generation comes from (3.25), and ls_h indicates average load shedding during dispatch time interval h.

The logic of commitment variables, and the minimum up/down constraints on thermal generators are described by the following equations $\forall g \in \mathcal{G}, h \in \mathcal{H}$:

$$u^G_{g,h} - u^G_{g,h-1} = v^G_{g,h} - w^G_{g,h} \tag{3.29a}$$

$$\sum_{\nu=h-MN^{DN}_g}^{h-1} \left(1 - u^G_{g,\nu}\right)\Delta T_\nu \geq MN^{DN}_g\, v^G_{g,h} \tag{3.29b}$$

$$\sum_{m=h-MN^{UP}_g}^{h-1} u^G_{g,m}\,\Delta T_m \geq MN^{UP}_g\, w^G_{g,h} \tag{3.29c}$$

where $v^G_{g,h}$ and $w^G_{g,h}$ indicate the start-up/shut-down of generators, and MN^{UP}_g and MN^{DN}_g are the minimum up/down times.

Additionally, thermal generator ramp constraints are also considered, which can be defined as follows $\forall g \in \mathcal{G}, h \in \mathcal{H}$:

$$-RP^G_g\,\Delta T_h - \overline{P}^G_g\,w^G_{g,h} \leq \hat{p}^G_{g,h} - \hat{p}^G_{g,h-1} \leq RP^G_g\,\Delta T_h + \overline{P}^G_g\,v^G_{g,h} \tag{3.30}$$

where RP^G_g is the thermal generator's ramp limit.

Finally, an energy neutrality constraint is included to prevent significant deviations from the initial battery SoC:

$$s^B_{b,l,H} = S^0_{b,l} \quad \forall b \in \mathcal{B}, l \in \mathcal{L} \tag{3.31}$$

where $S^0_{b,l}$ is the initial battery SoC, and H is the last time index of the set of dispatch time intervals $\mathcal{H} = \{1, \ldots, H\}$.

3.3.5 Optimization Model and Architecture

Based on the equations described in the previous sections, a novel EMS model with regulation, battery degradation, renewable curtailment, and power sharing limitations can be formulated. Thus, the EMS objective function $\mathcal{F}^{OBJ}(\cdot)$ is composed of a degradation component $\Phi \in [0, 1]$, variable generation costs C^G, no-load costs C^{NL}, start-up costs C^{SU}, shut-down costs C^{SD}, and load shedding costs C^{LS}, as follows:

$$\begin{aligned}\mathcal{F}^{OBJ}(\boldsymbol{x}, \boldsymbol{y}) = &\sum_{h\in\mathcal{H}}\sum_{b\in\mathcal{B}}\sum_{l\in\mathcal{L}} E^B_b \cdot C^{RB}_b \cdot \Phi_{b,l,h} + \sum_{h\in\mathcal{H}}\sum_{g\in\mathcal{G}} C^G_g \Delta T_h \left(\hat{p}^G_{g,h} + \Delta e^G_{g,h}\right) \\ &+ \sum_{h\in\mathcal{H}}\sum_{g\in\mathcal{G}} \left(C^{NL}_g \Delta T_h\, u^G_{g,h} + C^{SU}_g\, v^G_{g,h} + C^{SD}_g\, w^G_{g,h}\right) + \sum_{h\in H} C^{LS} \Delta T_h\, ls_h\end{aligned}$$

where E^B_b is battery's b rated energy capacity; C^{BR}_b is the battery replacement cost; $\boldsymbol{x} = \left[\boldsymbol{u}^G, \boldsymbol{v}^G, \boldsymbol{w}^G\right]$ are the binary decision variables; and $\boldsymbol{y} = \left[\hat{\boldsymbol{p}}^G, \hat{\boldsymbol{p}}^W, \hat{\boldsymbol{p}}^S, \Delta\boldsymbol{p}^G, \Delta\boldsymbol{p}^B, \boldsymbol{s}^B, \boldsymbol{c}^B, \boldsymbol{d}^B, \boldsymbol{ls}, \boldsymbol{\zeta}, \boldsymbol{\varsigma}\right]$ are the continuous decisions variables. This results in the following complete EMS

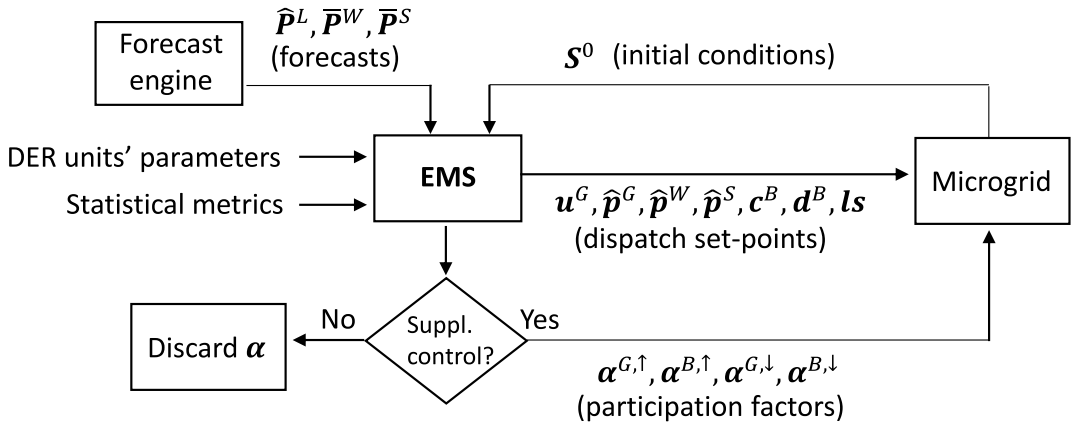

Figure 3.2: Proposed EMS architecture.

model:

$$
\begin{aligned}
\min_{\boldsymbol{x},\boldsymbol{y}} \quad & \mathcal{F}^{OBJ}(\boldsymbol{x},\boldsymbol{y}) \\
\text{s.t.} \quad & \boldsymbol{x} \in \{0,1\}, \ \boldsymbol{y} \geq 0 \\
& \text{Reserves and power balance: (3.10), (3.11), (3.25), (3.26), (3.28)} \\
& \text{Thermal generators: (3.16), (3.20), (3.29), (3.30)} \\
& \text{Batteries and degradation: (3.17), (3.18), (3.21)–(3.24), (3.31)} \\
& \text{Power sharing: (3.27) if droop-only control}
\end{aligned}
$$

which is a MILP problem that can be solved by off-the-shelf solvers. Note that this optimization problem does not include short-time intervals $j \in \mathcal{J}$ (1s timescale), considering only parameters, variables and constraints associated with long-time intervals $h \in \mathcal{H}$ (5min timescale). This results in a low-dimensional, and thus computationally efficient, formulation for the EMS optimization problem.

The general architecture of the proposed EMS is described in Fig. 3.2, which is based on a MPC scheme, as in [22–27]. Under this scheme, optimal dispatch set-points for the first dispatch time interval of each MPC iteration are regularly re-calculated and broadcasted to the microgrid's controllers based on frequently updated forecasts. Note that in the proposed EMS, participation factors $\boldsymbol{\alpha}$ are computed only if an AGC-like supplementary control is available, as these are not relevant in the case of droop-only control.

3.4 Computational Experiments

In this section, computational simulations to evaluate the performance of the proposed EMS model are presented. First, the general settings of the simulations are presented in Section 3.4.1. Then, the procedure used to calibrate reserve parameters are presented in Section 3.4.2. Finally, specific settings, results and discussions, for each of the two evaluated test systems are presented in Sections 3.4.3 and 3.4.4.

3.4.1 General Settings

The performance of the proposed EMS is evaluated by simulating its implementation during one full day on the following two test systems [27]: (i) a real isolated microgrid located in KLFN Ontario-Canada, and (ii) a larger test system based on a CIGRE medium voltage benchmark system. As in [22–27], simulations are performed considering a MPC scheme for which average power forecasts and optimal dispatch set-points are updated every 5 min, resulting in negligible average power forecast errors for the first dispatch time interval of each MPC iteration, i.e., $\chi_1^{MG}(\xi) \approx 0$. In each MPC run, a 24h horizon is used, alongside a variable time-resolution with different time-steps ΔT_h: 6 time-steps of 5min, 6 time-steps of 15min, 6 time-steps of 30min, and 19 time steps of 1h. Reserve requirements are only considered for the first 18 dispatch time intervals, i.e., next 5h, as it was observed that enforcing such constraints for the whole 24h horizon resulted in a large computational burden without significantly improving overall operating costs.

In the simulations, it is assumed that set-points are determined by the EMS, and short-term fluctuations are managed either by a droop-only frequency control, or an AGC-like control with both droop and supplementary controls, as specified in each case. Also, it is assumed that forecast errors and their associated reserves are only defined for dispatch time intervals $h \geq 2$, as $\chi_1^{MG}(\xi) \approx 0$ in accordance with the EMS's MPC scheme. Furthermore, it is assumed that all controllers are properly tuned, and thus degraded regulation performance can only arise from insufficient reserve allocation. In the event of reserve shortage, it is assumed that auxiliary emergency load shedding and renewable curtailment controllers are triggered, preventing system collapse.

For comparison purposes, three different EMS and frequency control architectures are evaluated in the simulations. The first one corresponds to the Base+Derating (B+DRT) arquitecture, in which a conventional EMS with a droop-only control is considered, similar to those proposed in [22–27]. In this architecture, uncertain power variations are assumed to be handled by: (i) a unique total reserve need, with no distinction between forecast errors

or regulation, which is computed as a percentage of the forecast renewable generation and demand; and (ii) a power capacity derating of generators and batteries, which is computed as percentage of the unit's rating. Note that for this architecture, the change in the expected thermal average power (3.20) and SoC (3.21), battery degradation (3.24), the impact of renewable curtailment on reserve needs (3.26), and limitations on the sharing of short-term fluctuations (3.27) are not represented in the EMS.

The second and third architectures correspond to the Regulation+Droop (R+DRP) and Regulation+AGC (R+AGC) cases, where both consider the formulation described in Section 3.3.5 for the EMS, and handle uncertain power variations through forecast error and regulation reserves, which are computed as a percentage of the forecast renewable generation and demand. In both cases, 4 even partitions with $\overline{S}_l = 0.2\,\forall l \in \mathcal{L}$ are considered for the piecewise linear degradation model (3.3). A droop-only control is assumed in the R+DRP case, whereas an AGC-like control is assumed in the R+AGC case. Accordingly, power sharing constraints (3.27) are considered exclusively in the R+DRP case, with these being enforced only for the first 5min dispatch time intervals, since it is assumed that droop controls are reset by re-dispatch signals every 5min, as per the MPC update rate.

The performance of the three architectures is evaluated by implementing the EMS's optimal dispatch decisions for the first dispatch time interval, and computing the corresponding reference $\boldsymbol{p}$ and delivered $\boldsymbol{p}'$ instantaneous powers (see Sections 3.2.3 and 3.2.4). Delivered instantaneous powers are then used to compute the effective average thermal generation costs, battery degradation costs, load shedding, renewable curtailment, and total number of start-ups and shut-downs. Furthermore, security from a regulation perspective is measured by comparing reference and delivered powers and computing the resulting LHP (3.15), which indicates the percentage of time that insufficient reserves were allocated.

Reserve sizing parameters were computed based on [8] and [5]. Specifically, standard deviations of forecast errors $\tilde{\sigma}_h^{\chi}$ were quantified by linear interpolations using the 1h-ahead and 24h-ahead values reported in [8] (see Table 3.1), whereas standard deviations of short-term fluctuations $\tilde{\sigma}_h^{r}$ were calculated using 6-weeks measurements from KLFN microgrid with a resolution of $\Delta\tau = 1$s (see Table 3.2) [5]. Battery degradation parameters are taken from [42], and the effective degradation resulting from the simulations is obtained using the detailed degradation model (2.7), which is then multiplied by the battery's replacement costs to obtain the resulting degradation costs. The reduction of the battery's energy capacity due to cell capacity fading is not considered in the simulations, as such reduction is negligible within the simulated daily horizon [42]. All simulations are performed using the Julia programming language [91], JuMP package [92], and Gurobi solver [66], on a PC with an Intel Core i7 3.20-GHz processor and 16 GB of RAM under a 64-bit Windows 10 operating system.

Table 3.1: Standard deviation of forecast errors [8]

Source	1h-ahead [%]	24h-ahead [%]
Wind	14.70	30.92
Solar	10.20	14.02
Demand	11.62	15.78

Table 3.2: Standard deviation of short-term fluctuations [5]

Source	5min [%]	15min [%]	30min [%]	1h [%]
Wind	35.43	39.90	42.35	44.58
Solar	16.69	24.54	27.91	33.21
Demand	3.68	6.27	8.93	12.63

3.4.2 Tuning of Reserve Parameters

To ensure a fair comparison between B+DRT, R+DRP, and R+AGC, reserve needs and capacity deratings are calibrated in each case study, so that the resulting load shedding and LHP obtained in the simulations are the same for the three architectures. In the case of load shedding, total reserve needs for B+DRT, and forecast error reserve needs for R+DRP and R+AGC, are determined such that a zero load shedding is obtained in all the case studies. For both KLFN and CIGRE test systems, this is achieved by considering one standard deviation of the forecast errors (see Table 3.1) when computing the reserve needs as a percentage of the forecast renewable generation and load, i.e., $\epsilon^{\chi} = 1$.

In the case of LHP, reserve quantification required a more delicate tuning to ensure that, for each case study, the same LHP is obtained in the three architectures. On the one hand, for B+DRT, simulations showed that directly increasing the total reserve needs did not reduce the LHP, since the basic EMS neglected the effect of droops and typically dispatched generators at maximum power and left the provision of reserves to the batteries, leaving no room in generators for handling short-term fluctuations. This in turn meant that the generators' maximum capacity limit was repeatedly reached, since for a droop-only control a percentage of the short-term fluctuations are forcedly allocated to generators based on their droop gains. Thus, for B+DRT, LHP was calibrated by applying a power capacity percentage derating to generators and batteries. Specifically, the maximum (minimum) capacity limits of generators and batteries considered in the basic EMS where reduced (increased) using a percentage of their installed capacity. This way, some room for handling short-term fluctuations is always left when determining the average power set-points in the basic EMS. On the other hand, for R+DRP and R+AGC,

LHP was directly adjusted by increasing the regulation reserves through the parameter ϵ^r, greatly simplifying the tuning process due to the explicit modeling of short-term fluctuations. During the simulations, three regulation security levels are evaluated based on the resulting LHP, which are described next:

- Low: for which a LHP around 10% is required
- Medium: for which a LHP around 5% is required
- High: for which a LHP around 1% is required

3.4.3 KLFN Microgrid: Settings, Results and Discussion

The performance of the proposed EMS is first evaluated on a test system based on the real-world isolated KLFN microgrid, for which real generation and demand measurements are used [5]. This microgrid is composed of 3 diesel units with capacities of 1500kW, 1000kW, and 600kW, which are only operated one at a time, as per the utility's dispatch rules, and whose parameters are extracted from [27]. For the simulated day, the 600kW unit is assumed to be ON at the start of the day, and a 1026kW peak demand is reached during the evening.

Currently, the KLFN microgrid has low renewable penetration (less than 70kW installed capacity) and no energy storage system; thus, regulation and battery degradation are not an issue at the present time. Therefore, to better illustrate the features of the proposed EMS for regulation and battery degradation modeling, a 1000kW/1000kWh lithium-ion battery is considered, and the renewable installed capacity is increased to reach a 25% renewable energy share (12.5% wind and 12.5% solar) in the simulated day. Additional details about the test system are presented in Appendix A.

The capability to reach the Low, Medium and High regulation security levels for the three EMS models is presented in Table 3.3, which includes the reserve sizing parameters used in the EMS models, the resulting LHP, and a flag indicating if the EMS was successful or not in reaching the desired regulation security level. Observe that only a small capacity derating ($\leq$6%) is needed to reach the desired regulation security levels for the basic EMS (B+DRT), as the KLFN test system has a medium renewable energy share (25%), and its generators and battery have a relatively large power capacity compared to the system's peak load.

The benefits of implementing the proposed EMS model in the KLFN microgrid can be observed in the operational results presented in Table 3.4, which includes total costs,

thermal costs, degradation costs, load shedding, renewable curtailment, and the average computation time per each MPC iteration. Note that the proposed EMS (R+DRP and R+AGC) outperforms the basic EMS (B+DRT) for all regulation security levels, as it reduces total operating costs (1%-9% lower) while keeping sufficiently low computation times for practical implementations ($\leq$ 1s per MPC iteration). A more thorough analysis on the results shows that this improved performance is closely related to the following:

- A more efficient BESS operation with reduced battery degradation, confirmed by comparing the degradation costs presented in Table 3.4. In particular, note that while the basic EMS uses the battery mostly for energy-shifting (5min timescale), the proposed EMS instead uses the battery mostly for reserve provision (1s timescale), as the latter requires shallower charging/discharging cycles relative to the energy shifting case, resulting in lower battery degradation.

- The strategic use of renewable curtailment for an enhanced system operation, confirmed by comparing the renewable curtailment presented in Table 3.4. In particular, observe that while the basic EMS typically dispatches renewable generation at its maximum available capacity at all times, the proposed EMS employs renewable curtailment during some critical operating hours in order to reduce the system's regulation/reserve needs, and to prevent deep battery charging/discharging cycles that would result in a large battery degradation.

It is also worth highlighting that, in terms of operating costs, no significant differences are observed between using the proposed EMS with a simple droop-only control (R+DRP) and a more advanced AGC (R+AGC) for the KLFN microgrid.

3.4.4 CIGRE Microgrid: Settings, Results and Discussion

The proposed EMS is evaluated here on a more complex microgrid based on a modified CIGRE benchmark test system from [27]. This microgrid has a 5755 kW peak demand, and is composed of 3 diesel generators (4700kW combined capacity) and 2 Combined Heat-and-Power units (810kW combined capacity). The microgrid also has multiple energy storage systems, with a total installed capacity of 1324kW/1324kWh, which for simplicity are modeled as a single lithium-ion battery. Also, the renewable installed capacity is increased to reach a 50% renewable energy share. Additional details about the test system are presented in Appendix A.

The simulation results for the CIGRE microgrid are shown in Tables 3.5 and 3.6, in which regulation security are operational performance results are indicated, respectively.

Table 3.3: Security compliance results for KLFN system with 25% renewable energy share

Regul. secur.	EMS model	Reserve sizing		LHP [%]	Success flag
		Derating [%]	ϵ^r		
Low	B+DRT	2.0	-	9.9	✓
	R+DRP	-	0.215	9.6	✓
	R+AGC	-	0.220	9.7	✓
Medium	B+DRT	3.0	-	5.0	✓
	R+DRP	-	0.500	5.1	✓
	R+AGC	-	0.600	4.9	✓
High	B+DRT	6.0	-	0.9	✓
	R+DRP	-	1.500	1.0	✓
	R+AGC	-	1.300	1.1	✓

Observe that, unlike the KLFN microgrid, the basic EMS (B+DRT) fails to reach the High regulation security level, reaching a minimum of 2.3% (instead of 1%) LHP. Furthermore, note that in this case, a significant derating ($\geq$19%) and load shedding is needed for the basic EMS to reach the desired LHP, which in turn causes a pronounced increase in total costs for the medium and high regulation security levels. This poor performance stems from the large renewable energy share (50%) of the CIGRE test system, alongside the inadequacy of the basic EMS to properly model large short-term power fluctuations. In contrast, the proposed EMSs (R+DRT and R+AGC) yield the desired LHP at reduced costs, since short-term fluctuations are properly modeled in this case.

As also noted for the KLFN microgrid, the proposed EMSs show overall better performance for the CIGRE system in terms of total costs and battery degradation while keeping computational tractability, and also use renewable curtailment as a regulation/reserve management mechanism. However, and unlike the small KLFN microgrid, the use of an AGC (R+AGC) instead of a simple droop-only control (R+DRP) may yield significant savings in terms of operating costs for the more complex CIGRE microgrid (3%-18% cost reduction).

In summary, the proposed EMS model outperforms the conventional EMS model, achieving reduced operational costs and battery degradation in both test systems for a wide range of regulation security levels, while maintaining computational tractability. This overall better performance is the result of explicitly modeling short-term fluctuations and their impact on regulation/reserve needs, battery degradation, and renewable curtailment.

Table 3.4: Operational results for KLFN system with 25% renewable energy share

Regul. secur.	EMS model	Total costs [kUSD]	Thermal costs [kUSD]	Degrad. costs [USD]	Load shed. [kWh]	Renew. curt. [kWh]	Comp. time [s]
Low	B+DRT	3.08	2.89	195	0	0	0.3
	R+DRP	2.81	2.78	27	0	118	0.7
	R+AGC	2.81	2.80	12	0	118	0.6
Medium	B+DRT	2.91	2.69	214	0	0	0.3
	R+DRP	2.81	2.79	16	0	118	0.7
	R+AGC	2.81	2.79	14	0	118	0.6
High	B+DRT	2.85	2.68	167	0	0	0.3
	R+DRP	2.81	2.79	17	0	118	0.7
	R+AGC	2.80	2.79	11	0	118	0.6

3.5 Summary

Due to the low-inertia and significant renewable generation variability in isolated microgrids, short time-scale fluctuations in the order of seconds can play a relevant role in the microgrid's operation and control. In this context, the present chapter discussed the design of a novel EMS model that takes into account the operational impact of the short-term fluctuations stemming from renewable generation rapid changes, and the role that renewable curtailment and batteries, including their degradation, can play to counter-balance these variations. The proposed EMS was evaluated on two realistic test systems, showing the benefits of including short-term fluctuations and battery degradation in the EMS's decision-making process. Such benefits include the reduction of total operating costs and battery degradation, while keeping sufficiently low computation times for near real-time practical applications. The main content of this chapter has been published in [93].

Table 3.5: Security compliance results for CIGRE system with 50% renewable energy share

Regul. secur.	EMS Model	Reserve sizing		LHP [%]	Success flag
		Derating [%]	ϵ^r		
Low	B+DRT	19.0	-	10.2	✓
	R+DRP	-	1.130	10.1	✓
	R+AGC	-	1.000	10.4	✓
Medium	B+DRT	28.5	-	4.8	✓
	R+DRP	-	1.500	5.1	✓
	R+AGC	-	1.300	4.9	✓
High	B+DRT	30.0	-	2.3†	✗
	R+DRP	-	3.000	0.8	✓
	R+AGC	-	2.500	0.9	✓

†1% LHP could not be achieved; instead, the minimum achievable LHP is indicated

Table 3.6: Operational results for CIGRE system with 50% renewable energy share

Regul. secur.	EMS Model	Total costs [kUSD]	Thermal costs [kUSD]	Degrad. costs [USD]	Load shed. [kWh]	Renew. curt. [kWh]	Comp. time [s]
Low	B+DRT	8.60	8.44	160	0	79	0.5
	R+DRP	8.73	8.60	136	0	2263	3.6
	R+AGC	8.48	8.42	58	0	1644	2.5
Medium	B+DRT	11.58	8.92	249	201	416	0.5
	R+DRP	9.15	8.98	168	0	4211	4.8
	R+AGC	8.43	8.36	74	0	2095	2.8
High	B+DRT	60.88	8.76	331	4316	3301	0.2
	R+DRP	10.67	10.53	132	0	10402	7.5
	R+AGC	8.71	8.63	71	0	3622	3.0

Chapter 4

Integrating Frequency-Dynamics in Microgrid Operation

Chapter 3 presented an EMS embedding short-term power fluctuations and their impact on operations, as these play a significant role in isolated microgrids due to their low-inertia and significant renewable energy integration. However, such EMS does not incorporate the impact of second-to-second fluctuations on the frequency regulation performance of isolated microgrids, which is particularly relevant given the system's low-inertia and existing DER operating standards constraining frequency deviation and RoCoF values (e.g., [86]). Hence, this chapter presents enhancements to the EMS described in Chapter 3 to consider the impact of short-term power fluctuations on transient frequency dynamics. For this purpose, accurate linear equations describing frequency excursions and RoCoF values in the presence of second-to-second power imbalances are developed, which then serve as a basis for the design of a computationally efficient EMS with frequency and RoCoF limit constraints suitable for near real-time practical applications. Exhaustive transient simulations on a realistic test system using detailed frequency dynamic and control models are presented, demonstrating the modeling accuracy of the proposed frequency-constrained EMS and the benefits resulting from its implementation in isolated microgrids. Such benefits include the reduction of total operating cost while keeping an adequate frequency regulation performance compliant with current DER operating standards.

The chapter is organized as follows: In Section 4.1, modifications to the EMS for the inclusion of frequency dynamics are presented. In Section 4.2, computational experiments and results are presented, demonstrating the relevance and advantages of the proposed frequency-constrained EMS. Finally, in Section 4.3, a summary of the topics presented in this chapter is provided.

4.1 Energy Management System Model

In this section, changes to the EMS model presented in Chapter 3 are presented, which aim to improve its modeling accuracy and integrate frequency dynamics in its decision making process. This includes modifications to the equations and constraints of the EMS optimization model, as well as changes in the general EMS architecture required for its implementation.

4.1.1 Capacity and Reserve Constraints

First, modifications to the capacity and reserve constraints originally presented in Sections 3.2.3 and 3.3.1 are discussed. In the case of thermal generators, their range of feasible average power set-points (3.16) can be extended, as the steady-state power capacity limits $\overline{P}_g^G$ and $\underline{P}_g^G$ of flexible diesel generators may be temporarily violated for a few seconds [2], resulting in the following updated capacity constraints $\forall g \in \mathcal{G}$:

$$\hat{p}_{g,h}^G + \Delta p_{g,h}^{G,\chi,\uparrow} \leq \overline{P}_g^G \, u_{g,h}^G \quad \forall h \in \mathcal{H}^r \tag{4.1a}$$

$$\hat{p}_{g,h}^G - \Delta p_{g,h}^{G,\chi,\downarrow} \geq \underline{P}_g^G u_{g,h}^G \quad \forall h \in \mathcal{H}^r \tag{4.1b}$$

$$\hat{p}_{g,h}^G + \Delta p_{g,h}^{G,\chi,\uparrow} + \Delta p_{g,h}^{G,r,\uparrow} \leq \overline{PT}_g^G \, u_{g,h}^G \quad \forall h \in \mathcal{H}^r \tag{4.1c}$$

$$\hat{p}_{g,h}^G - \Delta p_{g,h}^{G,\chi,\downarrow} - \Delta p_{g,h}^{G,r,\downarrow} \geq \underline{PT}_g^G \, u_{g,h}^G \quad \forall h \in \mathcal{H}^r \tag{4.1d}$$

$$\hat{p}_{g,h}^G + \Delta p_{g,h}^{G,\chi,\uparrow} + \Delta p_{g,h}^{G,r,\uparrow} \leq \overline{P}_g^G \, u_{g,h}^G \quad \forall h \in \mathcal{H} \setminus \mathcal{H}^r \tag{4.1e}$$

$$\hat{p}_{g,h}^G - \Delta p_{g,h}^{G,\chi,\downarrow} - \Delta p_{g,h}^{G,r,\downarrow} \geq \underline{P}_g^G \, u_{g,h}^G \quad \forall h \in \mathcal{H} \setminus \mathcal{H}^r \tag{4.1f}$$

where $\overline{PT}_g^G$ and $\underline{PT}_g^G$ are generator g's transient maximum and minimum power, as per Figure 2.6, with $\overline{PT}_g^G \geq \overline{P}_g^G$ and $\underline{PT}_g^G \leq \underline{P}_g^G$. Note that in the above equations, a distinction is made between the first $\mathcal{H}^r \subset \mathcal{H}$ dispatch time intervals, and the remaining dispatch time intervals resulting from the set difference $\mathcal{H} \setminus \mathcal{H}^r$. This is related to the use of growing time-steps in the MPC implementation of the microgrid EMS, for which the first $\mathcal{H}^r$ dispatch time intervals have a time-step equal to the MPC update rate (e.g., 5min), and the remaining dispatch time intervals $\mathcal{H} \setminus \mathcal{H}^r$ have longer time-steps [22–27]. Accordingly, equations for the first $\mathcal{H}^r$ time intervals are differentiated from the rest, as frequency controls regulate the units' power outputs in this finer time frame, whereas for the longer time-steps those outputs are changed through re-dispatch signals from the EMS.

In the case of batteries, reserves can be provided not only by increasing charging or discharging power set-points, as per (3.17), but also by decreasing such set-points, resulting

in an additional system flexibility [94]. Thus, to capture these effect, additional battery reserve variables $\Delta p^{B,C,\chi,\uparrow}_{b,l,h}$, $p^{B,C,r,\uparrow}_{b,l,h}$, $\Delta p^{B,D,\chi,\downarrow}_{b,l,h}$, and $\Delta p^{B,D,r,\downarrow}_{b,l,h}$ are defined, which are limited by the following constraints:

$$\Delta p^{B,C,\chi,\uparrow}_{b,l,h} + \Delta p^{B,C,r,\uparrow}_{b,l,h} \leq c^{B}_{b,l,h} \qquad \forall b \in \mathcal{B}, l \in \mathcal{L}, h \in \mathcal{H} \tag{4.2a}$$

$$\Delta p^{B,D,\chi,\downarrow}_{b,l,h} + \Delta p^{B,D,r,\downarrow}_{b,l,h} \leq d^{B}_{b,l,h} \qquad \forall b \in \mathcal{B}, l \in \mathcal{L}, h \in \mathcal{H} \tag{4.2b}$$

where $\Delta p^{B,C,\chi,\uparrow}_{b,l,h}$ and $\Delta p^{B,C,r,\uparrow}_{b,l,h}$ are the upward forecast error and regulation reserves provided by decreasing the battery's charging; and $\Delta p^{B,D,\chi,\downarrow}_{b,l,h}$ and $\Delta p^{B,D,r,\downarrow}_{b,l,h}$ are the downward forecast error and regulation reserves provided by decreasing the battery's discharging, respectively. The definition of the new battery reserve variables also affects battery energy requirements (3.18), which are redefined as follows $\forall b \in \mathcal{B}, l \in \mathcal{L}, h \in \mathcal{H}$:

$$\begin{aligned} & s^{B}_{b,l,h-1} + \frac{\Delta T_h \, \eta^{B,C}_{b}}{E_b} \left(c^{B}_{b,l,h} + \Delta p^{B,C,\chi,\downarrow}_{b,l,h} + \frac{1}{2} \Delta p^{B,C,r,\downarrow}_{b,l,h} \right) \\ & - \frac{\Delta T_h}{E_b \, \eta^{B,D}_{b}} \left(d^{B}_{b,l,h} - \Delta p^{B,D,\chi,\downarrow}_{b,l,h} - \frac{1}{2} \Delta p^{B,D,r,\downarrow}_{b,l,h} \right) \leq \overline{S}_{b,l} \end{aligned} \tag{4.3a}$$

$$\begin{aligned} & s^{B}_{b,l,h-1} - \frac{\Delta T_h}{E_b \, \eta^{B,D}_{b}} \left(d^{B}_{b,l,h} + \Delta p^{B,D,\chi,\uparrow}_{b,l,h} + \frac{1}{2} \Delta p^{B,D,r,\uparrow}_{b,l,h} \right) \\ & + \frac{\Delta T_h \, \eta^{B,C}_{b}}{E_b} \left(c^{B}_{b,l,h} - \Delta p^{B,C,\chi,\uparrow}_{b,l,h} - \frac{1}{2} \Delta p^{B,C,r,\uparrow}_{b,l,h} \right) \geq 0 \end{aligned} \tag{4.3b}$$

in which additional battery slack capacities resulting from reduced (dis)charging have been incorporated. Note that unlike (3.18), regulation reserves Δp^{r} here include a 1/2 term, since upward (downward) regulation reserves are assumed to be deployed at full capacity at most for half of the dispatch time interval length ΔT_h, based on the zero-mean characteristic of $\boldsymbol{r}$ in (3.1).

Based on modifications (4.1)-(4.2), the forecast error reserve balance (3.10) can be redefined as follows $\forall h \in \mathcal{H}$:

$$\zeta^{\chi}_{h} = \sum_{g \in \mathcal{G}} \Delta p^{G,\chi,\uparrow}_{g,h} + \sum_{b \in \mathcal{B}} \sum_{l \in \mathcal{L}} \left(\Delta p^{B,D,\chi,\uparrow}_{b,l,h} + \Delta p^{B,C,\chi,\uparrow}_{b,l,h} \right) \tag{4.4a}$$

$$\zeta^{\chi}_{h} = \sum_{g \in \mathcal{G}} \Delta p^{G,\chi,\downarrow}_{g,h} + \sum_{b \in \mathcal{B}} \sum_{l \in \mathcal{L}} \left(\Delta p^{B,D,\chi,\downarrow}_{b,l,h} + \Delta p^{B,C,\chi,\downarrow}_{b,l,h} \right) \tag{4.4b}$$

The regulation reserve balance (3.11) can also be redefined in a similar manner, but with the difference that as in (4.1), the first $\mathcal{H}^{r}$ dispatch time intervals are distinguished from

the remaining $\mathcal{H} \setminus \mathcal{H}^r$ dispatch time intervals, since frequency dynamics and control play a key role for this type of reserves. In particular, the following constraints are considered for the first dispatch time intervals, i.e., $\forall h \in \mathcal{H}^r$:

$$\zeta_h^r = \sum_{g \in \mathcal{G}} \Delta p_{g,h}^{G,r,\uparrow} + \sum_{b \in \mathcal{B}} \sum_{l \in \mathcal{L}} \left(\Delta p_{b,l,h}^{B,D,r,\uparrow} + \Delta p_{b,l,h}^{B,C,r,\uparrow} \right) + \Delta p_h^{PF,r,\uparrow} + \Delta p_h^{VFC,r,\uparrow} \tag{4.5a}$$

$$\zeta_h^r = \sum_{g \in \mathcal{G}} \Delta p_{g,h}^{G,r,\downarrow} + \sum_{b \in \mathcal{B}} \sum_{l \in \mathcal{L}} \left(\Delta p_{b,l,h}^{B,D,r,\downarrow} + \Delta p_{b,l,h}^{B,C,r,\downarrow} \right) + \Delta p_h^{PF,r,\downarrow} + \Delta p_h^{VFC,r,\downarrow} \tag{4.5b}$$

where additional regulation capabilities $\Delta p_h^{PF,r,\uparrow}$, $\Delta p_h^{PF,r,\downarrow}$, $\Delta p_h^{VFC,r,\uparrow}$ and $\Delta p_h^{VFC,r,\downarrow}$, stemming from frequency sensitive loads and VFCs are considered, as discussed in detail in Section 4.1.3. In contrast, the following constraints are considered for the remaining dispatch time intervals, i.e., $\forall h \in \mathcal{H} \setminus \mathcal{H}^r$:

$$\zeta_h^r = \sum_{g \in \mathcal{G}} \Delta p_{g,h}^{G,r,\uparrow} + \sum_{b \in \mathcal{B}} \sum_{l \in \mathcal{L}} \left(\Delta p_{b,l,h}^{B,D,r,\uparrow} + \Delta p_{b,l,h}^{B,C,r,\uparrow} \right) \tag{4.6a}$$

$$\zeta_h^r = \sum_{g \in \mathcal{G}} \Delta p_{g,h}^{G,r,\downarrow} + \sum_{b \in \mathcal{B}} \sum_{l \in \mathcal{L}} \left(\Delta p_{b,l,h}^{B,D,r,\downarrow} + \Delta p_{b,l,h}^{B,C,r,\downarrow} \right) \tag{4.6b}$$

for which $\Delta p_h^{PF,r,\uparrow}$, $\Delta p_h^{PF,r,\downarrow}$, $\Delta p_h^{VFC,r,\uparrow}$ and $\Delta p_h^{VFC,r,\downarrow}$ are not considered.

4.1.2 Operational Impact of Reserve Provision

As previously discussed in Section 3.3.1, forecast error and regulation reserves have an impact on the expected average thermal generation, battery SoC, and battery degradation, which can be captured through the ERU metric. In (3.19), this metric was computed using the mean absolute deviation (mad) of power imbalances; however, here the more accurate truncated absolute expectation (tae) is used instead, which can be defined as follows:

$$\text{tae}(Z, \zeta) = \int_{-\zeta}^{\zeta} |z| f(z) dz + \zeta \left[\int_{-\infty}^{-\zeta} f(z) dz + \int_{\zeta}^{\infty} f(z) dz \right] \tag{4.7}$$

where Z is a random variable representing uncertain power imbalances, $f(z)$ is its associated probability density function, and ζ is the available reserve capacity. Note that this formulation closely resembles $\text{mad}(Z) = \mathbb{E}(|Z|)$, but with the difference that $f(z)$ is truncated for $|z| \geq \zeta$, and the corresponding truncated values are clustered at $z = \pm\zeta$. This alternative definition is motivated by how reserves are deployed in practice, since if insufficient reserves are available, i.e., $|z| \geq \zeta$, only a reserve equal to $\pm\zeta$ will be deployed.

Based on (4.7), the updated ERU of the forecast error and regulation reserves can then be computed as follows:

$$\varphi_h^{\chi} = \frac{\text{tae}\left(\chi_h^{MG}, \zeta_h^{\chi}\right)}{\zeta_h^{\chi}}, \quad \varphi_h^{r} = \frac{\text{tae}\left(\boldsymbol{r}_h^{MG}, \zeta_h^{r}\right)}{\zeta_h^{r}} \tag{4.8}$$

Furthermore, assuming that both χ_h^{MG} and $\boldsymbol{r}_h^{MG}$ resemble a normal distribution, and replacing (3.6) and (3.9), one has that:

$$\varphi_h^{\chi} = \frac{1}{\epsilon^{\chi}}\sqrt{\frac{2}{\pi}}\left[1 - \exp\left(-\frac{\epsilon^{\chi 2}}{2}\right)\right] + 1 - \text{erf}\left(\frac{\epsilon^{\chi}}{\sqrt{2}}\right) \tag{4.9a}$$

$$\varphi_h^{r} = \frac{1}{\epsilon^{r}}\sqrt{\frac{2}{\pi}}\left[1 - \exp\left(-\frac{\epsilon^{r 2}}{2}\right)\right] + 1 - \text{erf}\left(\frac{\epsilon^{r}}{\sqrt{2}}\right) \tag{4.9b}$$

where exp and erf are the exponential and Gauss error functions, respectively.

Based on (4.9), the change in the expected average power of generators (3.20), battery's SoC (3.21), and battery degradation (3.23) due to the reserve provision can be adapted as follows:

$$\Delta e_{g,h}^{G} = \frac{\varphi_h^{\chi}}{2}\left(\Delta p_{g,h}^{G,\chi,\uparrow} - \Delta p_{g,h}^{G,\chi,\downarrow}\right) + \frac{\varphi_h^{r}}{2}\left(\Delta p_{g,h}^{G,r,\uparrow} - \Delta p_{g,h}^{G,r,\downarrow}\right) \tag{4.10}$$

$$\begin{aligned}
\Delta s_{b,l,h}^{B} = \frac{\varphi_h^{\chi}}{2}\frac{\Delta T_h}{E_b}\eta_b^{B,C}\left(\Delta p_{b,l,h}^{B,C,\chi,\downarrow} - \Delta p_{b,l,h}^{B,C,\chi,\uparrow}\right) \\
- \frac{\varphi_h^{\chi}}{2}\frac{\Delta T_h}{E_b}\frac{1}{\eta_b^{B,D}}\left(\Delta p_{b,l,h}^{B,D,\chi,\uparrow} - \Delta p_{b,l,h}^{B,D,\chi,\downarrow}\right) \\
+ \frac{\varphi_h^{r}}{2}\frac{\Delta T_h}{E_b}\eta_b^{B,C}\left(\Delta p_{b,l,h}^{B,C,r,\downarrow} - \Delta p_{b,l,h}^{B,C,r,\uparrow}\right) \\
- \frac{\varphi_h^{r}}{2}\frac{\Delta T_h}{E_b}\frac{1}{\eta_b^{B,D}}\left(\Delta p_{b,l,h}^{B,D,r,\uparrow} - \Delta p_{b,l,h}^{B,D,r,\downarrow}\right)
\end{aligned} \tag{4.11}$$

$$\Delta\phi_{b,l,h} = \frac{\hat{\phi}_{b,l}}{2}\frac{\varphi_h^{\chi}}{2}\frac{\Delta T_h}{E_b}\eta_b^{B,C}\left(\Delta p_{b,l,h}^{B,C,\chi,\downarrow} - \Delta p_{b,l,h}^{B,C,\chi,\uparrow}\right) + \frac{\hat{\phi}_{b,l}}{2}\frac{\varphi_h^{\chi}}{2}\frac{\Delta T_h}{E_b}\frac{1}{\eta_b^{B,D}}\left(\Delta p_{b,l,h}^{B,D,\chi,\uparrow} - \Delta p_{b,l,h}^{B,D,\chi,\downarrow}\right) + \frac{\hat{\phi}_{b,l}}{2}\frac{\varphi_h^{r}}{2}\frac{\Delta T_h}{E_b}\eta_b^{B,C}\left(\Delta p_{b,l,h}^{B,C,r,\downarrow} - \Delta p_{b,l,h}^{B,C,r,\uparrow}\right) + \frac{\hat{\phi}_{b,l}}{2}\frac{\varphi_h^{r}}{2}\frac{\Delta T_h}{E_b}\frac{1}{\eta_b^{B,D}}\left(\Delta p_{b,l,h}^{B,D,r,\uparrow} - \Delta p_{b,l,h}^{B,D,r,\downarrow}\right) \quad (4.12)$$

Note that unlike the original equations, and similar to (4.3), additional battery slack capacities resulting from reduced (dis)charging are incorporated, and a 1/2 term is included for regulation reserves, as it is assumed that both upward and downward regulation reserves are deployed during half of each dispatch time interval h.

4.1.3 Frequency-Dynamics Constraints

Unlike previous works on microgrid EMS, explicit frequency constraints are considered here, such that an adequate frequency regulation performance is ensured in daily microgrid operations. In the case of thermal generators, their maximum deliverable short-term regulation is defined by their frequency-droop κ_g^G, and the maximum frequency deviation limit $\overline{\Delta f}$ imposed by DER operating standards [86], yielding the following constraint:

$$\Delta p_{g,h}^{G,r,\uparrow} \leq \frac{\overline{\Delta f}}{f_0}\frac{\overline{P}_g^G}{\kappa_g^G} \quad \forall g \in \mathcal{G}, h \in \mathcal{H}^r \quad (4.13a)$$

$$\Delta p_{g,h}^{G,r,\downarrow} \leq \frac{\overline{\Delta f}}{f_0}\frac{\overline{P}_g^G}{\kappa_g^G} \quad \forall g \in \mathcal{G}, h \in \mathcal{H}^r \quad (4.13b)$$

where f_0 is the microgrid's nominal frequency in Hz. Similarly, for batteries, the maximum deliverable short-term regulation is given by the following constraints $\forall b \in \mathcal{B}, h \in \mathcal{H}^r$:

$$\sum_{l\in\mathcal{L}}\left(\Delta p_{b,l,h}^{B,D,r,\uparrow} + \Delta p_{b,l,h}^{B,C,r,\uparrow}\right) \leq \frac{\overline{\Delta f}}{f_0}\frac{\overline{P}_b^B}{\kappa_b^B} \quad (4.14a)$$

$$\sum_{l\in\mathcal{L}}\left(\Delta p_{b,l,h}^{B,C,r,\downarrow} + \Delta p_{b,l,h}^{B,D,r,\downarrow}\right) \leq \frac{\overline{\Delta f}}{f_0}\frac{\overline{P}_b^B}{\kappa_b^B} \quad (4.14b)$$

where κ_b^B is the battery's frequency droop.

As previously discussed in Section 2.4.2, loads provide a damping factor stemming from their frequency sensitivity K^{PF}. This feature is included in reserve regulation balance (4.5) through variables $\Delta p_h^{PF,r,\uparrow}$ and $\Delta p_h^{PF,r,\downarrow}$, which are constrained as follows $\forall h \in \mathcal{H}^r$:

$$\Delta p_h^{PF,r,\uparrow} \leq \frac{\overline{\Delta f}}{f_0} K^{PF} \left(\hat{P}_h^L - ls_h \right) \tag{4.15a}$$

$$\Delta p_h^{PF,r,\downarrow} \leq \frac{\overline{\Delta f}}{f_0} K^{PF} \left(\hat{P}_h^L - ls_h \right) \tag{4.15b}$$

Loads also present a voltage sensitivity K^{PV}, which can be exploited to provide additional frequency damping through the inclusion of VFCs in diesel generators (see Figure 2.8). This additional flexibility is incorporated in (4.5) through variables $\Delta p_h^{VFC,r,\uparrow}$ and $\Delta p_h^{VFC,r,\downarrow}$, which are constrained as follows $\forall h \in \mathcal{H}^r$:

$$\Delta p_h^{VFC,r,\uparrow} \leq \frac{\overline{\Delta f}}{f_0} K^{VFC} K^{PV} \left(\hat{P}_h^L - ls_h \right) \tag{4.16a}$$

$$\Delta p_h^{VFC,r,\downarrow} \leq \frac{\overline{\Delta f}}{f_0} K^{VFC} K^{PV} \left(\hat{P}_h^L - ls_h \right) \tag{4.16b}$$

Another relevant aspect to consider in microgrid frequency regulation is the RoCoF limit imposed by DER operating standards [86], since excessively large RoCoF values might lead to operating issues such as loss of synchronism in converters' phase locked loops [11]. Accordingly, a RoCoF constraint is also considered here, which is derived based on the microgrid dynamic model described in Section 2.4.4. Hence, taking into account that automatic frequency controllers have an inherent time delay and thus are not immediately available, the instantaneous frequency deviation resulting from short-term power fluctuations can be described by:

$$2IN^{SYS} \frac{d\Delta f(t)}{dt} + K^{LD} \Delta f(t) = r^W(t) + r^S(t) - r^L(t). \tag{4.17}$$

Thus, neglecting load damping K^{LD}, as in [40], one can obtain the following overestimation for the instantaneous RoCoF:

$$RoCoF(t) = \frac{1}{2IN^{SYS}} \left[r^W(t) + r^S(t) - r^L(t) \right]. \tag{4.18}$$

Additionally, given that the focus of this thesis is on isolated microgrid daily operations, i.e., without contingencies, one can assume that the continuous-time short-term fluctuations $r(t)$ change linearly between each short time interval $j \in \mathcal{J}$, as follows:

$$r(t) = \underbrace{\left(\frac{r_{h,j+1} - r_{h,j}}{\Delta\tau} \right)}_{\partial r_{h,j}} t \qquad \forall t \in [0, \Delta\tau] \tag{4.19}$$

where $r_{h,j}$ is the short-term power fluctuation at short time interval j within dispatch time interval h, as per (3.1); $\Delta\tau$ is the time-step length of short time intervals $j \in \mathcal{J}$; and ∂r_{hj} is defined as the short-term power fluctuation ramp. Thus, one can replace (4.19) in (4.18) to obtain:

$$RoCoF(t) = \frac{1}{2IN^{SYS}} \underbrace{\left[\partial r^{W}_{h,j} + \partial r^{S}_{h,j} - \partial r^{L}_{h,j} \right]}_{\partial r^{MG}_{h,j}} t \tag{4.20}$$

where $\partial r^{MG}_{h,j}$ is the microgrid's net short-term fluctuation ramp.

Similar to the forecast error and regulation reserve requirements described in Sections 3.2.1, 3.2.2, and 3.3.2, one can use the microgrid's net short-term fluctuation ramp to define a *regulation-ramp reserve need* $\zeta^{\partial r}_{h}$, which serves as a basis for deriving a RoCoF constraint, and can be defined as follows:

$$\boldsymbol{\partial r}^{MG}_{h}(\xi) = \hat{p}^{W}_{h}\, \boldsymbol{\partial \tilde{r}}^{W}_{h}(\xi) + \hat{p}^{S}_{h}\, \boldsymbol{\partial \tilde{r}}^{S}_{h}(\xi) - \hat{P}^{L}_{h}\, \boldsymbol{\partial \tilde{r}}^{L}_{h}(\xi) \tag{4.21a}$$

$$\text{std}\left(\boldsymbol{\partial r}^{MG}_{h}\right)^2 = \left(\hat{P}^{L}_{h}\, \tilde{\sigma}^{\partial r,L}_{h}\right)^2 + \left(\hat{p}^{W}_{h}\, \tilde{\sigma}^{\partial r,W}_{h}\right)^2 + \left(\hat{p}^{S}_{h}\, \tilde{\sigma}^{\partial r,S}_{h}\right)^2 \tag{4.21b}$$

$$\zeta^{\partial r}_{h} = \epsilon^{\partial r}\, \text{std}\left(\boldsymbol{\partial r}^{MG}_{h}\right) \tag{4.21c}$$

$$\zeta^{\partial r}_{h} = \epsilon^{\partial r} \left[\left(\hat{P}^{L}_{h}\, \tilde{\sigma}^{\partial r,L}_{h}\right)^2 + \left(\hat{p}^{W}_{h}\, \tilde{\sigma}^{\partial r,W}_{h}\right)^2 + \left(\hat{p}^{S}_{h}\, \tilde{\sigma}^{\partial r,S}_{h}\right)^2 \right]^{1/2} \tag{4.21d}$$

where $\boldsymbol{\partial \tilde{r}}^{L}_{h}$, $\boldsymbol{\partial \tilde{r}}^{W}_{h}$, and $\boldsymbol{\partial \tilde{r}}^{S}_{h}$ are zero-mean random vectors representing the normalized short-term fluctuation ramps of demand, wind generation, and solar generation, respectively; $\tilde{\sigma}^{\partial r,L}_{h} = \text{std}\left(\boldsymbol{\partial \tilde{r}}^{L}_{h}\right)$, $\tilde{\sigma}^{\partial r,W}_{h} = \text{std}\left(\boldsymbol{\partial \tilde{r}}^{W}_{h}\right)$, and $\tilde{\sigma}^{\partial r,S}_{h} = \text{std}\left(\boldsymbol{\partial \tilde{r}}^{S}_{h}\right)$; and $\epsilon^{\partial r}$ is a parameter for adjusting the desired confidence level. Note that as in (3.26), the regulation-ramp reserve need constraint (4.21d) can be convexified and thus be represented by a cutting-planes algorithm [89].

Based on (4.21), a constraint for ensuring a proper RoCoF performance can be derived. Such constraint is obtained by replacing $\partial r^{MG}_{h,j}$ in (4.20) by $\zeta^{\partial r}_{h}$, and assuming that automatic frequency controllers will not act until $t = T^{FC}$ due to their inherent time delay.

This yields the following constraint for ensuring RoCoF limit compliance:

$$\zeta_h^{\partial r} \leq \frac{2\,\overline{RoCoF}}{T^{FC} f_0} \underbrace{\sum_{g \in \mathcal{G}} u_{g,h}^{G}\, IN_g^{G}}_{IN^{SYS}} \quad \forall h \in \mathcal{H} \tag{4.22}$$

where IN_g^G is the synchronous inertia provided by each available generator g, and $\overline{RoCoF}$ is the absolute RoCoF limit in Hz/s. Thus, this constraint considers that, as per (4.21), the amount of renewable generation injected into the microgrid will result in a higher regulation-ramp reserve need $\zeta_h^{\partial r}$, ultimately leading to a higher synchronous inertia requirement for the system. It is also worth highlighting that battery virtual inertia IN^B is not considered in (4.22), since it is affected by converter control delays and thus not immediately available for instantaneous RoCoF damping (see Figure 2.7); however, this assumption can readily be relaxed by adding a virtual inertia component in (4.22).

It is important to highlight that modern frequency-constrained operational models for bulk power systems typically also consider a frequency nadir constraint to limit frequency deviations, as such constraint plays a significant role in the presence of stepwise power disturbances resulting from outages [37–41]. However, such type of constraint is not considered here, since: (i) this thesis focuses on short-term power fluctuations stemming from renewable generation and loads, which change in a linear, instead of stepwise, manner; and (ii) unlike bulk power systems, major contingencies such as large generator outages are typically not considered in isolated microgrid dispatch models, as including these would result in impractical large operating costs. The validity of using Quasi-Steady-State (QSS) frequency constraints (4.13)-(4.16) and RoCoF constraint (4.22) for modeling frequency and RoCoF dynamics in isolated microgrid daily operations is discussed in Section 4.2.5.

4.1.4 Optimization Model and Architecture

Based on the equations presented in previous sections, an updated EMS optimization model embedding frequency dynamics can be formulated. The resulting optimization model cor-

responds to a MILP problem that can be solved by off-the-shelf solvers:

$$
\begin{aligned}
\min_{\boldsymbol{x},\boldsymbol{y}} \quad & \mathcal{F}^{OBJ}\left(\boldsymbol{x},\boldsymbol{y}\right) \\
\text{s.t.} \quad & \boldsymbol{x} \in \{0,1\}\,,\ \boldsymbol{y} \geq 0 \\
& \text{Reserves and power balance: (4.4)–(4.6), (3.25), (3.26), (3.28)} \\
& \text{Thermal generators: (4.1), (4.10), (3.29), (3.30)} \\
& \text{Batteries and degradation: (3.17), (4.2), (4.3), (3.22), (3.24),} \\
& \qquad\qquad\qquad\qquad\qquad \text{(4.11), (4.12), (3.31)} \\
& \text{Frequency dynamics: (4.13)-(4.16), (4.21d), (4.22)}
\end{aligned}
$$

where the objective function $\mathcal{F}^{OBJ}$ includes thermal generation, battery degradation, and load shedding costs; $\boldsymbol{x} = \left[\boldsymbol{u}^{G}, \boldsymbol{v}^{G}, \boldsymbol{w}^{G}\right]$ are binary decision variables; and $\boldsymbol{y} = \left[\hat{\boldsymbol{p}}^{G}, \hat{\boldsymbol{p}}^{W}, \hat{\boldsymbol{p}}^{S}, \Delta\boldsymbol{p}^{G}, \Delta\boldsymbol{p}^{B}, \Delta\boldsymbol{p}^{VFC}, \Delta\boldsymbol{p}^{PF}, \boldsymbol{s}^{B}, \boldsymbol{c}^{B}, \boldsymbol{d}^{B}, \boldsymbol{ls}, \boldsymbol{\zeta}\right]$ are non-negative continuous decisions variables.

The architecture required to implement the proposed frequency-constrained EMS model is presented in Figure 4.1. Note that unlike the original architecture presented in Figure 3.2, this architecture allows the incorporation of additional modules for handling other possibly relevant aspects not modeled in the EMS optimization model. For example, an additional Optimal Power Flow module with AC power flow equations can be included to compute reactive power dispatch set-points, as in [22]. It is also worth highlighting that participation factors are omitted in Figure 4.1, as practical isolated microgrids typically have a droop-only control for frequency regulation [11, 86].

4.2 Computational Experiments

In this section, multiple simulations are carried out to evaluate the performance of the proposed frequency-constrained EMS model. First, the general settings of the simulations and case studies are presented in Sections 4.2.1 and 4.2.2. Then, the performance of the proposed EMS model is evaluated from four different perspectives, namely regulation security in Section 4.2.3, operational performance in Section 4.2.4, frequency modeling accuracy in Section 4.2.5, and computational performance in Section 4.2.6.

4.2.1 General Settings

The performance of the proposed frequency-constrained EMS model is evaluated by simulating its implementation during one full day on the modified CIGRE benchmark system

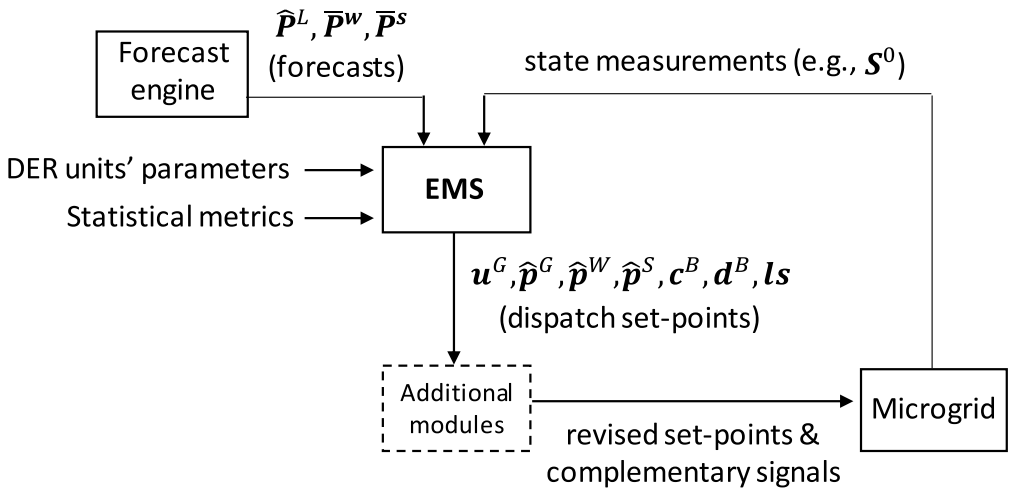

Figure 4.1: Proposed EMS architecture based on a MPC approach

presented in Section 3.4.4, with a larger 6153 kW peak demand, and a larger 2500kW/ 2500kWh lithium-ion battery. As in Chapter 3, simulations are performed using an MPC scheme with a 5min update rate, 24h horizon, and variable time resolution, with reserves being enforced only for the first 5h to reduce computational burden without significantly affecting total operating costs.

Three different EMS models are considered in the simulations for benchmarking purposes. The first model, referred hereinafter as EMS-1, corresponds to a conventional EMS similar to the ones presented in [22–27], for which frequency dynamics and battery degradation are not considered, and uncertain power variations are exclusively handled by a unique total reserve need, without any differentiation for forecast errors or regulation reserve needs. Note that this model closely resembles the B+DRT model studied in Section 3.4, with the only difference that the percentage-based capacity derating of generators and batteries is replaced by a simpler additional total reserve requirement. The second model, referred hereinafter as EMS-2, corresponds to the EMS model proposed in Chapter 3 (referred as R+DRP model in Section 3.4), which incorporates battery degradation and uses forecast error and regulation reserves for power fluctuation management, but does not consider frequency dynamics nor regulation-ramp reserves. The third model, referred hereinafter as EMS-3, corresponds to the frequency-constrained EMS model presented in Section 4.1.4, which considers frequency dynamics and battery degradation, and handles uncertain power variations through forecast error, regulation, and regulation-ramp reserves. In both EMS-2

and EMS-3 models, 4 even partitions with $\overline{S}_l = 0.2\ \forall l \in \mathcal{L}$ are used for representing battery degradation in a piecewise linear manner, as per (3.3). For the EMS-3 model, constraints (4.1), (4.5) and (4.13)-(4.16) are defined considering $\mathcal{H}^r = \{1, \ldots, 6\}$, as these are the dispatch time intervals with a time-step equal to the 5min MPC update rate, in which frequency dynamics and control play a key role. Note that constraint $\sum_{g \in G} u_{g,h} \geq 1\ \forall h \in \mathcal{H}$ is included in all three EMS models, which guarantees that at least one diesel generator is dispatched, so that there is always some synchronous inertia available in the system for instantaneous RoCoF damping.

The performance of the three EMS models is evaluated by retrieving the EMS's optimal dispatch set-points for the first dispatch time interval of each MPC iteration, and implementing such set-points in the dynamic model described in Section 2.4.4. Thus, transient simulations are performed iteratively for each dispatch time interval to obtain the evolution of the microgrid's frequency and DER units' instantaneous powers resulting from short-term power fluctuations. These results are then used to compute thermal generation costs, battery degradation costs, load shedding, renewable curtailment, and the amount of time that frequency deviation and RoCoF limits are violated. In accordance with IEEE's DER operating standard [86], all results and analyses related to the RoCoF are performed considering an averaging time window of 0.5s.

To ensure a fair comparison between the three EMS models, reserve needs are calibrated such that: (i) no load shedding resulting from forecast errors is obtained during the simulated day, and (ii) a specified frequency performance in the form of frequency and RoCoF limit compliance is achieved. The first condition is met by considering one standard deviation of the forecast errors when computing the reserve needs of the three EMS models, i.e, $\epsilon^{\chi} = 1$. The second condition is met by considering an additional total reserve requirement ΔRes in the EMS-1 model, by adjusting ϵ^{r} in the EMS-2 model, and by adjusting both ϵ^{r} and $\epsilon^{\partial r}$ in the EMS-3 model. As in Chapter 3, the standard deviations of forecast errors $\tilde{\sigma}^{\chi}_{h}$ are computed based on the values reported in [8] (see Table 3.1), and the standard deviations of short-term flucuations $\tilde{\sigma}^{r}_{h}$ and fluctuation-ramps $\tilde{\sigma}^{\partial r}_{h}$ are estimated using the 6-weeks measurements available from the KLFN microgrid [5] (see Tables 3.2 and 4.1).

A frequency deviation limit of $\overline{\Delta f} = \pm 1.2$Hz, RoCoF limit of $\overline{RoCoF} = \pm 0.5$Hz/s, and droop of $\kappa = 5\%$ for all DER units, are considered in the simulations, as per [86]. Frequency and voltage load sensitivities are obtained from the values reported in [95] for residential loads in North America, with $K^{PF} = 0.8$, and $K^{PV} = 1.5$. For RoCoF constraint (4.22), a frequency controller time delay of $T^{FC} = 0.1$s is considered, which results from the average response time observed for the battery and diesel generators in the transient simulations. For VFC, a voltage limit of $\overline{\Delta V} = 0.01$pu, and proportional gain of $K^{VFC} = 0.2$, are

Table 4.1: Standard deviations of short-term fluctuation-ramps [5]

Source	5min [%]	15min [%]	30min [%]	1h [%]
Wind	8.67	8.16	7.88	7.69
Solar	3.92	3.56	3.23	3.05
Demand	0.71	0.69	0.7	0.68

used based on [4]. Diesel engine governor's parameters are extracted from [2], which were slightly tuned to ensure stable system operation.

The battery degradation resulting from the simulations is computed using the same procedure and parameters described in Section 3.4.1, for which a detailed representation based on the rainflow cycle counting algorithm is considered. Such degradation is then multiplied by the battery's replacement cost to obtain the resulting battery degradation costs. Load shedding resulting from frequency regulation issues is valuated using a cost of 12 USD/kWh [96], while renewable curtailment is valuated using a cost of 0.07 USD/kWh, which is based on the wind and solar levelized costs of electricity reported in [97]. All simulations are performed on a PC with an Intel Core i7 3.20-GHz processor and 16 GB of RAM under a 64-bit Windows 10 operating system. The EMS optimal dispatch set-points are computed using the Julia programming language [91], JuMP package [92], and Gurobi solver [66]. Transient simulations are performed using MATLAB-Simulink [76].

4.2.2 Case Studies and Regulation Security Levels

The three EMS models are evaluated for two different case studies, which aim to illustrate possible practical frequency control configurations in the CIGRE microgrid. The first case study corresponds to a "Base" case, which considers the dynamic model presented in Section 2.4.4, but with the difference that the regulation capability of the VFC has been removed, i.e., $K^{VFC} = 0$ in Figure 2.8. The second case study corresponds to a "Detailed" case, for which the regulation capabilities of the VFC are incorporated, and the original linear percentage-based load shedding controller (see Figure 2.9) is replaced by a Under-Frequency Load Shedding (UFLS) scheme [87], whose frequency relay settings are illustrated in Figure 4.2. In both case studies, three different frequency regulation security levels are considered, which are based on the amount of time where the frequency deviation and RoCoF limits are violated, as follows:

- Low: for which frequency limit non-compliance should be around 300s.

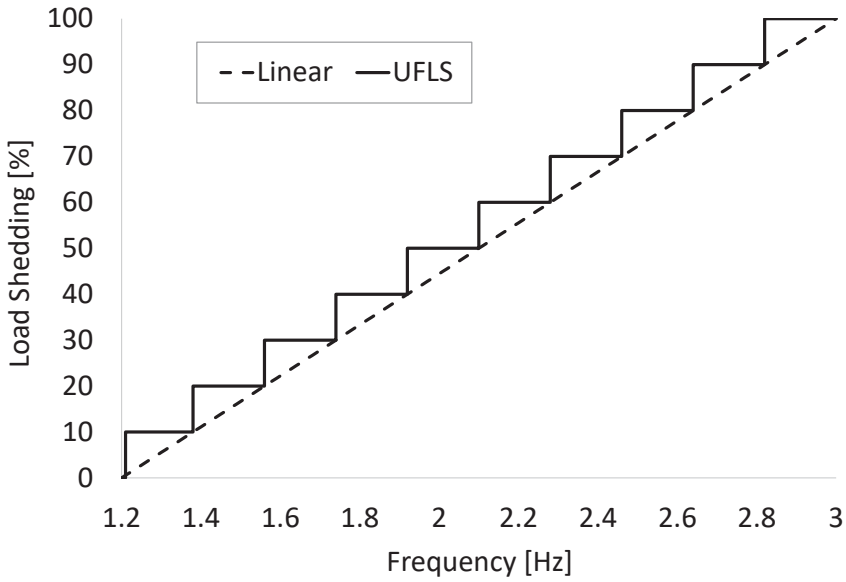

Figure 4.2: UFLS frequency relay setting relative to linear percentage-based load shedding.

- Medium: for which frequency limit non-compliance should be around 30s.
- High: for which Frequency-or-RoCoF (FoR) limit non-compliance should be around 30s, i.e., the total time that either frequency or RoCoF limits are violated is approximately half a minute.

4.2.3 Regulation Security

The capability to reach the Low, Medium, and High regulation security levels is evaluated for the three EMS models in this section. To accomplish this, the reserve requirements of the EMS models are gradually increased until either: (i) the desired frequency/FoR non-compliance is reached, or (ii) an infeasible optimization problem is obtained. The results of this test for the Base and Detailed cases are shown in Tables 4.2 and 4.3, respectively, which include the reserve sizing parameters used in the EMS models, the resulting non-compliance frequency/FoR values, and a flag indicating if the EMS was successful or not in reaching the desired regulation security level. From these results, it can be observed that the EMS-1 and EMS-2 models have difficulty reaching high regulation security levels, as these require large reserves that ultimately lead to infeasible optimization problems. In

Table 4.2: Security compliance results for Base case

Reg. sec.	EMS Model	Reserve sizing			Non-compl. [s]		Success flag
		ΔRes [MW]	ϵ^r	$\epsilon^{\partial r}$	Freq.	FoR	
Low	EMS-1	2.25	-	-	301	378	✓
	EMS-2	-	1.46	-	298	378	✓
	EMS-3	-	1.45	0.0	295	373	✓
Med.	EMS-1	2.59*	-	-	94*	162*	✗
	EMS-2	-	3.45	-	29	81	✓
	EMS-3	-	4.10	0.0	25	78	✓
High	EMS-1	-	-	-	-	-	✗
	EMS-2	-	4.20*	-	2*	46*	✗
	EMS-3	-	4.10	9.0	1	32	✓

*Desired frequency/FoR non-compliance could not be reached. Instead, the minimum achievable non-compliance is indicated.

contrast, the proposed frequency-constrained EMS model (EMS-3) can attain all regulation levels due to the more accurate modeling of short-term power fluctuations and frequency dynamics, which result in correctly balanced reserve requirements.

4.2.4 Operational Performance

In this section, the operational performance of the three EMS models is evaluated. The results of this test are shown in Tables 4.4 and 4.5 for the Base and Detailed cases, respectively, which include: (i) operating costs that consider thermal generation, battery degradation, and load shedding costs; (ii) total costs that include operating and renewable curtailment costs; and (iii) load shedding and renewable curtailment values. Note that the infeasible optimization results identified in Section 4.2.3 are omitted in these tables. From the results, it can be observed that the proposed frequency-constrained EMS model (EMS-3) also outperforms the EMS-1 and EMS-2 models in terms of operational performance, as the former exhibits reduced operating and total costs (2%-10% lower). Furthermore, note that the proposed EMS model tends to reduce the renewable curtailment in the system (up to 88% lower), which is reflected in the observed reduced costs.

It is also worth highlighting that a more thorough analysis of the results shows that there is a clear relationship between the desired regulation security level, the amount of

Table 4.3: Security compliance results for Detailed case

Reg. sec.	EMS Model	Reserve sizing			Non-compl. [s]		Success flag
		ΔRes [MW]	ϵ^r	$\epsilon^{\partial r}$	Freq.	FoR	
Low	EMS-1	2.00	-	-	302	410	✓
	EMS-2	-	0.54	-	298	405	✓
	EMS-3	-	1.00	0.0	295	399	✓
Med.	EMS-1	2.59*	-	-	62*	144*	✗
	EMS-2	-	3.03	-	30	96	✓
	EMS-3	-	3.33	0.0	30	96	✓
High	EMS-1	-	-	-	-	-	✗
	EMS-2	-	4.20*	-	0*	47*	✗
	EMS-3	-	3.33	9.1	0	32	✓

*Desired frequency/FoR non-compliance could not be reached. Instead, the minimum achievable non-compliance is indicated.

renewable/thermal generation injected into the system, and the number of thermal generators that are ON during the day. This relationship can be observed by comparing Figures 4.3, 4.4, and 4.5, where the dispatch profiles for the different regulation security levels and EMS models are illustrated, including renewable generation (RG), thermal generation (G1-G5), demand (D), battery discharge (BD), and battery charge (BC). Note that as the regulation security level increases from Low (Figure 4.3) to Medium (Figure 4.4), a significant amount of renewable generation is curtailed and replaced by thermal generation, which as discussed in Section 3.4, is the result of strategically using renewable curtailment to reduce the system's regulation/reserve needs. Furthermore, observe that as the regulation security level increases from Medium (Figure 4.4) to High (Figure 4.5), more thermal generators are turned ON during the day, such that a sufficient amount of synchronous inertia is available for RoCoF damping.

4.2.5 Frequency Modeling Accuracy

As previously discussed, one of the major advantages of proposed EMS model lies in the explicit modeling of frequency dynamics. Thus, to further validate the observed results, the accuracy of the QSS frequency equations (4.13)-(4.16), and RoCoF equations (4.20)-(4.22) used in the proposed EMS model were also tested. For this test, the instantaneous frequency and RoCoF obtained by transient simulations were compared to the ones estimated

Table 4.4: Operational results for the Base case

Reg. sec.	EMS model	Oper. cost [kUSD]	Total cost [kUSD]	Load shed. [kWh]	Ren. curt. [MWh]
Low	EMS-1	9.14	9.19	7.6	0.68
	EMS-2	9.03	9.08	7.1	0.72
	EMS-3	8.60	8.60	9.7	0.08
Med.	EMS-2	10.51	11.02	1.3	7.40
	EMS-3	9.66	10.01	0.5	4.98
High	EMS-3	11.18	11.97	0.1	11.34

Table 4.5: Operational results for the Detailed case

Reg. sec.	EMS model	Oper. cost [kUSD]	Total cost [kUSD]	Load shed. [kWh]	Ren. curt. [MWh]
Low	EMS-1	11.10	11.13	180.3	0.37
	EMS-2	10.18	10.18	130.1	0.05
	EMS-3	9.99	9.99	134.5	0.06
Med.	EMS-2	10.50	10.89	40.1	5.66
	EMS-3	9.67	9.89	39.6	3.22
High	EMS-3	11.24	12.04	6.2	11.47

using (4.13)-(4.16) and (4.20)-(4.22). Figure 4.6 illustrates the actual (Act.) frequency excursions obtained by the transient simulations, and the estimated (Est.) frequency excursions using QSS frequency equations (4.13)-(4.16) for a particular simulation case. Note that both actual and estimated curves exhibit a close resemblance, with more significant differences being observed in the presence of abrupt frequency jumps.

The close resemblance between actual and estimated values in Figure 4.6 was also observed in the rest of the simulation cases. This is illustrated in Table 4.6, in which the Mean Absolute Error (MAE) for all simulations cases is indicated, from where it can be concluded that the proposed EMS provides an accurate representation of the actual frequency dynamics of an isolated microgrid during daily operations.

4.2.6 Computational Performance

The computational performance of the three EMS models is evaluated here. This is a relevant aspect to assess, as computation times for the EMS optimization model need to be

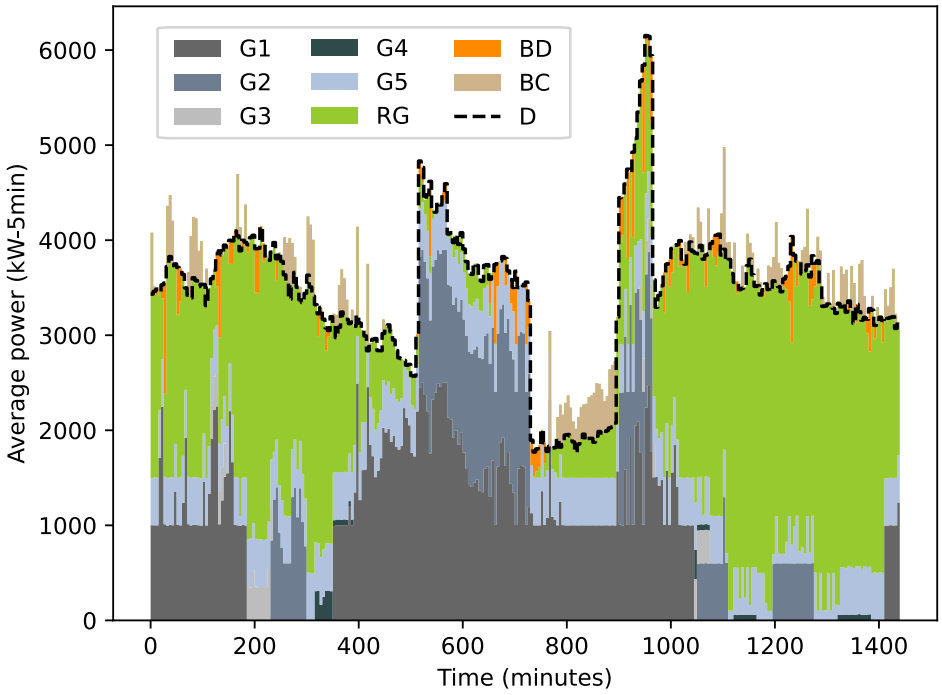

Figure 4.3: Dispatch results for EMS-1 model under a Low regulation security level.

significantly lower than the 5min MPC update rate for near real-time applications [22]. For this test, the computation times required to solve the optimization problems were recorded for each MPC iteration, yielding a total of 288 measurements for one full day simulation. The resulting average and maximum computation times are presented in Table 4.7, where it can be observed that all three EMS models exhibit low computation times in the order of seconds, making them suitable for practical applications. This observed computational efficiency stems from the fact that all three EMS models are linear, and thus result in computationally efficient MILP optimization problems. Therefore, another relevant contribution of the EMS model proposed in this chapter (EMS-3) is that it incorporates the impact of frequency dynamics on operations, while keeping a computational performance on par with the one observed for the simpler EMS-1 and EMS-2 models.

In summary, the proposed frequency-constrained EMS model outperforms existing EMS models, achieving reduced operational costs and reaching a wider range of frequency regulation security levels. Moreover, this overall better performance is achieved while keeping computational tractability suitable for near real-time practical applications.

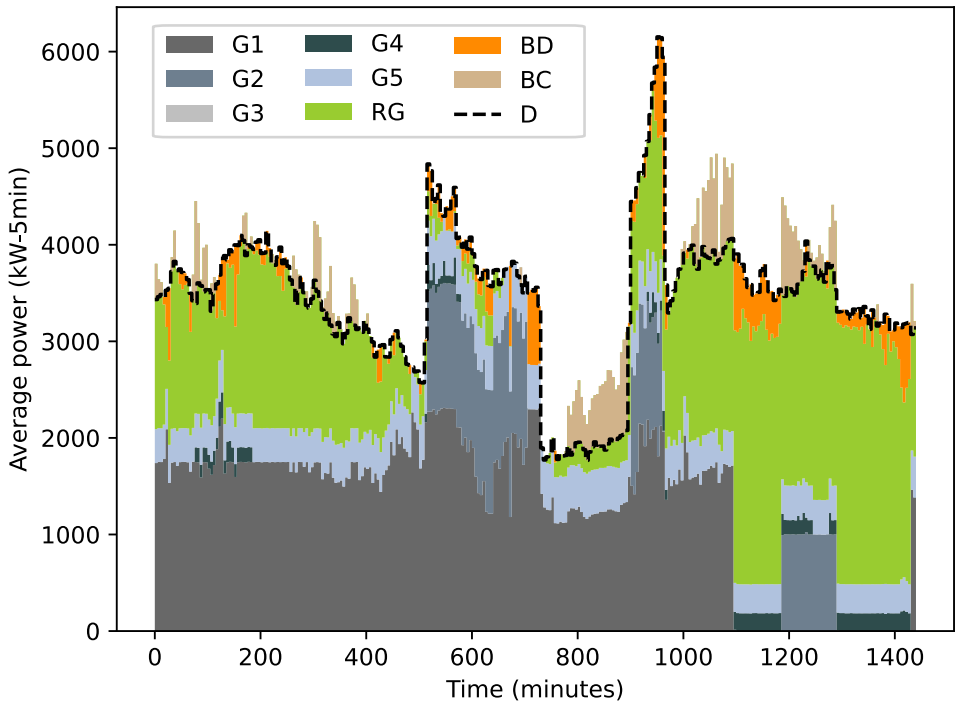

Figure 4.4: Dispatch results for EMS-2 model under a Medium regulation security level.

4.3 Summary

Short-term power fluctuations stemming from renewable generation can severely degrade the frequency regulation performance of isolated microgrids, as these have low inertia and, more commonly nowadays, significant renewable energy integration. Motivated by this, the present chapter developed a practical frequency-constrained EMS that incorporates short-term fluctuations and their impact on frequency regulation. The frequency-constrained EMS presented in this chapter was evaluated and compared to previously proposed EMS models on a realistic test system using detailed frequency transient models, showing that it allows reducing total operating costs for a given security level, and achieving higher frequency regulation security levels in line with modern operating standards for microgrids. Furthermore, due to the use of alternative linear equations to describe frequency dynamics, the proposed frequency-constrained EMS model can be solved with sufficiently low computation times, making it suitable for near real-time practical applications. The main content of this chapter has been published in [98].

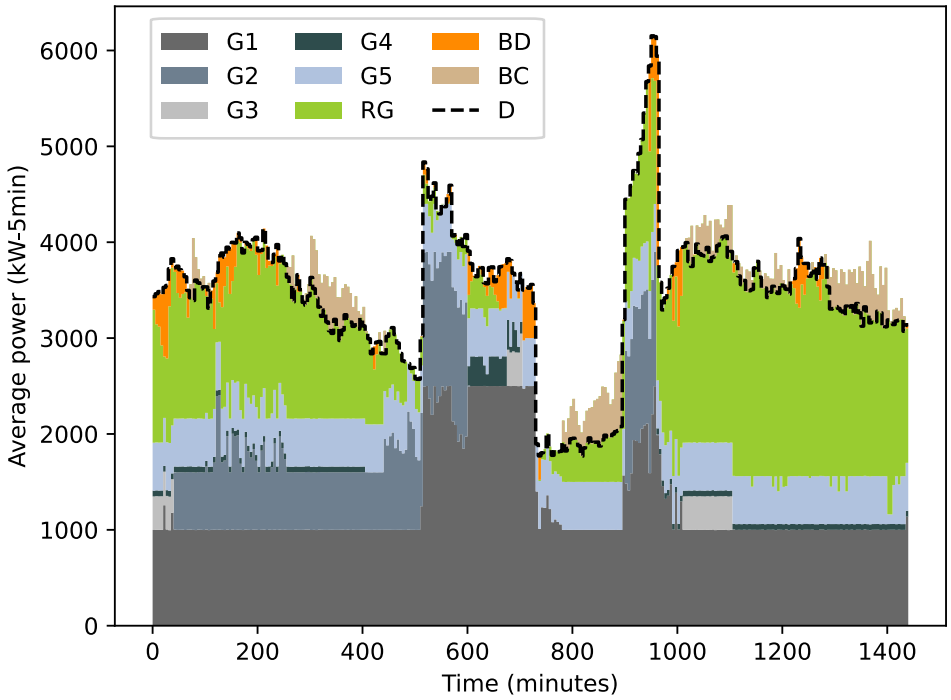

Figure 4.5: Dispatch results for EMS-3 model under a High regulation security level.

Table 4.6: Frequency and RoCoF Mean Absolute Errors

Reg. sec.	EMS model	Freq. MAE [Hz]		RoCoF MAE [Hz/s]	
		Base	Detailed	Base	Detailed
Low	EMS-1	0.02	0.03	0.04	0.04
	EMS-2	0.01	0.03	0.05	0.04
	EMS-3	0.02	0.03	0.04	0.05
Med.	EMS-2	0.01	0.02	0.02	0.02
	EMS-3	0.01	0.02	0.01	0.02
High	EMS-3	0.01	0.01	0.01	0.01

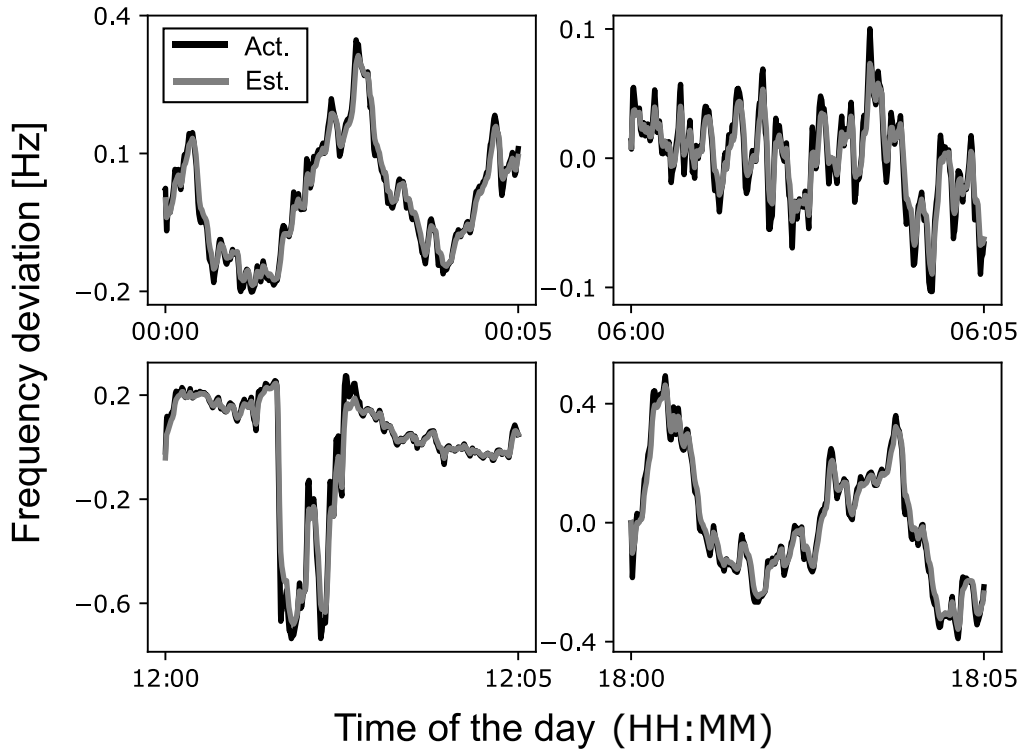

Figure 4.6: Comparison of frequency excursions during different times of the day for the Base case using the proposed EMS (EMS-3) under a High regulation security level.

Table 4.7: Computation times per MPC iteration

Reg. sec.	EMS Model	Average time [s]		Maximum time [s]	
		Base	Detailed	Base	Detailed
Low	EMS-1	0.6	0.6	16.9	17.1
	EMS-2	2.0	0.9	21.5	22.2
	EMS-3	1.2	1.0	21.9	24.2
Med.	EMS-2	6.5	5.1	56.7	32.5
	EMS-3	4.5	3.1	27.1	30.7
High	EMS-3	2.9	2.8	18.9	22.7

Chapter 5

Integrating Thermostatically Controlled Loads in Microgrid Operation

To address the issue of a potential degraded frequency regulation performance in isolated microgrids, Chapter 4 presented an EMS integrating short-term fluctuations and their impact on frequency regulation, in which an strategic use of thermal generators and batteries was employed to ensure an economic and reliable system operation. However, this EMS neglects the additional flexibility stemming from other currently available technologies, such as modern load controls. Within these, the aggregate control of TCLs are of particular interest for isolated microgrids, as TCLs comprise a significant share of the total residential demand [17], and can counterbalance short-term power imbalances while remaining non-disruptive to the end-user [18]. Hence, the present chapter studies the integration of TCLs within microgrid operations through the use of computationally tractable aggregate models, focusing on the role that TCLs can play to manage second-to-second power fluctuations and their corresponding impact on frequency regulation. In particular, two computationally efficient and accurate aggregate TCL models are developed:

1. A virtual battery model representing the aggregate flexibility of TCLs, for which relevant detailed TCL thermal dynamics are incorporated, such as solar irradiance heat gains and wall/floor heat transfers [61, 82, 83].

2. A frequency transient model representing the aggregate dynamics of a TCL collection, for which relevant practical challenges are integrated, such as communication delays [99], and the presence of model uncertainty and time-variability [21].

These aggregate TCL models are then used to design a practical EMS integrating TCL flexibility, and study the impact of TCL integration on microgrid operation and frequency control. Computational experiments using detailed frequency transient and thermal dynamic models are presented, demonstrating the accuracy of the proposed aggregate TCL models, as well as the economic and reliability benefits resulting from using these aggregate models to integrate TCLs in microgrid operations.

The chapter is organized as follows: In Section 5.1, the design of the proposed aggregate TCL models is discussed, for which detailed TCL thermal dynamics and practical challenges are considered. Then, based on the models developed in the previous section, a novel EMS integrating TCL flexibility is proposed in Section 5.2. Computational experiments and associated results are presented in Section 5.2, showcasing the benefits of integrating TCLs in microgrid operations through the use of proper aggregate TCL models. Finally, the main contributions and conclusions of this chapter are summarized in Section 5.3.

5.1 Aggregate Modeling of Thermostatically Controlled Loads

In this section, models needed for the implementation of an aggregate TCL control are discussed. First, a novel decoupled thermal model is presented in Section 5.1.1, which is used in Section 5.1.2 to develop virtual battery model capable of accurately describing the aggregate flexibility of a TCL collection. Then, practical challenges found in aggregate TCL control implementations, and how these can be modeled, are discussed in Section 5.1.3. Finally, based on the previous modeling techniques, a new transient model for characterizing the frequency dynamics of an aggregate TCL control is developed in Section 5.1.4.

5.1.1 Decoupled Thermal Model

As previously discussed in Section 2.3.2, one of the main drawbacks of the third-order model (2.13) is its increased mathematical complexity, which prevents its direct integration in virtual battery models with a large TCL population. Thus, to tackle this issue, a decoupled thermal model is proposed here, which captures the high-modeling accuracy of the original third-order model, while maintaining a low mathematical complexity suitable for virtual battery model design. The proposed decoupled thermal model is based on (2.13), for which

a series of simplifications can be made based on the following properties commonly found in practical settings:

1. Inner household thermal dynamics operate at a relatively fast timescale in the order of seconds to minutes, whereas wall and floor thermal dynamics operate at a slower timescale in the order of minutes to hours.
2. Air conditioners automatically regulate the inner household temperature to match the thermostat's setpoint $\theta^{I,SP}$, resulting in $\theta^{I} \approx \theta^{I,SP}$.
3. The ground temperature θ^{G} remains relatively constant during the day.

These allow characterizing wall/floor thermal dynamics (2.13b) and (2.13c), which operate at a slower timescale DT, in the following decoupled manner:

$$C^{W} \frac{d\theta^{W}(t)}{dt} \approx q^{W} + \frac{\theta^{A} + \theta^{I,SP} - 2\theta^{W}(t)}{R^{W}/2} \tag{5.1a}$$

$$0 \approx \frac{\theta^{G} + \theta^{I,SP} - 2\theta^{F}(t)}{R^{F}/2} \tag{5.1b}$$

which results in the following equations for characterizing the wall and floor temperature evolution over time:

$$\theta^{W}(t) \approx \theta^{W,SS} + \left(\theta^{W,0} - \theta^{W,SS}\right) \exp\left(-\alpha^{W} t\right) \tag{5.2a}$$

$$\theta^{F}(t) \approx \theta^{F,SS} = \left(\theta^{G} + \theta^{I,SP}\right)/2 \tag{5.2b}$$

where $\theta^{W,SS} = (\theta^{A} + \theta^{I,SP})/2 + q^{W} R^{W}/4$ is the steady-state wall temperature; $\theta^{W,0}$ is the initial wall temperature; $\theta^{F,SS}$ is the steady-state floor temperature; and $\alpha^{W} = 4/(R^{W} C^{W})$.

Inner household thermal dynamics (2.13a), on the other hand, operate at a faster timescale, for which it can be assumed that wall and floor temperatures remain relatively constant, resulting in the following decoupled representation:

$$C^{I} \frac{d\theta^{I}(t)}{dt} \approx q^{TCL}(t) + q^{EQ} - \frac{\theta^{I}(t)}{R^{EQ}} \tag{5.3a}$$

$$q^{EQ} = q^{C} + \frac{\theta^{A}}{R^{C}} + \frac{\theta^{W,DT}}{R^{W}/2} + \frac{\theta^{F,SS}}{R^{F}/2} \tag{5.3b}$$

$$\frac{1}{R^{EQ}} = \frac{1}{R^{C}} + \frac{1}{R^{W}/2} + \frac{1}{R^{F}/2} \tag{5.3c}$$

$$\theta^{W,DT} = \theta^{W,SS} + \frac{\left(\theta^{W,0} - \theta^{W,SS}\right)}{\alpha^{W} DT}\left[1 - \exp\left(\alpha^{W} DT\right)\right] \tag{5.3d}$$

where q^{EQ} and R^{EQ} are the equivalent heat gain and thermal resistance, respectively, and $\theta^{W,DT}$ is the average wall temperature during the DT timescale considered for the slower wall and floor dynamics. Thus, the following equation can be used to describe the inner household temperature:

$$\theta^{I}(t) \approx q^{EQ} R^{EQ} + \left(\theta^{I,0} - q^{EQ} R^{EQ}\right) \exp(-\alpha^{I} t) \tag{5.4}$$

where $\theta^{I,0}$ is the initial inner household temperature, and $\alpha^{I} = 1/(C^{I} R^{EQ})$.

Note that the proposed decoupled model (5.1)-(5.4) captures the dynamics of the original third-order model (2.13) with reduced complexity, as the differential equations are decoupled in this case. This not only translates into an improved computational performance, but also serves as a basis for deriving a practical virtual battery model that incorporates solar heat gains and wall/floor thermal dynamics, as discussed next.

5.1.2 Virtual Battery Model

A new virtual battery model is derived here using the decoupled thermal model presented in Section 5.1.1. The proposed virtual battery model is based on [6], but adapted to incorporate the additional thermal dynamics of detailed high-order household thermal models.

As a first step, (5.3a) has to be rewritten in terms of TCL electric consumption. For this, the following continuous TCL power model is assumed:

$$q^{TCL}(t) = \eta^{TCL} p^{TCL}(t) = \eta^{TCL} \left[p^{TCL,SS} + \Delta p^{TCL}(t)\right] \tag{5.5a}$$

$$0 \leq p^{TCL}(t) \leq \overline{P}^{TCL} \tag{5.5b}$$

where η^{TCL} is the coefficient of performance; p^{TCL} is the TCL electric power consumption, which has been split into steady-state baseline consumption $p^{TCL,SS}$ and deviations from it Δp^{TCL}; and $\overline{P}^{TCL}$ is the TCL rated electrical power. Thus, replacing (5.5a) in (5.3a), the following thermal-electric differential equation is obtained:

$$C^{I} \frac{d\theta^{I}(t)}{dt} = \eta^{TCL} \left[p^{TCL,SS} + \Delta p^{TCL}(t)\right] + q^{EQ} - \frac{\theta^{I}(t)}{R^{EQ}} \tag{5.6a}$$

$$p^{TCL,SS} = \frac{1}{\eta^{TCL}} \left(\frac{\theta^{I,SP}}{R^{EQ}} - q^{EQ}\right) \tag{5.6b}$$

where the TCL baseline consumption (5.6b) is obtained by assuming a steady-state condition with no TCL power deviations, i.e., $d\theta^{I}/dt = \Delta p^{TCL} = 0$ and $\theta^{I} = \theta^{I,SP}$.

Defining the auxiliary variable $\Theta = C^I \left(\theta^I - \theta^{I,SP}\right)/\eta^{TCL}$, and re-arraging (5.6), one has that:

$$\frac{d\Theta_n(t)}{dt} = -\gamma_n^{TCL}\,\Theta_n(t) + \Delta p_n^{TCL}(t) \tag{5.7}$$

where the subsubscript n has been added for representing a particular TCL in the set of TCLs $\mathcal{N} = \{1, \ldots, N\}$, and $\gamma_n^{TCL} = (C_n^I\, R_n^{EQ})^{-1}$. Thus, based on (5.7), the following virtual battery model can be defined:

$$\frac{de^V(t)}{dt} = -\gamma^V e^V(t) - d^V(t) \tag{5.8a}$$

$$-E^V \leq e^V(t) \leq E^V, \quad -P^{V,C} \leq d^V(t) \leq P^{V,D} \tag{5.8b}$$

e^V is the virtual battery's stored energy, which can be linked to Θ in (5.7), and thus to the temperature offset from the thermostat's setpoint $\theta^I - \theta^{I,SP}$; d^V is the virtual battery's discharging power, which can be linked to the deviation from the baseline consumption Δp^{TCL} in (5.7); and γ^V is the virtual battery's self-discharging rate. Maximum capacity limits are also considered in this virtual battery model, namely, maximum discharging power $P^{V,D}$, maximum charging charging power $P^{V,C}$, and maximum stored energy E^V. While these capacity limits cannot be directly computed, analytical upper/lower bounds can instead be derived, so that:

$$\underline{P}^{V,D} \leq P^{V,D} \leq \overline{P}^{V,D} \tag{5.9a}$$

$$\underline{P}^{V,C} \leq P^{V,C} \leq \overline{P}^{V,C} \tag{5.9b}$$

$$\underline{E}^V \leq E^V \leq \overline{E}^V \tag{5.9c}$$

The equations necessary to compute these bounds are discussed next, based on derivations presented in Appendix B.

Upper bounds $\overline{P}^{V,D}$, $\overline{P}^{V,C}$, and $\overline{E}^V$ can be determined by overestimating the flexibility available from the TCL collection $\mathcal{N}$, resulting in the following equations:

$$\overline{P}^{V,D} = \sum_{n\in\mathcal{N}} p_n^{TCL,SS} \tag{5.10a}$$

$$\overline{P}^{V,C} = \sum_{n\in\mathcal{N}} \left(\overline{P}_n^{TCL} - p_n^{TCL,SS}\right) \tag{5.10b}$$

$$\overline{E}^V = \sum_{n\in\mathcal{N}} \left(1 + \frac{|\gamma_n^{TCL} - \gamma^V|}{\gamma^V}\right) \frac{C^I \Delta\theta_n^{TCL}}{\eta_n^{TCL}} \tag{5.10c}$$

where $\Delta\theta_n^{TCL}$ is the TCL's n temperature deadband. On the other hand, lower bounds can be determined by underestimating the flexibility of the TCL collection. Note, however, that in this case a range of possible lower bounds are available. In general, any $\underline{P}^{V,D}$, $\underline{P}^{V,C}$, and $\underline{E}^{V}$ satisfying the following expressions is a valid underestimator of the true virtual battery capacity limits:

$$\beta_n \, \underline{P}^{V,D} \leq p_n^{TCL,SS} \tag{5.11a}$$

$$\beta_n \, \underline{P}^{V,C} \leq \overline{P}_n^{TCL} - p_n^{TCL,SS} \tag{5.11b}$$

$$\beta_n \, \underline{E}^{V} \leq \frac{C^I \Delta\theta_n^{TCL}}{\eta_n^{TCL}} \left(1 + \frac{|\gamma^V - \gamma_n^{TCL}|}{\gamma_n^{TCL}}\right)^{-1} \tag{5.11c}$$

where $\beta_n \geq 0$ is a parameter indicating the share of the total regulation provided by each TCL, with $\sum_{n\in\mathcal{N}} \beta_n = 1$. For example, setting $\beta_n = p_n^{TCL,SS} / \sum_{n\in\mathcal{N}} p_n^{TCL,SS}$, which maximizes $\underline{P}^{V,D}$, results in:

$$\underline{P}^{V,D} = \sum_{n\in\mathcal{N}} p_n^{TCL,SS} \tag{5.12a}$$

$$\underline{P}^{V,C} = \tilde{P}^{V,D} \min_{n\in\mathcal{N}} \left\{ \frac{\overline{P}_n^{TCL} - p_n^{TCL,SS}}{p_n^{TCL,SS}} \right\} \tag{5.12b}$$

$$\underline{E}^{V} = \tilde{P}^{V,D} \min_{n\in\mathcal{N}} \left\{ \frac{C^I \Delta\theta_n^{TCL}}{\eta_n^{TCL} \, p_n^{TCL,SS}} \left(1 + \frac{|\gamma^V - \gamma_n^{TCL}|}{\gamma_n^{TCL}}\right)^{-1} \right\} \tag{5.12c}$$

which are valid underestimators of the exact virtual battery capacity limits. Note that (5.10) and (5.11), while similar to the equations in Theorems 5 and 6 of [6], differ in how γ_n^{TCL} and $p_n^{TCL,SS}$ are calculated, as these now incorporate the more detailed thermal dynamics of high-order household models.

5.1.3 Practical Challenges

Another relevant issue to consider for the implementation of an aggregate TCL control are its inherent practical challenges, as these can hinder its flexibility and regulation capability. Thus, in what follows, two relevant challenges previously identified in real-life applications are discussed.

The first challenge relates to the time-variability and uncertainty present in virtual battery models, which as discussed in [21], stems from their dependence in external factors

such as ambient temperature. This applies also to the proposed virtual battery model (5.8), as its energy/power capacity limits $P^{V,D}$, $P^{V,C}$, and E^{V} are dependant on solar radiation heat gains q^{C} and q^{W}, and external temperatures θ^{A} and θ^{G} (see Sections 5.1.1 and 5.1.2), all of which vary over the day and are subject to imperfect forecasts. Thus, to model these additional effects, subscripts for time-intervals $h \in \mathcal{H}$ and Monte Carlo (MC) scenarios $i \in \mathcal{I}$ are considered for the virtual battery capacity limits in (5.9), yielding the following updated conservative limits:

$$\underline{P}_{h}^{V,D,MC} = \min_{i \in \mathcal{I}} \underline{P}_{h}^{V,D}(\xi_i) \tag{5.13a}$$

$$\underline{P}_{h}^{V,C,MC} = \min_{i \in \mathcal{I}} \underline{P}_{h}^{V,C}(\xi_i) \tag{5.13b}$$

$$\underline{E}_{h}^{V,MC} = \min_{i \in \mathcal{I}} \underline{E}_{h}^{V}(\xi_i) \tag{5.13c}$$

where ξ_i denotes the sample realization of scenario i, for which different values of $q^{C}(\xi_i)$, $q^{W}(\xi_i)$, $\theta^{A}(\xi_i)$, and $\theta^{G}(\xi_i)$ are generated and then used to estimate the corresponding virtual battery capacity limits. Note that (5.13) uses a conservative minimum approach to ensure a reliable model. Furthermore, observe that capacity limits in (5.13) are assumed to remain constant for time-interval h, as external temperatures have relatively slow dynamics (in order of minutes to hours), and second-to-second fluctuations in solar radiation are filtered by the household's wall and internal thermal capacitances.

A second challenge relates to communication delays, as these directly impact the response time of aggregate TCL control implementations. As reported in [99], communication delays can reach values of up to 1s in real-life applications, making their incorporation in frequency dynamic models necessary, since the timescale of these dynamics are in the order of milliseconds to seconds in isolated microgrids. To model this effect, an additional communication delay block is considered in the proposed frequency dynamic model presented next.

5.1.4 Frequency Dynamic Model

Based on the virtual battery model and practical challenges discussed in Sections 5.1.2 and 5.1.3, a novel transient model for characterizing the frequency dynamics of an aggregate TCL control is developed here. The proposed model is presented in Figure 5.1, which considers frequency deviation measurements Δf and virtual battery discharge power output p^{V}, as well as a Virtual Battery Controller (VBC) and an Actuation Mechanism, which are described next.

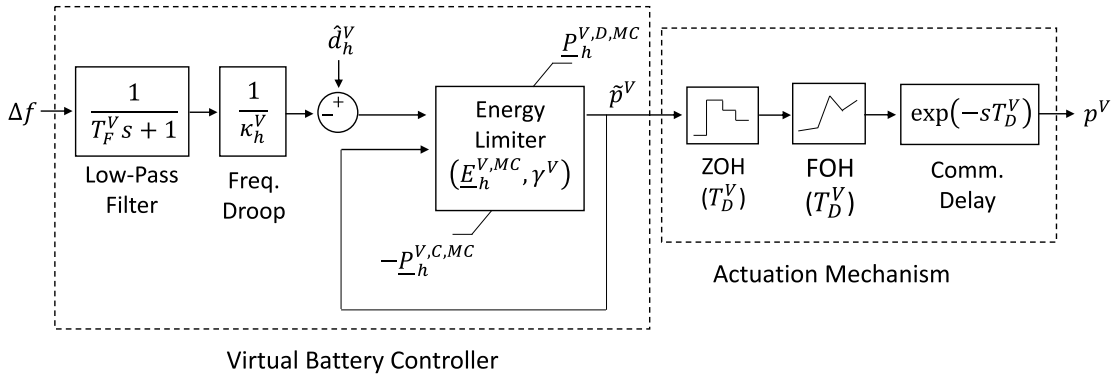

Figure 5.1: Block diagram of aggregate TCL control model.

The VBC block is composed of: (i) an Energy Limiter block, in which virtual battery state-of-charge (5.8a) and capacity limits (5.13) are integrated; (ii) an external discharging power set-point $\hat{d}_h^V$; (iii) a Frequency-Droop block with droop constant κ_h^V; and (iv) a Low-Pass Filter with time constant T_F^V. The Actuation Mechanism represents the change in dynamics resulting from implementing the virtual battery regulation instruction $\tilde{p}^V$ across the different TCLs, and is composed of: (i) a Zero-Order Hold (ZOH) block with sampling period T_D^V, which is used to represent the inherent discrete-time nature of the control, as residential TCLs typically operate using a ON/OFF switching logic and have short cycling constraints [6, 77, 80]; (ii) a First-Order Hold (FOH) block, which is used to represent that ON/OFF switching signals are intentionally spread across a T_D^V time interval to prevent large step-wise power changes in the system; and (iii) a Communication Delay block with time delay T_D^V (see Section 5.1.3). Note that the parameter T_D^V is intentionally chosen to be consistent in the previous three blocks, so that a coordinated system response is ensured, as illustrated in Figure 5.2.

5.2 Energy Management System Model

In this section, a novel microgrid EMS embedding the flexibility of an aggregate TCL control is designed. First, the optimization model considered for the EMS is presented, which builds on the models previously developed in Section 5.1. Then, the general architecture needed for implementing the aggregate TCL control and EMS is discussed.

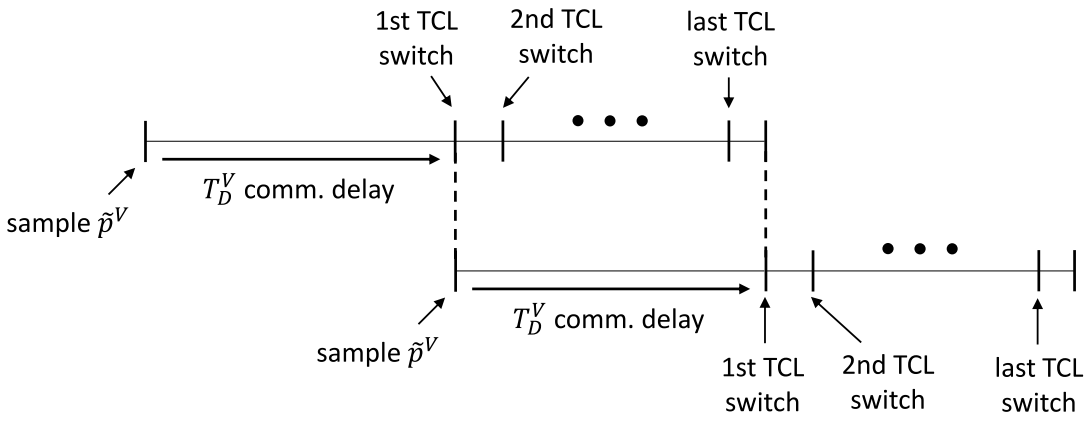

Figure 5.2: Coordinated TCL actuation mechanism with communication delays.

5.2.1 Optimization Model

As previously discussed, modern EMS models for isolated microgrids require the incorporation of frequency dynamics in their decisions-making process, since these systems are particularly prone to poor frequency regulation performance. Thus, the proposed EMS model builds on the frequency-constrained EMS model described in Chapter 4, which is adapted here to integrate the flexibility of an aggregate TCL control. The specific changes made to the the original frequency-constrained EMS model are described next.

Fist, the constraints associated to the virtual battery model (5.8) are defined $\forall h \in \mathcal{H}$ as follows:

$$\hat{e}_h^V = \left(1 - \gamma^V \Delta T_h\right) \hat{e}_{h-1}^V - \Delta T_h \, \hat{d}_h^V + \Delta \hat{e}_h^V \tag{5.14a}$$

$$-\mu \, \underline{E}_h^{V,MC} \leq \hat{e}_h^V \leq \mu \, \underline{E}_h^{V,MC} \tag{5.14b}$$

$$\hat{d}_h^V + \Delta p_h^{V,\chi,\uparrow} + \Delta p_h^{V,r,\uparrow} \leq \underline{P}_h^{V,D,MC} \tag{5.14c}$$

$$\hat{d}_h^V - \Delta p_h^{V,\chi,\downarrow} - \Delta p_h^{V,r,\downarrow} \geq -\underline{P}_h^{V,C,MC} \tag{5.14d}$$

where ΔT_h is the time step of dispatch time-interval h; $\hat{e}_h^V$ is the virtual battery's stored energy at the end time-interval h; $\hat{d}_h^V$ is the discharge power set-point for the VBC during time-interval h (see Figure 5.1); $\Delta p_h^{V,\chi,\uparrow}$ and $\Delta p_h^{V,\chi,\downarrow}$ are the upward and downward forecast error reserves provided by the virtual battery, respectively; $\Delta p_h^{V,r,\uparrow}$ and $\Delta p_h^{V,r,\downarrow}$ are the upward and downward regulation reserves provided by the virtual battery, respectively; and $\mu \in [0, 1]$ is a safety derating factor to prevent the repeated triggering of the Energy

Limiter block in the VBC (see Figure 5.1). Note that (5.14) also includes the decision variable $\Delta\hat{e}_h^V$, which represents the expected increase in the virtual battery's stored energy due to reserve provision, defined as follows:

$$\Delta\hat{e}_h^V = \frac{\varphi_h^\chi}{2}\Delta T_h\left(\Delta p_h^{V,\chi,\downarrow} - \Delta p_h^{V,\chi,\uparrow}\right) + \frac{\varphi_h^r}{2}\Delta T_h\left(\Delta p_h^{V,r,\downarrow} - \Delta p_h^{V,r,\uparrow}\right) \tag{5.15}$$

where φ_h^χ and φ_h^r are the ERU parameters for forecast error and regulation reserves, respectively (see Sections 3.3.1 and 4.1.2).

To ensure enough energy is saved in the virtual battery for reserve provision, the following additional conservative constraints are also considered $\forall h \in \mathcal{H}$:

$$\left(1-\gamma^V\Delta T_h\right)\hat{e}_{h-1}^V - \Delta T_h\left(\hat{d}_h^V - \Delta p_h^{V,\chi,\downarrow} - \frac{1}{2}\Delta p_h^{V,r,\downarrow}\right) \leq \mu\,\underline{E}_h^{V,MC} \tag{5.16a}$$

$$\left(1-\gamma^V\Delta T_h\right)\hat{e}_{h-1}^V - \Delta T_h\left(\hat{d}_h^V + \Delta p_h^{V,\chi,\uparrow} + \frac{1}{2}\Delta p_h^{V,r,\uparrow}\right) \geq -\mu\,\underline{E}_h^{V,MC} \tag{5.16b}$$

Furthermore, an energy neutrality constraint for the virtual battery is included, as follows:

$$\hat{e}_H^V = E^{V,0} \tag{5.17}$$

where $E^{V,0}$ is the initial stored energy in the virtual battery, and H is the last time index of the set of time intervals $\mathcal{H}$.

Based on the frequency dynamic controller presented in Section 5.1.4, constraints for characterizing the maximum deliverable short-term regulation of the virtual battery can be also defined $\forall h \in \mathcal{H}$ as follows (see Figure 5.1):

$$\Delta p_h^{V,r,\uparrow} \leq \frac{\overline{\Delta f}}{f_0}\frac{1}{\kappa_h^V} \tag{5.18a}$$

$$\Delta p_h^{V,r,\downarrow} \leq \frac{\overline{\Delta f}}{f_0}\frac{1}{\kappa_h^V} \tag{5.18b}$$

$$\kappa_h^V = \overline{\kappa}^V \Big/ \min\left\{\underline{P}_h^{V,D,MC}, \underline{P}_h^{V,C,MC}\right\} \tag{5.18c}$$

where f_0 is the microgrid's nominal frequency, and $\overline{\Delta f}$ is the maximum frequency deviation limit imposed by DER operating standards. Note that in (5.18), the frequency-droop constant κ_h^V is adjusted based on the virtual battery's power capacity limits for dispatch time-interval h, where $\overline{\kappa}^V$ is a fixed droop value in line with modern operating DER standards [86].

System power and reserve balances (3.28) and (4.4)–(4.6) are also modified to incorporate the additional flexibility stemming from an aggregate TCL control. In the case of power balance (3.28), one now has the following updated constraint $\forall h \in \mathcal{H}$:

$$\sum_{b\in\mathcal{B}}\sum_{l\in\mathcal{L}}\left(d^{B}_{b,l,h}-c^{B}_{b,l,h}\right)+\sum_{g\in\mathcal{G}}\hat{p}^{G}_{g,h}+\hat{d}^{V}_{h}=\hat{P}^{L}_{h}-\hat{p}^{W}_{h}-\hat{p}^{S}_{h}-ls_{h} \tag{5.19}$$

Similarly, for forecast error reserve balance (4.4), the following constraint is instead used $\forall h \in \mathcal{H}$:

$$\zeta^{\chi}_{h}=\sum_{g\in\mathcal{G}}\Delta p^{G,\chi,\uparrow}_{g,h}+\sum_{b\in\mathcal{B}}\sum_{l\in\mathcal{L}}\left(\Delta p^{B,D,\chi,\uparrow}_{b,l,h}+\Delta p^{B,C,\chi,\uparrow}_{b,l,h}\right)+\Delta p^{V,\chi,\uparrow}_{h} \tag{5.20a}$$

$$\zeta^{\chi}_{h}=\sum_{g\in\mathcal{G}}\Delta p^{G,\chi,\downarrow}_{g,h}+\sum_{b\in\mathcal{B}}\sum_{l\in\mathcal{L}}\left(\Delta p^{B,D,\chi,\downarrow}_{b,l,h}+\Delta p^{B,C,\chi,\downarrow}_{b,l,h}\right)+\Delta p^{V,\chi,\downarrow}_{h} \tag{5.20b}$$

Finally, the regulation reserve balance constraints (4.5) and (4.6) are replaced by the following updated constraints:

$$\zeta^{r}_{h}=\sum_{g\in\mathcal{G}}\Delta p^{G,r,\uparrow}_{g,h}+\sum_{b\in\mathcal{B}}\sum_{l\in\mathcal{L}}\left(\Delta p^{B,D,r,\uparrow}_{b,l,h}+\Delta p^{B,C,r,\uparrow}_{b,l,h}\right) \tag{5.21a}$$

$$+\Delta p^{V,r,\uparrow}_{h}+\Delta p^{PF,r,\uparrow}_{h}+\Delta p^{VFC,r,\uparrow}_{h} \qquad \forall h\in\mathcal{H}^{r} \tag{5.21b}$$

$$\zeta^{r}_{h}=\sum_{g\in\mathcal{G}}\Delta p^{G,r,\downarrow}_{g,h}+\sum_{b\in\mathcal{B}}\sum_{l\in\mathcal{L}}\left(\Delta p^{B,D,r,\downarrow}_{b,l,h}\Delta p^{B,C,r,\downarrow}_{b,l,h}\right)+ \tag{5.21c}$$

$$+\Delta p^{V,r,\downarrow}_{h}+\Delta p^{PF,r,\downarrow}_{h}+\Delta p^{VFC,r,\downarrow}_{h} \qquad \forall h\in\mathcal{H}^{r} \tag{5.21d}$$

$$\zeta^{r}_{h}=\sum_{g\in\mathcal{G}}\Delta p^{G,r,\uparrow}_{g,h}+\sum_{b\in\mathcal{B}}\sum_{l\in\mathcal{L}}\left(\Delta p^{B,D,r,\uparrow}_{b,l,h}+\Delta p^{B,C,r,\uparrow}_{b,l,h}\right)+\Delta p^{V,r,\uparrow}_{h} \quad \forall h\in\mathcal{H}\setminus\mathcal{H}^{r} \tag{5.22a}$$

$$\zeta^{r}_{h}=\sum_{g\in\mathcal{G}}\Delta p^{G,r,\downarrow}_{g,h}+\sum_{b\in\mathcal{B}}\sum_{l\in\mathcal{L}}\left(\Delta p^{B,D,r,\downarrow}_{b,l,h}+\Delta p^{B,C,r,\downarrow}_{b,l,h}\right)+\Delta p^{V,r,\downarrow}_{h} \quad \forall h\in\mathcal{H}\setminus\mathcal{H}^{r} \tag{5.22b}$$

Based on the constraints defined above, an updated EMS model integrating TCL flexibility and its associated dynamics can be formulated. The following optimization model

corresponds to a MILP problem that can be solved using off-the-shelf solvers:

$$
\begin{aligned}
\min_{\boldsymbol{x},\boldsymbol{y},\boldsymbol{z}} \quad & \mathcal{F}^{OBJ}\left(\boldsymbol{x},\boldsymbol{y}\right) \\
\text{s.t.} \quad & \boldsymbol{x} \in \{0,1\}\,,\ \boldsymbol{y} \geq 0 \\
& \text{Reserves and power balance: (5.20)–(5.22), (3.25), (3.26), (5.19)} \\
& \text{Thermal generators: (4.1), (4.10), (3.29), (3.30)} \\
& \text{Batteries and degradation: (3.17), (4.2), (4.3), (3.22), (3.24),} \\
& \qquad\qquad\qquad\qquad\qquad \text{(4.11), (4.12), (3.31)} \\
& \text{Frequency dynamics: (4.13)-(4.16), (4.21d), (4.22)} \\
& \text{TCLs and virtual battery: (5.14)–(5.18)}
\end{aligned}
$$

where the objective function $\mathcal{F}^{OBJ}$ includes thermal generation, battery degradation, and load shedding costs; $\boldsymbol{x} = \left[\boldsymbol{u}^G, \boldsymbol{v}^G, \boldsymbol{w}^G\right]$ are binary decision variables; $\boldsymbol{y} = \left[\hat{\boldsymbol{p}}^G, \hat{\boldsymbol{p}}^W, \hat{\boldsymbol{p}}^S, \Delta\boldsymbol{p}^G, \Delta\boldsymbol{p}^B, \Delta\boldsymbol{p}^V, \Delta\boldsymbol{p}^{VFC}, \Delta\boldsymbol{p}^{PF}, \boldsymbol{s}^B, \boldsymbol{c}^B, \boldsymbol{d}^B, \boldsymbol{ls}, \boldsymbol{\zeta}\right]$ are non-negative continuous decisions variables; and $\boldsymbol{z} = \left[\hat{\boldsymbol{e}}^V, \hat{\boldsymbol{d}}^V\right]$ are free continuous decision variables.

5.2.2 Implementation Architecture

The general architecture required to implement the proposed EMS model embedding aggregate TCL control is illustrated in Figure 5.3. Note that as per [6], the proposed architecture follows a centralized approach for TCL control, in which direct communication links between the Aggregate TCL Controller and the different TCLs are needed to ensure a reliable coordinated control. Furthermore, observe that local frequency measurements are required for the Aggregate TCL Controller, such that frequency regulation services can be provided by it.

5.3 Computational Experiments

In this section, simulations to evaluate the benefits of the proposed virtual battery and EMS models are presented and discussed. First, the general settings considered in the experiments are described. Then, the proposed decoupled household thermal model and virtual battery model are benchmarked against the current state-of-art models. Finally, the implementation of an aggregate TCL control for improved microgrid operations is simulated, and its benefits quantified.

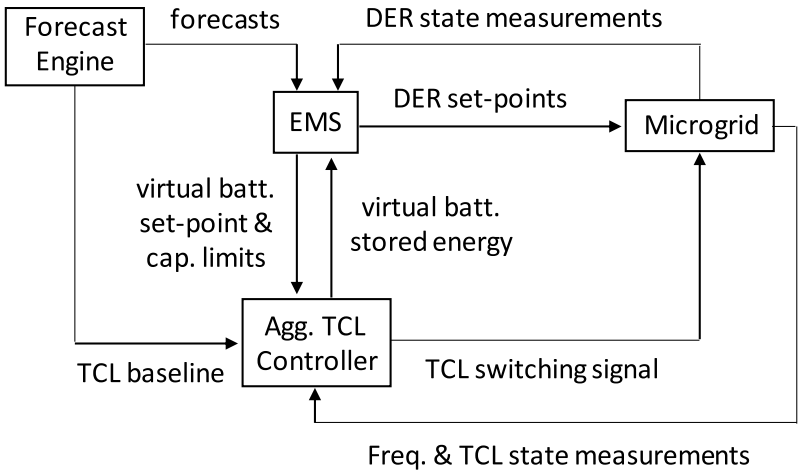

Figure 5.3: EMS and aggregate TCL control implementation architecture.

5.3.1 General Settings

The experiments are performed assuming the households used for the priority-stack TCL control presented in [6] are located in KLFN (53°35'N 88°39'W) during the fall season [5], given that detailed renewable generation and load data is available for this isolated community located in Canada. The test microgrid corresponds to the CIGRE-based medium voltage benchmark system presented in Section 4.2.1, but with a smaller 1324kW/1324kWh lithium-ion battery.

A collection of $N = 1800$ air conditioners operating in heating mode is assumed for the aggregate TCL control, which results from considering KLFN's population of 914 people, 3 inhabitants per household, and a scaling factor of 5.933 = 6153kW/1037kW based on the peak loads of the CIGRE-based microgrid used here and the KLFN microgrid from which renewable generation and load data is extracted. Air conditioner parameters $\eta^{TCL}, \overline{P}^{TCL}$, and $\Delta\theta^{TCL}$ are extracted from [6], and a thermostat setpoint $\theta^{I,SP} = 21°C$ is assumed. Thermal household parameters $R^W, R^C, R^F, C^W, C^I, C^F$ and variables $\theta^A, \theta^G, q^W, q^C$ are calculated using the procedure described in [83], assuming a typical North American house with a 12m x 9m surface area and 5.4m height (2 floors). To represent heterogeneity in the TCL population, random samples of house length, width and height, as well as $\eta^{TCL}, \overline{P}^{TCL}, \Delta\theta^{TCL}$, and $\theta^{I,SP}$ parameters, are generated from independent uniform distributions with a maximum deviation of ±5% around their nominal values.

Thermal dynamic simulations are run using the Julia programming language [91] and the DifferentialEquations package [100]. The EMS optimization model is solved in Julia using the JuMP package [92] and the Gurobi solver [66]. Frequency transient simulations are run using MATLAB-Simulink [76].

5.3.2 Thermal Model Accuracy

The accuracy of the first-order thermal model (2.8) and the proposed decoupled thermal model (5.1)-(5.4) is evaluated first. For this, one full day simulation of the thermal dynamics of a household is performed, and the inner, wall and floor temperatures resulting from the different models are compared.

Figure 5.4 illustrates the resulting inner temperature for the simple first-order model (2.8) and the more-detailed third-order model (2.13), for which a 1s time resolution and same initial conditions are used. Observe that the first-order model significantly differs from the highly-accurate third-order model after the 20 minute mark, indicating that the former is not sufficiently accurate to represent the daily thermal dynamics of a household in practical settings. This suggests that aggregate TCL control techniques based on a first-order thermal model would show a degraded performance.

Figure 5.5 illustrates the inner, wall, and floor temperatures for the proposed decoupled thermal model (5.1)-(5.4) and the highly-detailed third order model (2.13), in which a $DT = 5\text{min}$ timescale is considered for modeling wall/floor dynamics in the decoupled model. A close resemblance between both models can be observed in this case, indicating that the proposed decoupled model is adequate for developing more precise aggregate TCL control techniques, including the proposed virtual battery model presented in Section 5.1.2.

5.3.3 Comparison of Virtual Battery Models

In this section, the virtual battery model presented in Section 5.1.2 is compared against the current state-of-art model presented in [6] in terms of modeling accuracy. For the comparison, the implementation of both virtual battery models within an aggregate TCL controller is simulated, and their corresponding TCL load baseline and capacity limits are evaluated. TCL load baselines for the proposed and state-of-art virtual battery models are computed, respectively, from (5.6b) and the following steady-state equation based on (2.8):

$$p_0^{TCL,SS} = \left(\theta^I - \theta^A\right) / \eta^{TCL} R^A. \tag{5.23}$$

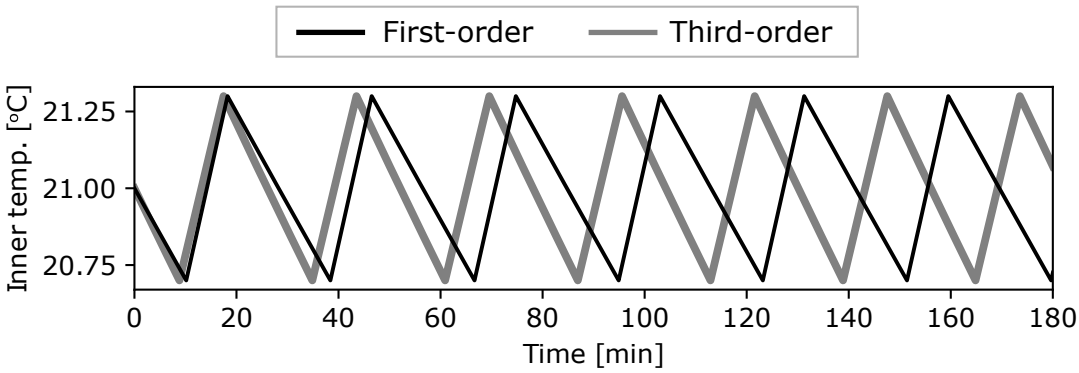

Figure 5.4: Comparison of the household's inner temperature for the first-order and third-order thermal models.

Capacity limits for the proposed and state-of-art models are calculated based on (5.12) and the "Maximimize n_- (Sufficient)" battery model presented in [6], respectively, with $R^A = \left(1/R^C + 1/R^W\right)^{-1}$ and $\gamma^V = (1/N) \sum_{n\in\mathcal{N}} \gamma_n^{TCL}$. Thermal simulations are performed using the decoupled household thermal model (see Sections 5.1.1 and 5.3.2).

The simulation results for the virtual battery model in [6] are illustrated in Figure 5.6a, for which a 2 MW discharging power is requested from the aggregate TCL controller. Note that due to an inaccurate TCL load baseline estimation, the controller delivers an erroneous 2+0.457 MW discharging power. Furthermore, observe that while the virtual battery operates within its energy capacity limits until $T_{lim} \approx 12.5$min, the controller loses its tracking capability significantly earlier at $T_{loss} \approx 9.4$min. This indicates an inaccurate virtual battery model, as the controller should lose its tracking capability only after surpassing the virtual battery's capacity limit.

The results for the proposed virtual battery model are presented in Figure 5.6b, for which the same 2 MW discharging signal is requested. Note that in this case, the controller correctly delivers the 2 MW discharging power, as an accurate baseline estimation is now used. Furthermore, observe that the controller's tracking capability is lost at $T_{loss} \approx 13.9$min, which is only 1.1min after the virtual battery reaches its energy capacity limit ($T_{lim} \approx 12.8$min). This is consistent with the conservativeness of the lower bounds (5.12) used for computing such limits, resulting in a more accurate virtual battery model.

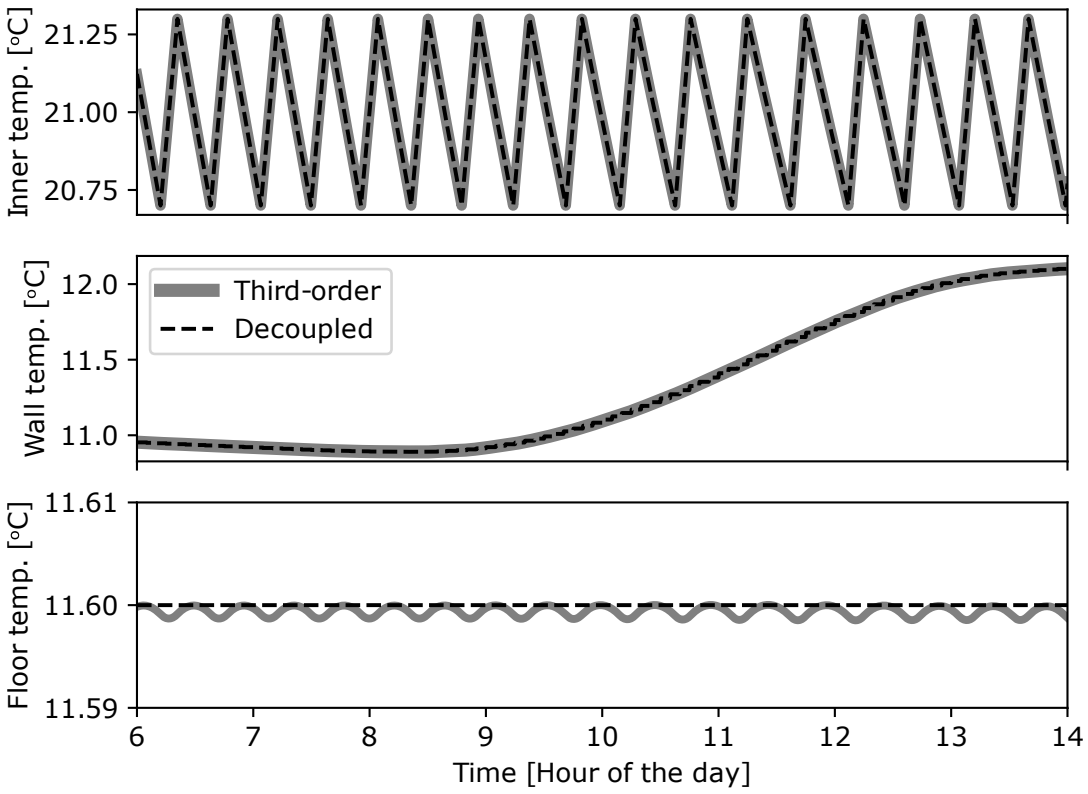

Figure 5.5: Comparison of the household's inner (top), wall (middle), and floor (bottom) temperatures for the third-order and proposed decoupled thermal models.

5.3.4 Integration in Microgrid Operation

The benefits of harvesting TCL flexibility for an enhanced microgrid operation are evaluated in this section. For this purpose, the implementation of two different EMS models is simulated:

1. The frequency-constrained EMS model presented in Chapter 4, which incorporates frequency dynamics but neglects TCL flexibility.
2. The novel EMS model presented in Section 5.2.1, which integrates frequency dynamics and the flexibility stemming from a coordinated TCL control.

Simulations are performed for one full day considering the same settings of the Base case in the computational experiments presented in Section 4.2, which include real measurements

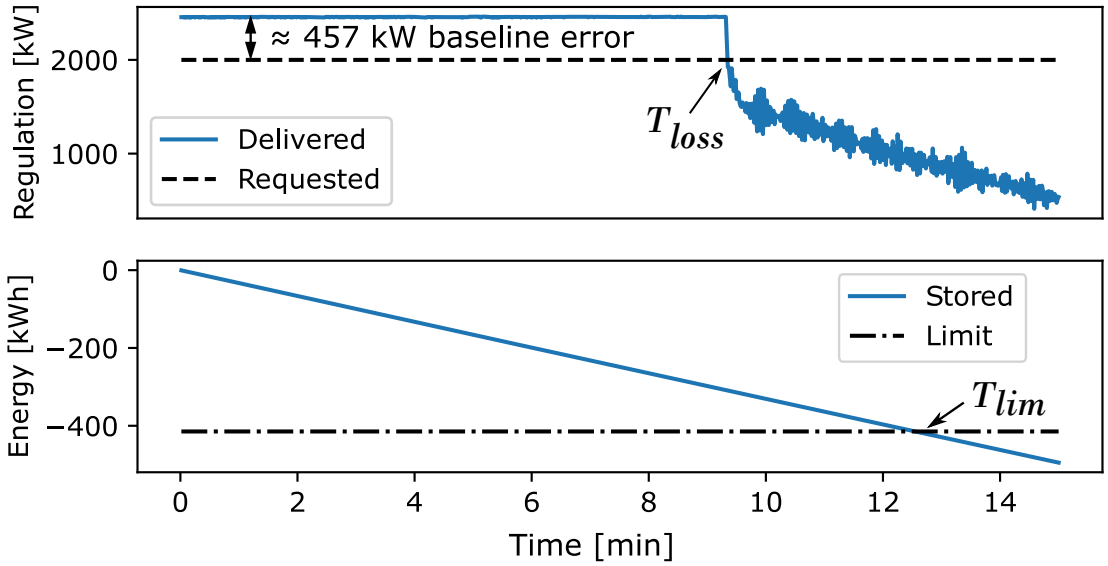

(a)

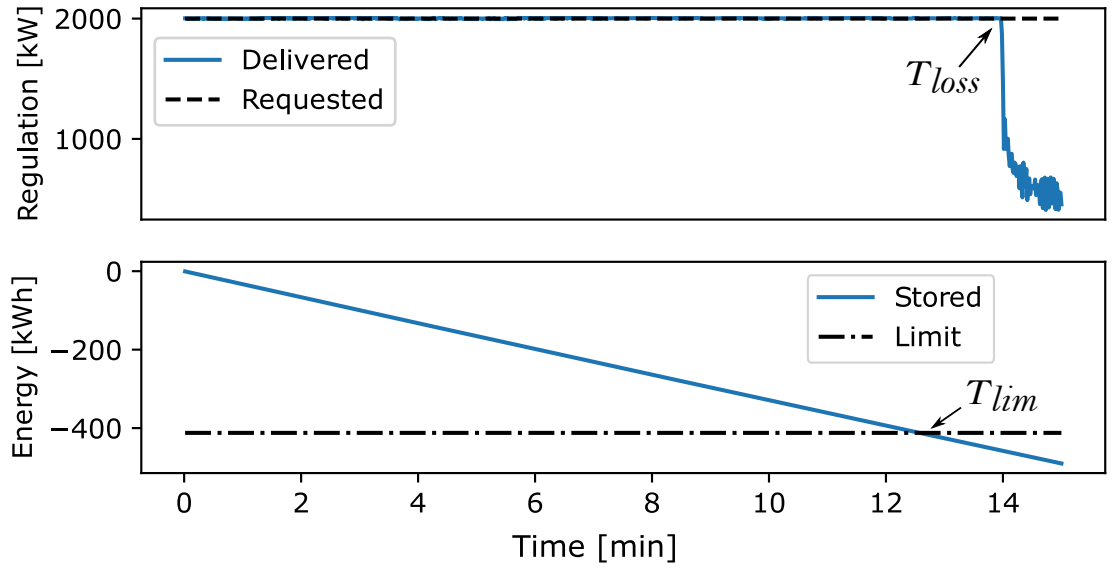

(b)

Figure 5.6: Regulation and stored energy for (a) the virtual battery model in [6], and (b) the proposed virtual battery model.

Table 5.1: EMS model comparison

Virtual Batt.	Comm. delay [s]	Oper. costs [kUSD]	Ren. curt. [kWh]	Load shed. [kWh]	Total non-compl. [s]	Comp. time [s]	
						Mean	Max.
No	-	17.025	1321	1.15	86	1.4	9.7
Yes	1	16.117	573	1.83	79	1.3	9.4
Yes	0.1	15.986	336	1.06	72	1.3	9.4

from the KLFN microgrid [5], detailed frequency transient models, and frequency and RoCoF limits in line with modern DER operating standards [86].

For the EMS model integrating TCL control, the transient model presented in Section 5.1.4 is considered, with $\kappa_h^V = 5\%$ [86], and two different communication delays $T_D^V = 1$ [99] and $T_D^V = 0.1$ [101], for which the low-pass filter is tuned to ensure a stable system response, yielding $T_F^V = 5$ and $T_F^V = 1$, respectively. Virtual battery capacity limits (5.13) are determined using 100 Monte Carlo samples drawn from two independent zero-mean normal distributions for solar irrandiance and ambient temperature forecast errors, whose standard deviations are extracted from Table 3.1 and [102], respectively. Note that 100 samples were used since the Monte Carlo simulations converged at that point. A safety derating factor of $\mu = 0.95$ was considered in EMS constraints (5.14) and (5.16).

The simulation results are presented in Table 5.1, for which the original frequency-constrained EMS model without TCL flexibility (first row) is compared against the proposed EMS model embedding TCL flexibility with a communication delay of $T_D^V = 1$s (second row), and $T_D^V = 0.1$s (third row). The table shows total operating costs, including renewable curtailment and load shedding costs, as well as the total accumulated renewable curtailment and load shedding for the simulated day. Moreover, the presented total non-compliance time measures the amount of time for which either frequency or RoCoF limits ($\pm$1.2Hz and $\pm$0.5Hz respectively) are violated. Furthermore, the mean and maximum computation times required to solve the optimization problem of an MPC iteration are also displayed. From the results, it can be observed that the proposed EMS model integrating TCL flexibility enables daily savings of 908 to 1039 USD (5.3%-6.1%) for a similar regulation security level (non-compliance $\leq$ 86s), at sufficiently low computation times for practical applications ($\ll$ 5min).

The resulting dispatch profiles from the different EMS models are presented in Figure 5.7 for the case with no virtual battery, Figure 5.8 for the case with virtual battery and $T_D^V = 1$s, and Figure 5.9 for the case with virtual battery and $T_D^V = 0.1$s, depicting thermal generation (G1-G5), renewable generation (RG), demand (D), battery discharge

(BD), battery charge (BC), virtual battery discharge (VBD), and virtual battery discharge (VBD). By comparing the figures, it can be observed that the virtual battery (VBC/VBD) tends to replace the "conventional" battery (BC/BD), as the former can provide energy shifting services without incurring into battery degradation costs, while having a sufficiently large energy capacity ($\approx$ 411 kWh). A similar trend is observed for the reserve provision service, in which the displacement of battery participation is more notorious due to the large power capacity of the virtual battery in this case ($\approx$ 3250 kW).

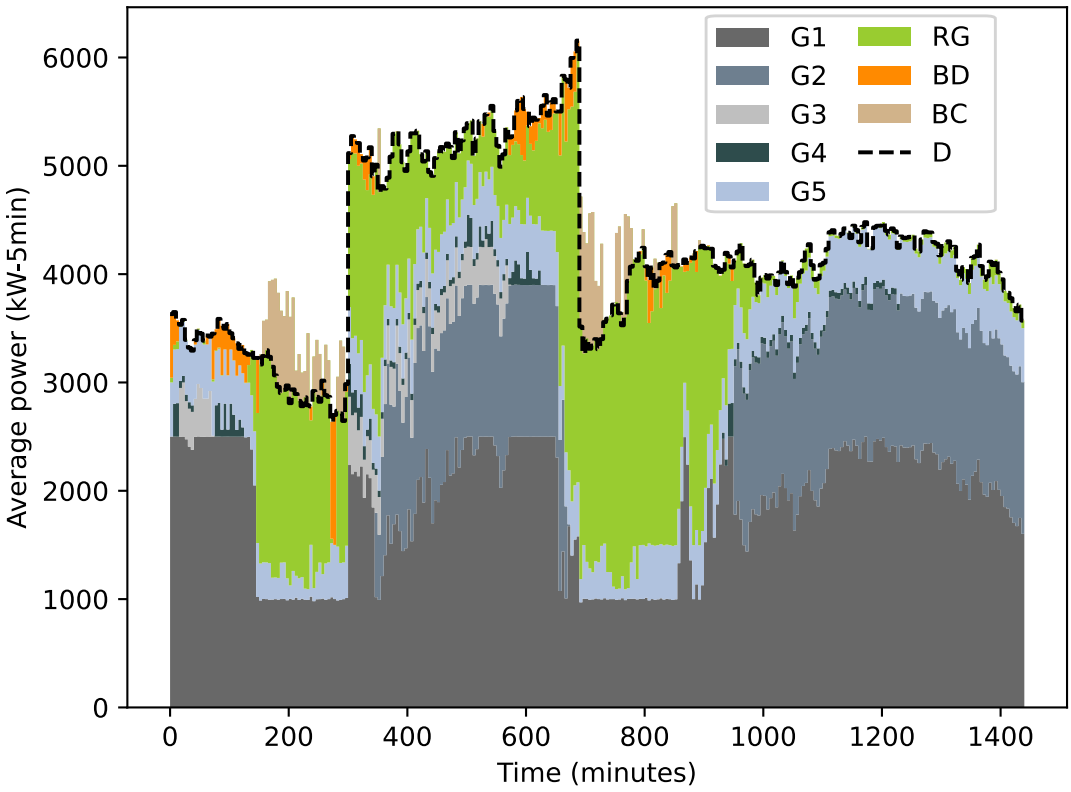

Figure 5.7: Dispatch results for case without TCL flexibility.

5.3.5 Validation of TCL Tracking Capability

In this section, the simulation results of Section 5.3.4 are used to evaluate the tracking capability of the aggregate TCL controller in practical microgrid operations. For this test, the TCL regulation signal p^V resulting from the frequency transient simulations is used

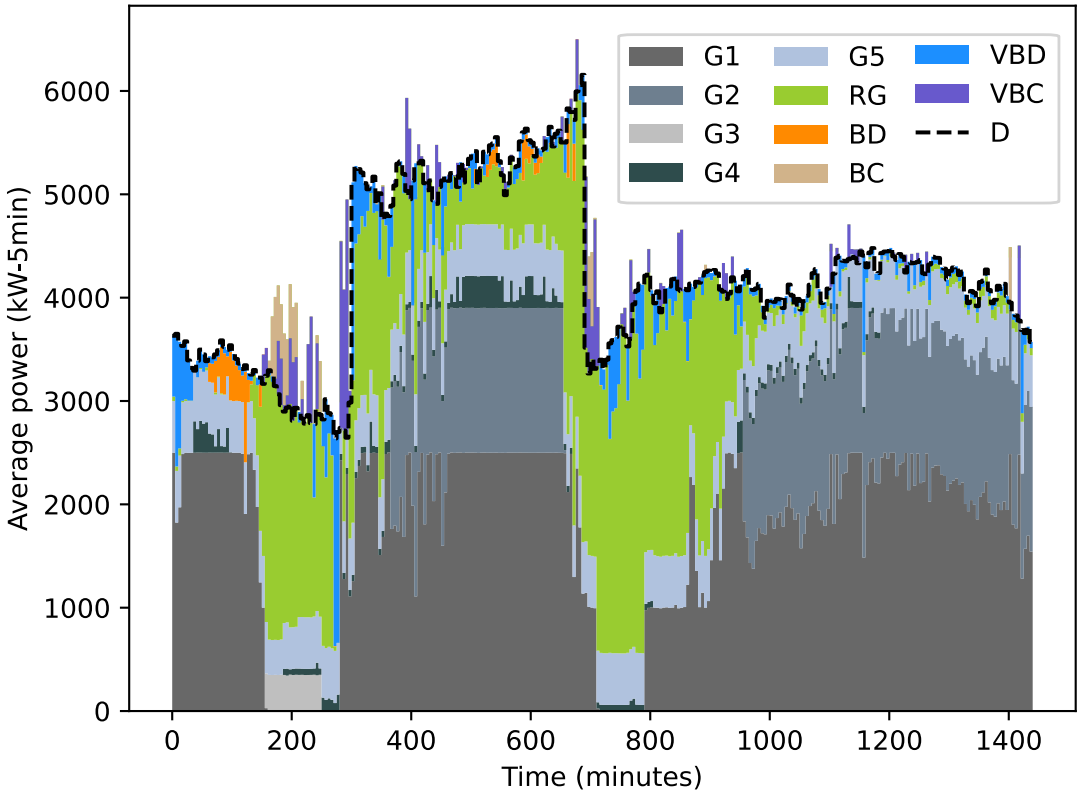

Figure 5.8: Dispatch results for case with TCL flexibility (virtual battery) considering a communication delay of $T_D^V = 1$s.

as an input for the aggregate TCL controller, and the response of each of the 1800 TCLs composing the TCL aggregation is simulated in detail considering high-order household thermal dynamics and a deadband ON/OFF control. With these results, the differences between the estimated TCL regulation considered in the frequency transient simulations, and actual regulation provided by the TCL population can be calculated.

Figure 5.10 illustrates the resulting mismatches between estimated and actual TCL response, considering a communication delay of $T_D^V = 1$s (second row in Table 5.1). Observe that the TCLs are capable of accurately tracking the requested regulation signal, with a maximum error of approximately the rated power of one TCL ($\approx$ 6 kW). This demonstrates the validity of the proposed virtual battery model and frequency transient model for representing the flexibility and frequency dynamics of an aggregate TCL control.

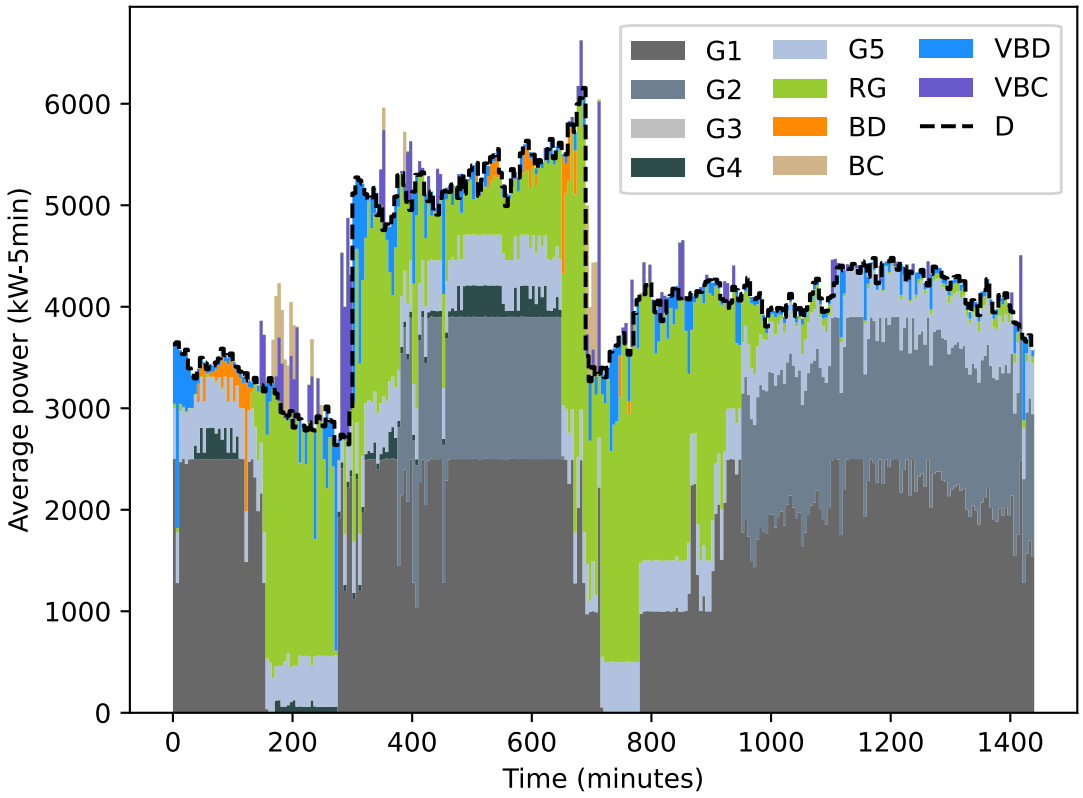

Figure 5.9: Dispatch results for case with TCL flexibility (virtual battery) considering a communication delay of $T_D^V = 0.1$s.

5.4 Summary

The present chapter discussed the integration of TCLs within EMS models for an improved frequency control and operation of isolated microgrids. For this purpose, two computationally efficient aggregate TCL models were developed, which describe the flexibility and frequency dynamics of aggregated TCLs, while taking into account relevant practical challenges such as high-order household thermal dynamics, communication delays, and the presence of model uncertainty and time-variability. These aggregate models were then used to design a practical microgrid EMS incorporating TCLs, and analyze its corresponding impact on microgrid operation and frequency regulation. Computational experiments on a realistic isolated microgrid using detailed thermal and frequency transient models demonstrated the high modeling accuracy of the proposed aggregate TCL models, and

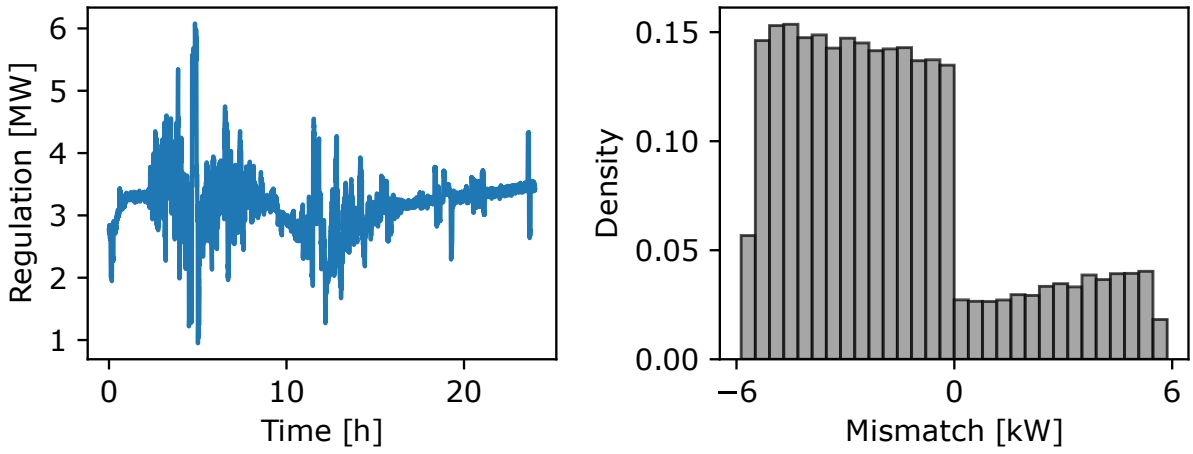

Figure 5.10: Estimated regulation provided by the TCL aggregation and mismatch between estimated and actually delivered TCL regulation

showed that an EMS embedding TCL flexibility can enable significant daily savings in the order of 5%-6%, while meeting frequency regulation security levels in line with modern DER operating standards.

Chapter 6

Conclusion

6.1 Summary and Conclusions

This thesis focused on the design of a centralized EMS model for isolated microgrids, which, unlike conventional power systems, are characterized by a low system inertia and significant renewable integration. To address these challenges, the integration of renewable short-term power fluctuations within EMS models was studied, including how these fluctuations can impact the system's frequency regulation, and how CESS (i.e., BESS) and VESS (i.e., TCL control) can be used to counter-balance these fluctuations, as highlighted next.

In Chapter 3, computationally efficient models were developed for characterizing renewable short-term power fluctuations and BESS, which included the impact of short-term fluctuations on microgrid operation, and how the battery lifetime was affected due to the provision of regulation services. These models were then used to develop a first version of the proposed EMS, which, as demonstrated through simulations on two realistic test microgrids, outperforms the current industry standard in terms of operating costs and system reliability, and can be solved within reasonable computation times.

In Chapter 4, a second version of the proposed EMS was developed, for which the impact of renewable short-term power fluctuations on frequency dynamics was integrated in the EMS's decision-making process. This was accomplished through the development of accurate linear equations describing the frequency deviation and RoCoF resulting from short-term fluctuations, yielding a more detailed, yet computationally efficient, frequency-constrained EMS model. The advantages of this EMS model were demonstrated through detailed transient simulations on a realistic test microgrid, highlighting not only its eco-

nomic benefits, but also its capability to comply with modern DER operating standards in terms of frequency regulation performance.

Finally, in Chapter 5, the complete version of the proposed EMS model was presented, for which the additional flexibility stemming from an aggregate TCL control was integrated within the microgrid EMS. This was accomplished through the use of VESS models, which capture the capability and limitations of an aggregate TCL control in a computationally efficient way, allowing their integration within the optimization routines of EMS models. Computational experiments using detailed frequency transient and thermal dynamic models were presented, demonstrating the accuracy of the proposed VESS models and the operational benefits resulting from using them to integrate TCLs in microgrid operation.

The main conclusions of this thesis can be summarized as follows:

- Second-to-second power fluctuations stemming from wind and solar generation directly impact the operation and frequency regulation of isolated microgrids, and thus must be incorporated in modern microgrid EMS. Neglecting these fluctuations in microgrid EMS can lead to higher operational costs resulting from the inefficient allocation of system reserves, as well as reduced system reliability.

- Frequency dynamics and regulation, which have been typically neglected in UC and other operational models, need to be integrated in the design and validation process of modern EMS for isolated microgrids. Neglecting such dynamics can lead to not only higher operational costs and lower system reliability, but also in the failure to meet modern DER operating standards.

- BESS are a key flexibility source for the enhanced operation of isolated microgrids, and thus should be included in microgrid EMS. However, special attention must be given in modeling the battery degradation resulting from BESS operation, which, as demonstrated here, can play a relevant role in reducing system operating costs.

- Aggregate TCL control techniques are a relevant flexibility source for the enhanced operation of isolated microgrids, making their integration in microgrid EMS relevant. This can be achieved through the use of computationally efficient VESS models, which allow integrating the flexibility and limitations of TCLs in the optimization routines of microgrid EMS. Similar to the case of BESS, special attention must be given to practical challenges resulting from TCL integration, namely, TCL thermal dynamics, communication delays, and the presence of VESS model uncertainty and time-variability.

- Computational efficiency plays a fundamental role in the design of modern microgrid EMS models, as sufficiently low computation times are needed for the implementation of MPC schemes typically found in microgrid EMS. Accordingly, efficient yet sufficiently accurate mathematical models were developed throughout this thesis.

6.2 Contributions

The main contributions of this thesis are the following:

- Mathematical models characterizing renewable short-term power fluctuation and their impact on microgrid operation and frequency regulation were developed. Computational efficiency was considered in the design process of these models, allowing their incorporation in practical microgrid EMS.
- Mathematical models describing the flexibility of BESS and aggregate TCL control were developed. The proposed models included key practical challenges associated with both technologies, namely, BESS degradation, TCL thermal dynamics, and the presence of communication delays in aggregate TCL controls. Furthermore, computational efficiency was considered in the models' design process, allowing their incorporation in microgrid EMS.
- A comprehensive microgrid EMS model was developed integrating renewable short-term fluctuations and the capability of BESS and TCL to counter-balance such fluctuations. The proposed EMS adequately balances modeling detail and computational efficiency, allowing its practical implementation in MPC schemes.
- Computational experiments using detailed frequency transient and thermal dynamic models in realistic settings were performed to demonstrate the validity of the models proposed in this thesis, highlighting the economic and reliability benefits resulting from their incorporation into EMS for isolated microgrids.

Two IEEE journal papers [93] and [98] have been published based on the content presented in Chapters 3 and 4. A third journal paper based on the contents presented in Chapter 5 has been submitted for publication [103].

6.3 Future Work

Based on the work presented in this thesis, the following topics could be researched in the future:

- Study second-to-second reactive power fluctuations and their impact on the voltage dynamics of isolated microgrids. Furthermore, evaluate if these play a significant role in microgrid operations, and if so, investigate how these could be integrated in microgrid EMS models.
- Study the use of VESS models for characterizing decentralized TCL control techniques, and investigate how these could be integrated in microgrid EMS models while preserving computational tractability for practical applications.
- Study how the modeling of renewable short-term power fluctuations would affect existing microgrid planning models, and how these fluctuations could be incorporated in their decision-making process.

References

[1] I. Hadjipaschalis, A. Poullikkas, and V. Efthimiou, "Overview of current and future energy storage technologies for electric power applications," *Renewable and Sustainable Energy Reviews*, vol. 13, no. 6-7, pp. 1513–1522, Sep. 2009.

[2] K. Yeager and J. Willis, "Modeling of emergency diesel generators in an 800 megawatt nuclear power plant," *IEEE Transactions on Energy Conversion*, vol. 8, no. 3, pp. 433–441, 1993.

[3] X. Xu, M. Bishop, D. G. Oikarinen, and C. Hao, "Application and modeling of battery energy storage in power systems," *CSEE Journal of Power and Energy Systems*, vol. 2, no. 3, pp. 82–90, 2016.

[4] M. Farrokhabadi, C. A. Cañizares, and K. Bhattacharya, "Frequency control in isolated/islanded microgrids through voltage regulation," *IEEE Transactions on Smart Grid*, vol. 8, no. 3, pp. 1185–1194, 2017.

[5] M. Arriaga and C. Cañizares, "Overview and Analysis of Data for Microgrid at Kasabonika Lake First Nation (KLFN)," Hatch Project, University of Waterloo, Tech. Rep., 2015.

[6] H. Hao, B. M. Sanandaji, K. Poolla, and T. L. Vincent, "Aggregate flexibility of thermostatically controlled loads," *IEEE Transactions on Power Systems*, vol. 30, no. 1, pp. 189–198, 2015.

[7] X. Hu, C. Zou, C. Zhang, and Y. Li, "Technological developments in batteries: A survey of principal roles, types, and management needs," *IEEE Power and Energy Magazine*, vol. 15, no. 5, pp. 20–31, Sep. 2017.

[8] R. Palma-Behnke, C. Benavides, F. Lanas, B. Severino, L. Reyes, J. Llanos, and D. Sáez, "A microgrid energy management system based on the rolling horizon strategy," *IEEE Trans. Smart Grid*, vol. 4, no. 2, pp. 996–1006, 2013.

[9] N. Hatziargyriou, H. Asano, R. Iravani, and C. Marnay, "Microgrids," *IEEE Power and Energy Magazine*, vol. 5, no. 4, pp. 78–94, July 2007.

[10] D. E. Olivares, A. Mehrizi-Sani, A. H. Etemadi, C. A. Cañizares, R. Iravani, M. Kazerani, A. H. Hajimiragha, O. Gomis-Bellmunt, M. Saeedifard, R. Palma-Behnke, G. A. Jiménez-Estévez, and N. D. Hatziargyriou, "Trends in microgrid control," *IEEE Transactions on Smart Grid*, vol. 5, no. 4, pp. 1905–1919, July 2014.

[11] M. Farrokhabadi, C. A. Cañizares, J. W. Simpson-Porco, E. Nasr, L. Fan, P. A. Mendoza-Araya, R. Tonkoski, U. Tamrakar, N. Hatziargyriou, D. Lagos, R. W. Wies, M. Paolone, M. Liserre, L. Meegahapola, M. Kabalan, A. H. Hajimiragha, D. Peralta, M. A. Elizondo, K. P. Schneider, F. K. Tuffner, and J. Reilly, "Microgrid stability, definitions, analysis, and modeling," IEEE Power and Energy Society, Piscataway, NJ, USA, Tech. Rep. PES-TR66, 2018.

[12] M. Anvari, G. Lohmann, M. Wächter, P. Milan, E. Lorenz, D. Heinemann, M. R. R. Tabar, and J. Peinke, "Short term fluctuations of wind and solar power systems," *New Journal of Physics*, vol. 18, no. 6, 2016.

[13] H. Bevrani, A. Ghosh, and G. Ledwich, "Renewable energy sources and frequency regulation: survey and new perspectives," *IET Renewable Power Generation*, vol. 4, no. 5, pp. 438–457, 2010.

[14] "Electrical energy storage," International Electrotechnical Commission, Tech. Rep., 2011. [Online]. Available: https://www.iec.ch/basecamp/electrical-energy-storage

[15] M. Farrokhabadi, B. V. Solanki, C. A. Canizares, K. Bhattacharya, S. Koenig, P. S. Sauter, T. Leibfried, and S. Hohmann, "Energy storage in microgrids: Compensating for generation and demand fluctuations while providing ancillary services," *IEEE Power and Energy Magazine*, vol. 15, no. 5, pp. 81–91, Sep. 2017.

[16] N. O'Connell, P. Pinson, H. Madsen, and M. O'Malley, "Benefits and challenges of electrical demand response: A critical review," *Renewable and Sustainable Energy Reviews*, vol. 39, pp. 686–699, 2014.

[17] "Residential energy consumption survey," U.S. Energy Information Administration, Tech. Rep., 2015. [Online]. Available: https://www.eia.gov/consumption/residential/data/2015/

[18] D. S. Callaway and I. A. Hiskens, "Achieving controllability of electric loads," *Proceedings of the IEEE*, vol. 99, no. 1, pp. 184–199, 2011.

[19] J. L. Mathieu, M. Kamgarpour, J. Lygeros, G. Andersson, and D. S. Callaway, "Arbitraging intraday wholesale energy market prices with aggregations of thermostatic loads," *IEEE Transactions on Power Systems*, vol. 30, no. 2, pp. 763–772, 2015.

[20] V. Trovato, S. H. Tindemans, and G. Strbac, "Leaky storage model for optimal multi-service allocation of thermostatic loads," *IET Generation, Transmission & Distribution*, vol. 10, no. 3, pp. 585–593, 2016.

[21] J. L. Mathieu, M. G. Vayá, and G. Andersson, "Uncertainty in the flexibility of aggregations of demand response resources," in *IECON 2013 - 39th Annual Conference of the IEEE Industrial Electronics Society*, 2013, pp. 8052–8057.

[22] D. E. Olivares, C. A. Cañizares, and M. Kazerani, "A centralized energy management system for isolated microgrids," *IEEE Trans. Smart Grid*, vol. 5, no. 4, pp. 1864–1875, 2014.

[23] B. V. Solanki, A. Raghurajan, K. Bhattacharya, and C. A. Cañizares, "Including smart loads for optimal demand response in integrated energy management systems for isolated microgrids," *IEEE Transactions on Smart Grid*, vol. 8, no. 4, pp. 1739–1748, 2017.

[24] B. V. Solanki, K. Bhattacharya, and C. A. Cañizares, "A sustainable energy management system for isolated microgrids," *IEEE Transactions on Sustainable Energy*, vol. 8, no. 4, pp. 1507–1517, Oct. 2017.

[25] M. Farrokhabadi, C. A. Cañizares, and K. Bhattacharya, "Unit commitment for isolated microgrids considering frequency control," *IEEE Trans. Smart Grid*, vol. 9, no. 4, pp. 3270–3280, 2018.

[26] W. Violante, C. A. Cañizares, M. A. Trovato, and G. Forte, "An energy management system for isolated microgrids with thermal energy resources," *IEEE Transactions on Smart Grid*, vol. 11, no. 4, pp. 2880–2891, 2020.

[27] B. V. Solanki, C. A. Cañizares, and K. Bhattacharya, "Practical energy management systems for isolated microgrids," *IEEE Trans. Smart Grid*, vol. 10, no. 5, pp. 4762–4775, 2019.

[28] M. F. Zia, E. Elbouchikhi, and M. Benbouzid, "Microgrids energy management systems: A critical review on methods, solutions, and prospects," *Applied Energy*, vol. 222, pp. 1033 – 1055, 2018.

[29] H. Shayeghi, E. Shahryari, M. Moradzadeh, and P. Siano, "A survey on microgrid energy management considering flexible energy sources," *Energies*, vol. 12, no. 11, 2019.

[30] D. E. Olivares, J. D. Lara, C. A. Cañizares, and M. Kazerani, "Stochastic-predictive energy management system for isolated microgrids," *IEEE Transactions on Smart Grid*, vol. 6, no. 6, pp. 2681–2693, Nov. 2015.

[31] J. D. Lara, D. E. Olivares, and C. A. Cañizares, "Robust energy management of isolated microgrids," *IEEE Systems Journal*, vol. 13, no. 1, pp. 680–691, March 2019.

[32] Z. Shi, H. Liang, S. Huang, and V. Dinavahi, "Distributionally robust chance-constrained energy management for islanded microgrids," *IEEE Transactions on Smart Grid*, vol. 10, no. 2, pp. 2234–2244, 2019.

[33] D. Romero-Quete and C. A. Cañizares, "An affine arithmetic-based energy management system for isolated microgrids," *IEEE Transactions on Smart Grid*, vol. 10, no. 3, pp. 2989–2998, May 2019.

[34] Z. Bao, Q. Zhou, Z. Yang, Q. Yang, L. Xu, and T. Wu, "A multi time-scale and multi energy-type coordinated microgrid scheduling solution—part i: Model and methodology," *IEEE Trans. Power Systems*, vol. 30, no. 5, pp. 2257–2266, 2015.

[35] C. Ju, P. Wang, L. Goel, and Y. Xu, "A two-layer energy management system for microgrids with hybrid energy storage considering degradation costs," *IEEE Trans. Smart Grid*, vol. 9, no. 6, pp. 6047–6057, 2018.

[36] C. Zhang, Y. Xu, Z. Y. Dong, and J. Ma, "Robust operation of microgrids via two-stage coordinated energy storage and direct load control," *IEEE Trans. Power Syst.*, vol. 32, no. 4, pp. 2858–2868, 2017.

[37] M. Paturet, U. Markovic, S. Delikaraoglou, E. Vrettos, P. Aristidou, and G. Hug, "Stochastic unit commitment in low-inertia grids," *IEEE Trans. Power Systems*, vol. 35, no. 5, pp. 3448–3458, 2020.

[38] Z. Chu, U. Markovic, G. Hug, and F. Teng, "Towards optimal system scheduling with synthetic inertia provision from wind turbines," *IEEE Trans. Power Systems*, vol. 35, no. 5, pp. 4056–4066, 2020.

[39] S. Saberi Oskouee, S. Kamali, and T. Amraee, "Primary frequency support in unit commitment using a multi-area frequency model with flywheel energy storage," *IEEE Trans. Power Systems*, pp. 1–1, 2021.

[40] L. Badesa, F. Teng, and G. Strbac, "Simultaneous scheduling of multiple frequency services in stochastic unit commitment," *IEEE Trans. Power Systems*, vol. 34, no. 5, pp. 3858–3868, 2019.

[41] ——, "Conditions for regional frequency stability in power system scheduling—part II: Application to unit commitment," *IEEE Trans. Power Systems*, pp. 1–1, 2021.

[42] B. Xu, J. Zhao, T. Zheng, E. Litvinov, and D. S. Kirschen, "Factoring the cycle aging cost of batteries participating in electricity markets," *IEEE Trans. Power Syst.*, vol. 33, no. 2, pp. 2248–2259, 2018.

[43] B. Xu, A. Oudalov, A. Ulbig, G. Andersson, and D. S. Kirschen, "Modeling of lithium-ion battery degradation for cell life assessment," *IEEE Trans. Smart Grid*, vol. 9, no. 2, pp. 1131–1140, 2018.

[44] T. A. Nguyen and M. L. Crow, "Stochastic optimization of renewable-based microgrid operation incorporating battery operating cost," *IEEE Trans. Power Syst.*, vol. 31, no. 3, pp. 2289–2296, 2016.

[45] M. Manbachi and M. Ordonez, "AMI-based energy management for islanded ac/dc microgrids utilizing energy conservation and optimization," *IEEE Transactions on Smart Grid*, vol. 10, no. 1, pp. 293–304, 2019.

[46] M. F. Zia, E. Elbouchikhi, M. Benbouzid, and J. M. Guerrero, "Energy management system for an islanded microgrid with convex relaxation," *IEEE Transactions on Industry Applications*, vol. 55, no. 6, pp. 7175–7185, 2019.

[47] I. Duggal and B. Venkatesh, "Short-term scheduling of thermal generators and battery storage with depth of discharge-based cost model," *IEEE Trans. Power Syst.*, vol. 30, no. 4, pp. 2110–2118, 2015.

[48] N. Padmanabhan, M. Ahmed, and K. Bhattacharya, "Battery energy storage systems in energy and reserve markets," *IEEE Transactions on Power Systems*, vol. 35, no. 1, pp. 215–226, Jan. 2020.

[49] B. Xu, Y. Shi, D. S. Kirschen, and B. Zhang, "Optimal battery participation in frequency regulation markets," *IEEE Trans. Power Syst.*, vol. 33, no. 6, pp. 6715–6725, 2018.

[50] G. He, Q. Chen, C. Kang, P. Pinson, and Q. Xia, "Optimal bidding strategy of battery storage in power markets considering performance-based regulation and battery cycle life," *IEEE Transactions on Smart Grid*, vol. 7, no. 5, pp. 2359–2367, Sep. 2016.

[51] D. S. Kirschen, G. Strbac, P. Cumperayot, and D. de Paiva Mendes, "Factoring the elasticity of demand in electricity prices," *IEEE Transactions on Power Systems*, vol. 15, no. 2, pp. 612–617, May 2000.

[52] A. Papavasiliou and S. S. Oren, "Large-scale integration of deferrable demand and renewable energy sources," *IEEE Transactions on Power Systems*, vol. 29, no. 1, pp. 489–499, Jan. 2014.

[53] A. Khodaei, M. Shahidehpour, and S. Bahramirad, "SCUC with hourly demand response considering intertemporal load characteristics," *IEEE Transactions on Smart Grid*, vol. 2, no. 3, pp. 564–571, Sep. 2011.

[54] N. O'Connell, P. Pinson, H. Madsen, and M. O'Malley, "Economic dispatch of demand response balancing through asymmetric block offers," *IEEE Transactions on Power Systems*, vol. 31, no. 4, pp. 2999–3007, July 2016.

[55] W. Mendieta and C. A. Cañizares, "Primary frequency control in isolated microgrids using thermostatically controllable loads," *IEEE Transactions on Smart Grid*, vol. 12, no. 1, pp. 93–105, 2021.

[56] D. Patteeuw, K. Bruninx, A. Arteconi, E. Delarue, W. D'haeseleer, and L. Helsen, "Integrated modeling of active demand response with electric heating systems coupled to thermal energy storage systems," *Applied Energy*, vol. 151, pp. 306–319, Aug. 2015.

[57] K. Bruninx, Y. Dvorkin, E. Delarue, W. D'haeseleer, and D. S. Kirschen, "Valuing demand response controllability via chance constrained programming," *IEEE Transactions on Sustainable Energy*, vol. 9, no. 1, pp. 178–187, Jan. 2018.

[58] Y. Zhang, S. Shen, and J. L. Mathieu, "Distributionally robust chance-constrained optimal power flow with uncertain renewables and uncertain reserves provided by loads," *IEEE Transactions on Power Systems*, vol. 32, no. 2, pp. 1378–1388, March 2017.

[59] M. Vrakopoulou, B. Li, and J. L. Mathieu, "Chance constrained reserve scheduling using uncertain controllable loads part i: Formulation and scenario-based analysis," *IEEE Transactions on Smart Grid*, vol. 10, no. 2, pp. 1608–1617, March 2019.

[60] V. Trovato, F. Teng, and G. Strbac, "Role and benefits of flexible thermostatically controlled loads in future low-carbon systems," *IEEE Transactions on Smart Grid*, vol. 9, no. 5, pp. 5067–5079, 2018.

[61] P. Bacher and H. Madsen, "Identifying suitable models for the heat dynamics of buildings," *Energy and Buildings*, vol. 43, no. 7, pp. 1511–1522, 2011.

[62] E. Unamuno and J. A. Barrena, "Hybrid ac/dc microgrids—Part I: Review and classification of topologies," *Renewable and Sustainable Energy Reviews*, vol. 52, pp. 1251–1259, Dec. 2015.

[63] N. Padhy, "Unit commitment-a bibliographical survey," *IEEE Transactions on Power Systems*, vol. 19, no. 2, pp. 1196–1205, 2004.

[64] S. Y. Abujarad, M. Mustafa, and J. Jamian, "Recent approaches of unit commitment in the presence of intermittent renewable energy resources: A review," *Renewable and Sustainable Energy Reviews*, vol. 70, pp. 215–223, 2017.

[65] Q. P. Zheng, J. Wang, and A. L. Liu, "Stochastic optimization for unit commitment—A review," *IEEE Transactions on Power Systems*, vol. 30, no. 4, pp. 1913–1924, July 2015.

[66] Gurobi Optimization, LLC, "Gurobi Optimizer Reference Manual," 2021. [Online]. Available: https://www.gurobi.com

[67] International Business Machines (IBM) Corporation, "IBM ILOG CPLEX Optimization Studio documentation," 2021. [Online]. Available: https://www.ibm.com/docs/en/icos

[68] D. Pozo, J. Contreras, and E. E. Sauma, "Unit commitment with ideal and generic energy storage units," *IEEE Transactions on Power Systems*, vol. 29, no. 6, pp. 2974–2984, Nov. 2014.

[69] J. Wang, J. Purewal, P. Liu, J. Hicks-Garner, S. Soukazian, E. Sherman, A. Sorenson, L. Vu, H. Tataria, and M. W. Verbrugge, "Degradation of lithium ion batteries employing graphite negatives and nickel–cobalt–manganese oxide+ spinel manganese oxide positives: Part 1, aging mechanisms and life estimation," *Journal of Power Sources*, vol. 269, pp. 937–948, Dec. 2014.

[70] Q. Zhang and R. E. White, "Capacity fade analysis of a lithium ion cell," *Journal of Power Sources*, vol. 179, no. 2, pp. 793–798, May 2008.

[71] M. Safari, M. Morcrette, A. Teyssot, and C. Delacourt, "Multimodal physics-based aging model for life prediction of li-ion batteries," *Journal of The Electrochemical Society*, vol. 156, no. 3, pp. A145–A153, Dec. 2009.

[72] S. B. Peterson, J. Apt, and J. Whitacre, "Lithium-ion battery cell degradation resulting from realistic vehicle and vehicle-to-grid utilization," *Journal of Power Sources*, vol. 195, no. 8, pp. 2385–2392, April 2010.

[73] M. A. Ortega-Vazquez, "Optimal scheduling of electric vehicle charging and vehicle-to-grid services at household level including battery degradation and price uncertainty," *IET Generation, Transmission Distribution*, vol. 8, no. 6, pp. 1007–1016, June 2014.

[74] "Standard practices for cycle counting in fatigue analysis," American Society for Testing and Materials, Standard, 2011. [Online]. Available: https://www.astm.org/Standards/E1049

[75] G. Marsh, C. Wignall, P. R. Thies, N. Barltrop, A. Incecik, V. Venugopal, and L. Johanning, "Review and application of rainflow residue processing techniques for accurate fatigue damage estimation," *International Journal of Fatigue*, vol. 82, pp. 757–765, Jan. 2016.

[76] MATLAB, *version 9.10.0 (R2021a)*. Natick, Massachusetts: The MathWorks Inc., 2021. [Online]. Available: https://www.mathworks.com

[77] J. L. Mathieu, S. Koch, and D. S. Callaway, "State estimation and control of electric loads to manage real-time energy imbalance," *IEEE Transactions on Power Systems*, vol. 28, no. 1, pp. 430–440, 2013.

[78] S. Ross and J. Mathieu, "Strategies for network-safe load control with a third-party aggregator and a distribution operator," *IEEE Transactions on Power Systems*, vol. 36, no. 4, pp. 3329–3339, 2021.

[79] L. Zhao, W. Zhang, H. Hao, and K. Kalsi, "A geometric approach to aggregate flexibility modeling of thermostatically controlled loads," *IEEE Transactions on Power Systems*, vol. 32, no. 6, pp. 4721–4731, 2017.

[80] S. H. Tindemans, V. Trovato, and G. Strbac, "Decentralized control of thermostatic loads for flexible demand response," *IEEE Transactions on Control Systems Technology*, vol. 23, no. 5, pp. 1685–1700, Sep. 2015.

[81] W. Zhang, J. Lian, C. Chang, and K. Kalsi, "Aggregated modeling and control of air conditioning loads for demand response," *IEEE Transactions on Power Systems*, vol. 28, no. 4, pp. 4655–4664, Nov. 2013.

[82] J. M. G. López, E. Pouresmaeil, C. A. Cañizares, K. Bhattacharya, A. Mosaddegh, and B. V. Solanki, "Smart residential load simulator for energy management in smart grids," *IEEE Transactions on Industrial Electronics*, vol. 66, no. 2, pp. 1443–1452, 2019.

[83] I. Calero, C. A. Cañizares, K. Bhattacharya, and R. Baldick, "Duck-curve mitigation in power grids with high penetration of pv generation," *IEEE Transactions on Smart Grid*, vol. 13, no. 1, pp. 314–329, 2022.

[84] P. Kundur and N. Balu, *Power System Stability and Control*, ser. EPRI power system engineering series. McGraw-Hill, 1994.

[85] J. Machowski, J. Bialek, and J. Bumby, *Power System Dynamics: Stability and Control*, 2nd ed. Wiley, 2011.

[86] "IEEE standard for interconnection and interoperability of distributed energy resources with associated electric power systems interfaces," *IEEE Std 1547-2018 (Revision of IEEE Std 1547-2003)*, 2018.

[87] N. N. A. Bakar, M. Y. Hassan, M. F. Sulaima, M. N. Mohd Nasir, and A. Khamis, "Microgrid and load shedding scheme during islanded mode: A review," *Renewable and Sustainable Energy Reviews*, vol. 71, pp. 161–169, 2017.

[88] R. C. Geary, "Moments of the ratio of the mean deviation to the standard deviation for normal samples," *Biometrika*, vol. 28, no. 3, pp. 295–307, 1936.

[89] S. Boyd and L. Vandenberghe, "Localization and cutting-plane methods," Stanford EE 364b course, Lecture notes, 2007.

[90] A. Gupte, S. Ahmed, M. S. Cheon, and S. Dey, "Solving mixed integer bilinear problems using MILP formulations," *SIAM Journal on Optimization*, vol. 23, no. 2, pp. 721–744, 2013.

[91] J. Bezanson, A. Edelman, S. Karpinski, and V. B. Shah, "Julia: A fresh approach to numerical computing," *SIAM review*, vol. 59, no. 1, pp. 65–98, 2017.

[92] I. Dunning, J. Huchette, and M. Lubin, "JuMP: A modeling language for mathematical optimization," *SIAM Review*, vol. 59, no. 2, pp. 295–320, 2017.

[93] S. Córdova, C. Cañizares, A. Lorca, and D. E. Olivares, "An energy management system with short-term fluctuation reserves and battery degradation for isolated microgrids," *IEEE Transactions on Smart Grid*, vol. 12, no. 6, pp. 4668–4680, 2021.

[94] J.-F. Toubeau, J. Bottieau, Z. De Greve, F. Vallee, and K. Bruninx, "Data-driven scheduling of energy storage in day-ahead energy and reserve markets with probabilistic guarantees on real-time delivery," *IEEE Transactions on Power Systems*, pp. 1–1, 2020.

[95] L. M. Korunovic, J. V. Milanovic, S. Z. Djokic, K. Yamashita, S. M. Villanueva, and S. Sterpu, "Recommended parameter values and ranges of most frequently used static load models," *IEEE Transactions on Power Systems*, vol. 33, no. 6, pp. 5923–5934, 2018.

[96] A. J. Praktiknjo, A. Hähnel, and G. Erdmann, "Assessing energy supply security: Outage costs in private households," *Energy Policy*, vol. 39, no. 12, pp. 7825 – 7833, 2011.

[97] "Renewable power generation costs in 2019," International Renewable Energy Agency, Tech. Rep., 2019.

[98] S. Córdova, C. A. Cañizares, A. Lorca, and D. E. Olivares, "Frequency-constrained energy management system for isolated microgrids," *IEEE Transactions on Smart Grid*, pp. 1–1, 2022.

[99] V. Lakshmanan, M. Marinelli, J. Hu, and H. W. Bindner, "Provision of secondary frequency control via demand response activation on thermostatically controlled loads: Solutions and experiences from Denmark," *Applied Energy*, vol. 173, pp. 470–480, 2016.

[100] C. Rackauckas and Q. Nie, "Differentialequations.jl–a performant and feature-rich ecosystem for solving differential equations in julia," *Journal of Open Research Software*, vol. 5, no. 1, 2017.

[101] C. Ahumada, R. Cárdenas, D. Sáez, and J. M. Guerrero, "Secondary control strategies for frequency restoration in islanded microgrids with consideration of communication delays," *IEEE Transactions on Smart Grid*, vol. 7, no. 3, pp. 1430–1441, 2016.

[102] J. Hou, H. Li, N. Nord, and G. Huang, "Model predictive control under weather forecast uncertainty for hvac systems in university buildings," *Energy and Buildings*, vol. 257, p. 111793, 2022.

[103] S. Córdova, C. A. Cañizares, A. Lorca, and D. E. Olivares, "Aggregate modeling of thermostatically controlled loads for microgrid energy management systems," *IEEE Transactions on Smart Grid*, submitted for publication.

APPENDICES

Appendix A

Test System Parameters

Additional test system parameters for the computational experiments discussed in Section 3.4 are presented here. For both the KLFN and CIGRE test systems, Li(NiMnCo)O_2-based batteries are considered, which have the following cycle depth stress function:

$$\Gamma^{\lambda}(\lambda) = \left(5.23 \times 10^{-3}\right) \lambda^{2.03}$$

with battery replacement cost of $C^{BR} = 300$ USD/kWh [42]. Furthermore, the considered batteries have an initial SoC of 50%, and corresponding limits of 10% and 90%. For the KLFN test system, a charging and discharging efficiency of $\eta^{B,C} = \eta^{B,D} = 95\%$ is used [42]; on the other hand, for the CIGRE test system, an efficiency of $\eta^{B,C} = \eta^{B,D} = 86\%$ is used [27].

Generator parameters for the KLFN and CIGRE test systems are presented in Tables A.1 and A.2, respectively. These parameters are based on [27], with the only difference that the fuel costs have been linearized to speed-up simulations; note that this linearized version is highly accurate, having a coefficient of determination greater than 95%. A load shedding cost of $C^{LS} = 12$ USD/kWh, as per [96], and droop $\kappa = 3\%$ for all units, as per [86], are used in all simulations.

Table A.1: Generator parameters for KLFN test system

Unit	$\overline{P}_g^G$ [kW]	$\underline{P}_g^G$ [kW]	C_g^G [USD/ kW-min]	C_g^{NL} [USD/ min]	C_g^{SU} [USD]	C_g^{SD} [USD]	RP_g^G [kW/ min]	MN_g^{UP} [min]	MN_g^{DN} [min]
1	1500	600	0.021017	-0.3184	83.60	13.464	150	30	30
2	1000	400	0.008333	1.4678	36.90	7.304	100	30	30
3	600	180	0.003088	0.5891	13.20	4.664	60	30	30

Table A.2: Generator parameters for CIGRE benchmark test system

Unit	$\overline{P}_g^G$ [kW]	$\underline{P}_g^G$ [kW]	C_g^G [USD/ kW-min]	C_g^{NL} [USD/ min]	C_g^{SU} [USD]	C_g^{SD} [USD]	RP_g^G [kW/ min]	MN_g^{UP} [min]	MN_g^{DN} [min]
1	2500	1000	0.003797	0.2493	83.60	13.464	250	60	60
2	1400	600	0.003767	0.3740	39.60	7.304	140	60	60
3	800	350	0.004217	0.1100	13.20	4.664	100	30	30
4	310	60	0.004217	0.0000	6.47	1.267	60	30	30
5	500	100	0.001067	-0.1076	0.83	0.000	100	30	30

Appendix B

Virtual Battery Capacity Limits

The steps used to determine the energy and power capacity limits of the virtual battery model are presented here, which are based on the derivation originally made in [6] for simple first-order household thermal models. For the derivation, (5.7) and (5.8a) are mapped to the Laplace domain, as follows:

$$s\,\Theta_n(s) = -\gamma_n^{TCL}\Theta_n(s) + \Delta p_n^{TCL}(s) \tag{B.1a}$$

$$s\,e^V(s) = -\gamma^V e^V(s) - d^V(s) \tag{B.1b}$$

where $\Theta_n(0) = e^V(0) = 0$ assuming $\theta^I(0) = \theta^{I,SP}$

B.1 Upper Bounds

Define the virtual battery power discharge as the sum of the TCLs baseline deviation, as follows:

$$d^V = -\sum_{n\in\mathcal{N}} \Delta p_n^{TCL} \tag{B.2}$$

Combining (B.2) and (B.1), the following expression for the virtual battery's stored energy can be obtained:

$$e^V(s) = \sum_{n\in\mathcal{N}} \left(1 + \frac{\gamma_n^{TCL} - \gamma^V}{s + \gamma^V}\right) \Theta_n(s) \tag{B.3}$$

for which the property $\Pi(s) = X(s)\,Y(s) \Rightarrow \|\pi(t)\|_\infty \leq \|x(t)\|_1 \,\|y(t)\|_\infty$ can be exploited, where $\pi(t)$, $x(t)$, and $y(t)$ are the inverse Laplace transforms of $\Pi(s)$, $X(s)$ and $Y(s)$, respectively. Consequently, the following inequality for the virtual battery's energy capacity

limit can be obtained:

$$\|e^V(t)\|_\infty \leq \sum_{n\in\mathcal{N}} \left(1 + \frac{|\gamma_n^{TCL} - \gamma^V|}{\gamma^V}\right) \frac{C^I \Delta\theta_n^{TCL}}{\eta_n^{TCL}} \tag{B.4}$$

since $\|\Theta_n(t)\|_\infty = C^I \Delta\theta_n^{TCL}/\eta_n^{TCL}$, as residential TCLs typically have a deadband control with a maximum temperature range of $\Delta\theta_n^{TCL}$.

The virtual battery's power capacity limits can then be obtained from combining (5.5) and (B.2), resulting in:

$$\sum_{n\in\mathcal{N}} \left(p_n^{TCL,SS} - \overline{P}_n^{TCL}\right) \leq d^V \leq \sum_{n\in\mathcal{N}} p_n^{TCL,SS} \tag{B.5}$$

B.2 Lower Bounds

The baseline deviation for each TCL can be defined as a share of the total virtual battery discharge as follows:

$$\Delta p_n^{TCL} = -\beta_n \, d^V \tag{B.6}$$

where $\beta_n \geq 0$ and $\sum_{n\in\mathcal{N}} \beta_n = 1$. Combining (B.1) and (B.6) yields:

$$\Theta_n(s) = \sum_{n\in\mathcal{N}} \beta_n \left(1 + \frac{\gamma^V - \gamma_n^{TCL}}{s + \gamma_n^{TCL}}\right) e^V(s) \tag{B.7}$$

for which the property $\Pi(s) = X(s)\,Y(s) \Rightarrow \|\pi(t)\|_\infty \leq \|x(t)\|_1 \, \|y(t)\|_\infty$ can again be exploited, resulting in:

$$\|\Theta_n(t)\|_\infty \leq \beta_n \left(1 + \frac{|\gamma^V - \gamma_n^{TCL}|}{\gamma_n^{TCL}}\right) E^V \tag{B.8}$$

where the virtual battery's energy capacity limit $E^V = \|e^V(t)\|_\infty$ can be chosen such that:

$$\beta_n \, E^V \leq \frac{C^I \Delta\theta_n^{TCL}}{\eta_n^{TCL}} \left(1 + \frac{|\gamma^V - \gamma_n^{TCL}|}{\gamma_n^{TCL}}\right)^{-1} \tag{B.9}$$

in order to guarantee that that TCLs remain within their temperature deadband, i.e., $\|\Theta_n(t)\|_\infty \leq C^I \Delta\theta_n^{TCL}/\eta_n^{TCL}$.

The virtual battery's power capacity limits can then be obtained by combining (5.5) and (B.6), resulting in:

$$\beta_n \, P^{V,C} \leq \overline{P}_n^{TCL} - p_n^{TCL,SS} \tag{B.10a}$$

$$\beta_n \, P^{V,D} \leq p_n^{TCL,SS} \tag{B.10b}$$

which ensures electric power consumption of each TCL will remain within its limits, i.e., $0 \leq p_n^{TCL} \leq \overline{P}_n^{TCL}$.